Stony Brook University

Development of a Green Cost-Efficient Technology for Biogas Purification to Pipeline Quality Natural Gas

A Dissertation Presented

By

Saurabh Umesh Patel

To

The Graduate School

in partial fulfillment of the

requirements

for the Degree of

Doctor of Philosophy

in

Materials Science and Engineering

Stony Brook University

December 2013

State University of New York at Stony Brook

The Graduate School

Saurabh Umesh Patel

We, the dissertation committee for the above candidate for Doctor of Philosophy degree, hereby recommend acceptance of this dissertation.

_____

Dr. Devinder Mahajan
Department of Material Science and Engineering

_____

Dr. Dilip Gersappe
Department of Material Science and Engineering

_____

Dr. David Tonjes
Department of Technology and Society

_____

Dr. Kyoung Ro
U.S. Department of Agriculture – ARS

This dissertation is accepted by the graduate school

_____

Dr. Charles Taber
Dean of the Graduate School

Abstract of the Dissertation

Development of a Green Cost-Efficient Technology for Biogas Purification to Pipeline Quality Natural Gas

By

Saurabh Umesh Patel

Doctor of Philosophy

In

Materials Science and Engineering

Stony Brook University

2013

Biogas is a clean renewable energy source which can be directly substituted in place for conventional fossil fuel. Regrettably, biogas often contains a large amount of H_2S which must be removed for its effective usage. The focus of this study was to assess potential of local biogas production on Long Island, NY and develop a cost-effective and environmentally friendly technology for removal of H_2S in a biogas stream. An assessment of the biogas potential found that 234 x 10^6 m^3 of CH_4 can be locally produced, which is equivalent to 2.54 TW-h of electricity, approximately 12% of fossil fuel power generation of Long Island. Biochar produced from hardwood, switchgrass, rye, and animal waste was evaluated as a potential adsorbent of H_2S. Samples were characterized and activated under CO_2 and O_2. Prior to activation biochar samples exhibited limited H_2S adsorption capacity, but this improved by over 88% after activation. The

maximum surface area (1103 m^2g^{-1}) was attained at 850°C under CO_2 oxidation in the hardwood based biochar. The highest H_2S adsorption capacity was found to be 100 mg of H_2S/g of sample at STP. H_2S adsorption studies on metal oxides were carried out using CuO, NiO, and Fe_2O_3 catalysts. The results showed the decomposition of H_2S on $Fe_2O_3 \rightarrow H_2 + S^0$ at 210°C with adsorption capacity of 3.38 g H_2S/g sample.

Dedication

To my parents who always told me to pursue my dreams.

To my wife who has become the foundation of my life.

Contents

List of Figures

List of Tables

List of Abbreviation

AD – Anaerobic Digester

BET – Brunauer-Emmett-Teller

BTU – British Thermal Units

C&D – Construction and Demolition

COD – Chemical Oxygen Demand

EIA – Energy Information Administration

EPA – Environmental Protection Agency

FPD – Flame Photometric Detector

FID – Flame Ionizing Detector

gHgS – gram of H_2S per gram of Sample

GHG – Greenhouse Gas

HTT – Highest Treatment Temperature

LI – Long Island

LGRF – Landfill Gas Recovery Facility

mHgS – milligram of H_2S per gram of Sample

MLD – Million Liter Per Day

MSW – Municipal Solid Waste

MW – MegaWatt

PPB – Parts Per Billion

PPM – Parts Per Million

TCD – Thermal Conductivity Detector

TW – TeraWatt

VOC – Volatile Organic Compound

VS – Volatile Solids

WWTP – Wastewater Treatment Plant

Acknowledgment

I would like to highly acknowledge my academic advisor Dr. Devinder Mahajan for the opportunity to work under his guidance. I am grateful to Dr. David Tonjes for the numerous discussions and advice he has provided me with over the years. My sincere thanks to Dr. Dilip Gersappe for introducing me to LBM and guiding me throughout my PhD. My special thanks to Dr. Kyoung Ro for providing the biochar samples, the bases of all my experiments.

Thank you to all my lab mates and friends, Wei Nan, Kristine Horvat, Mason Yeh, Julie Hasty, and Prasad Kerkar for all the support they have provided me with in the past five years.

To all my friends who have been by myself in the good times and the bad times: Shayan Byrappa, Ravi Dey, Gagan Jodhani, Mani Sen, Sumantu Iyer, Srivatsa Bhat, Shishir Das, and Saurabh Shervat. I am also thankful to all the staff members in Materials Science department for all they have done for me over the years.

Chapter 1: Introduction

In 2013, global natural gas consumption was 117 trillion ft^3 while the United States consumed 25.3 trillion ft^3. Natural gas is heavily used by power, industrial, and residential sectors. It is a relatively inexpensive and cleaner fuel source as compared to other fossil fuels. Natural gas consists primarily of methane (CH_4) with trace amounts of carbon dioxide (CO_2) and nitrogen (N_2) after being purified. With renewed interest in local energy production in recent times, a new technological advancement known as hydraulic fracking has led to increased production of natural gas. The US-EIA projects natural gas production growth to 41.5 trillion ft^3 by 2040 – an increase in 39% from 2013 – led by stronger demand in power and industrial sectors. Despite the recent increase in natural gas production due to fracking, the cost of natural gas has been steadily increasing and the price of natural gas is projected to reach about $11 per million BTU by 2040, compared to about $6 per million BTU in 2013[1]. The projected rate of price increase of 1.7% per year is the highest among all energy sources. Hydraulic fracking involves injection of numerous chemicals into the ground to extract shale gas, which can potential cause environmental hazards. Critics of fracking have pointed to large amount of the chemicals ending up in deep underground aquifers as well as released of fugitive gases into the atmosphere[2-4]. An attractive alternative to overcome such environmental hazards while still fulfilling demand is to utilize renewable biogas. Local production of biogas can provide a safe and sustainable alternative to natural gas obtained via hydraulic fracking.

The production of bioenergy from biomass is becoming an important source of energy. Traditional use of biomass is simply burning the biomass for heating and cooking purposes. This is also a means of dealing with unwanted waste in many parts of the world. Rather than using

biomass is such manner it can be better utilized by anaerobically converting biomass into renewable biogas.

Renewable biogas is produced when organic matter decays in the absence of oxygen (anaerobic digestion). The typical composition of biogas is 60% CH_4, 38% CO_2, and 2% other gases including N_2, hydrogen (H_2), hydrogen sulfide (H_2S), and oxygen (O_2) in comparison to natural gas which contains 70-95% CH_4 and 5-30% other gases[5-8]. Biogas can be used as is or can be upgraded to pipeline quality natural gas.

Compound Name	Chemical Formula	Biogas (%)	Natural Gas (%)
Methane	CH_4	50-75	95
Carbon Dioxide	CO_2	25-50	0.7
Nitrogen	N_2	0-10	1.3
Hydrogen	H_2	0-1	Trace
Hydrogen Sulfide	H_2S	0-3	-
Oxygen	O_2	0-2	0.02

Table 1.1: *Composition of biogas from anaerobic digester in comparison to pipeline quality natural gas.*

Naturally occurring anaerobic conditions in places such as landfills and wetlands allow methanogenic bacteria to feed on organic matter and produce biogas. Over 400 million tons of biogas is produced worldwide each year from multiple sources including rice paddies, sewage sludge, livestock manure, and bio-waste[9]. There are many advantages of utilizing biogas as a fuel source:

1. Biogas production from organic waste in an anaerobic digester leads to controlled production of CH_4 without risk of GHGs being released into the atmosphere, unlike hydraulic fracking[4, 10].
2. Biogas production from anaerobic digesters presents the advantage of treating organic waste that might otherwise be landfilled and negatively impact the environment[10]. This also means lower cost for waste disposal for local communities.
3. Capturing fugitive biogas from landfills prevents highly damaging GHGs from entering the atmosphere. It is well known that CH_4 is 20x more potent in the atmosphere compared to carbon dioxide thus uncontrolled release of it is damaging to the environment and human health[11].
4. The use of biogas as biomethane does not require supplementary infrastructure, since it can be directly introduced into the existing natural gas network after purification.

To increase the use of biogas in the most effective way, contaminates in the gas stream must be removed. There are number of different industrial processes that can be utilized to upgrade biogas including water scrubbing, membrane separation, and pressure-swing adsorption to name a few. Unfortunately, many of these processes consume large amount of energy, create additional chemical waste, or are very expensive. In this study, we focused on developing a cost-effective and environmentally-benign biogas purification technology using biochar.

Biochar is a carbon-rich product obtained when biomass is heated in a closed container with limited oxygen (pyrolysis). Usually biochar is considered a waste by-product of pyrolysis since bio-oil and syngas are the targeted products. Biochar has the right physical and chemical

properties to remove contaminants in biogas. A focus on producing bio-oil and syngas from biomass has led to neglect of biochar utility for many years. Nonetheless, a number of studies have been conducted to characterizing and applying biochar[12-15]. Currently, the biggest use of biochar is its application to soil as a means of improving soil productivity. Its use for carbon storage has also been widely studied[16-18].

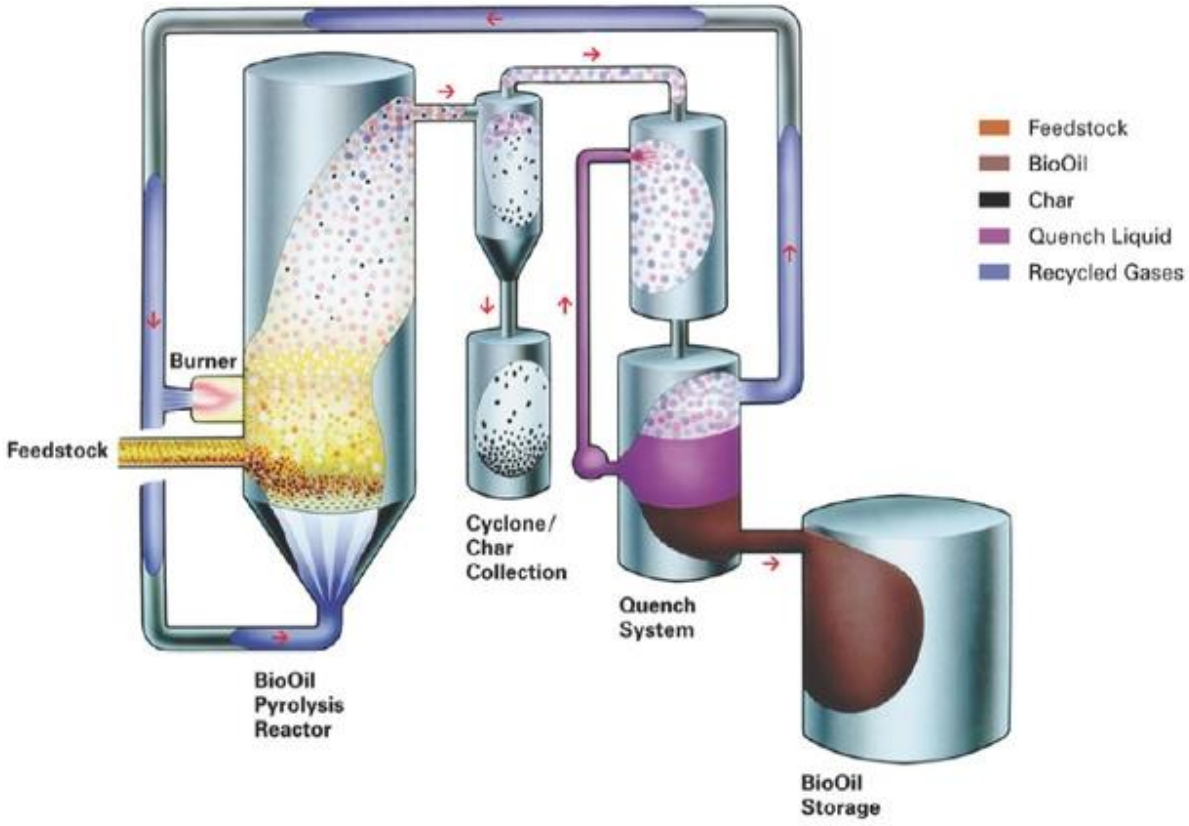

Figure 1.1: *Illustration of a typical pyrolysis unit where different biomasses are used as feedstock. Main purpose of this process is converting biomass into more useful bio-oil and syngas with a by-product of biochar[19].*

The knowledge that biogas can be extracted from decaying plants and vegetables has been known for centuries, but it was not until 1895 in the United Kingdom that it was utilized as a fuel source[20]. Since then, biogas manufacturing technology has come a long way. The production of biogas can come from multiple sources including biomass, manure, sewage, landfills, and

wetlands, making it a "green" renewable fuel. With the help of technology biogas can be produced in a controlled manner.

1.1 Biogas

Anaerobic digestion involves a large number of microorganisms working in synergy, which are often classified into two groups, acetogens and methanogens. The acid formers produce acetic and propionic acids based on a COD mass balance, while the CH_4 formers convert the acids and by-products into CH_4 [20, 21].

The process of anaerobic digestion occurs in four stages: hydrolysis, acidogenesis, acetogenesis, and methanogenesis. In the initial stage, large proteins, fats, and carbohydrate polymers are broken down through hydrolysis into amino acids, long-chain fatty acids, and sugars. Most of the microorganisms which take part in hydrolysis are strict anaerobes such as bacteriocides, colstridia, and bifidobacteria. The initial products are fermented during acidogenesis to form three, four, and five-carbon volatile fatty acids, such as lactic, butyric, propionic, and valeric acids. The H_2 producing acetogenic bacteria consume these fatty acids and form acetic acid, CO_2, and H_2. Typical homoacetogenic bacteria are *Acetobacterium woodii* and *Clostridium aceticum*[20, 21]. Finally, methanogenic bacteria consume the acetate, H_2, and some of the CO_2 to produce CH_4. The chemical reactions which take place in the final methanogenic stage to produce CH_4 are:

Acetotrophic methanogenesis: $CH_3COOH \rightarrow CO_2 + CH_4$ (1)

Hydrogenotrophic methanogenesis: $CO_2 + 4H_2 \rightarrow CH_4 + 2H_2O$ (2)

Methylotrophic methanogenesis: $CH_3OH + H_2 \rightarrow CH_4 + H_2O$ (3)

Acetotrophic methanogenesis is the primary pathway to produce CH_4. Based on Eq. (1), theoretical biogas yield is 50% CH_4 and 50% CO_2, but this is not always the case. For instance, during the acetogenic stage a small amount of H_2 is produced, and for every four mole of H_2 consumed by hydrogenotrophic methanogens, a mole of CO_2 is converted into CH_4. Additionally, fats and proteins can yield large amounts of H_2 for hydrogenotrophic methanogens to consume[22].

Anaerobic digestion is sensitive to temperature conditions, pH, anaerobiosis, and toxic compounds[23]. For instance, in a two stage AD, in which two digesters operate in series, the rate of degradation in both stages must be equal in size. If the first degradation stage runs too fast, the acid concentration rises and the pH drops below 7.0 which inhibits the methanogenic bacteria. If the second phase runs too fast, methane production is limited by the first stage. Thus, the rate-limiting step depends on the feedstock which is being digested[21]. Therefore, the process design must be well suited to the feedstock properties to insure optimum biogas production.

1.1.1 Landfills

The natural decomposition of biomass in landfills leads to production of gas commonly known as landfill gas. When burned, a cubic foot of the gas can yield as much as 10 Btu of heat energy per percentage of CH_4 composition[24]:

$$\frac{Energy\ (Btu)}{Cubic\ feet} = 10(Btu) * \ Percent\ of\ CH_4\ Composition \tag{4}$$

Production of landfill gas largely depends on the type of waste, age of the waste, the quantity, and weather conditions. For instance, landfills in hot dry, climates produce less CH_4, but wet places produce more CH_4. If not captured, CH_4 from landfills becomes a greenhouse gas that is at least 20 times more potent than CO_2 [11].

In 2011 the U.S. EPA estimated about 250 billion kgs of MSW was generated in the U.S., equal to two kgs per person per day. Of the 250 billion kgs of waste generation, 54% was discarded in landfills while the 46% was either recycled, composted or combusted with energy recovery[25]. According to the EPA, nearly 25% of CH_4 released into the atmosphere comes from landfills. Therefore, capturing this naturally escaping gas will address environmental concerns, as well as increasing energy demands. While many of the large landfills around the US have a LGRF, they lack the proper means to fully utilize the gas, resulting in simply flaring of the gas[26, 27]. With help of upgrading technology the gas can be burned in generators to produce electricity.

1.1.2 Waste Disposal Technologies

The production of biogas from MSW can be done in a controlled manner instead of simply being landfilled. Technologies such as anaerobic digestion, thermal processing, and hydrolysis can be used produce biogas and reduce waste volume. Waste can be brought to a processing center which utilizes such technologies to produce biogas.

1.1.2.1 Anaerobic Digester

Organic components in MSW – such as food waste, yard waste, cardboard, and paper – are consumed by bacteria in absence of oxygen in an AD resulting in biogas, solid byproducts, and reclaimed water. AD can be broken into three parts: pre-treatment, digestion of the feedstock, and post-treatment. The need for pre-treatment and post-treatment is strongly correlated to the particular digestion technology being used and the overall objective of the user. Pre-treatment requires the separation of organics from other waste and the size reduction of the feedstock, while post-treatment requires the disposal of residuals after digestion. The purpose of MSW digestion is to produce stable digestate (immature compost) from organic feedstock and large amounts of

biogas. ADs produce biogas which is richer in CH_4 as compared to landfill gas. Depending on the type of digester used the concentration of CH_4 varies from 55-80%[28].

1.1.2.2 Thermal Technology

Thermal processing technologies use heat under controlled conditions to convert MSW to usable products. It has the potential to convert all organic parts of MSW into energy. Thermal processing technologies include gasification, plasma gasification, pyrolysis, cracking and depolymerization. All of the above technologies have advantages and disadvantages. Thermal processing occurs in high-temperature reaction vessels. For instance, reactor temperatures range from 426 °C for cracking technology to 4426 °C for plasma gasification. Thermal processing produces a gas known as "syngas," which is different than biogas[28]. Unlike biogas, syngas is predominantly a mixture of carbon monoxide (CO) and H_2. The gas can be used in boilers, reciprocation engines and combustion turbines. While a large amount of electricity can be generated from these processes, a large amount of electricity is needed to power the processes.

1.1.2.3 Hydrolysis

Hydrolysis is a developing technology being utilized to break down MSW into useful byproducts. It is a process in which water reacts with another substance to form two or more new substances. Chemical reactions between water, acids, and organic matter in MSW produce sugars in hydrolysis. The sugar is then fermented to produce alcohol, followed by distillation to separate the water from alcohol, and recovery of fuel-grade ethanol. During the process hydrolysis produces byproducts: usually gypsum and lignin which can be later used in the hydrolysis process[28, 29]. Hydrolysis waste technology is in the development stage, and is expensive and unreliable.

With the aid of current and projected future technologies, MSW can be transformed into reusable fuel sources. The economic feasibility of such transformations needs to be studied further. Meanwhile, existing landfills can be utilized to capture biogas and transform it into a renewable fuel source.

1.2 Biogas to Bio-methane

Biogas treatment is generally required for it to be used in a conventional manner, for example, as a vehicle fuel or for injection into the natural gas grid. This treatment removes trace compounds which are harmful to the natural gas grid or end-user appliances. Removal of CO_2 is also important in terms of increasing the calorific value of the gas. This study is focused on removal of H_2S and CO_2 from the gas stream. An overview of such processes is presented below. Removal of H_2S can be done at two different stages during biogas production: (1) removal of H_2S during digestion[30-34] and (2) removal of H_2S after digestion[5, 35-38].

1.2.1 Chemical Scrubbing

Direct injection of pure oxygen into the anaerobic digester has been studied by[32, 33]. Small amount of O_2 (2-6 vol%) can be introduced into the digester for removal of H_2S with an efficiency of 80-99%. Use of air instead of pure O_2 has also shown an efficiency of 99% without affecting COD removal, VS reduction and CH_4 production. Introduction of nitrate into the digester has also been studied but without any success in removing H_2S[32]. Safety measures must be taken when using this method to avoid overdosing which can create an explosive mixture with the biogas. It may also stop the anaerobic process if overdosed. Addition of iron chloride ($FeCl_{2-3}$) to the digester leads to precipitation of iron sulfide (FeS) instead of producing H_2S. This method is very effective in reducing high concentration of H_2S, but not at eliminating low levels of H_2S. H_2S reductions by this method are limited to minimum of 100 ppm[33, 34].

Adsorption of H_2S using iron oxide (Fe_2O_3) and iron hydroxide ($Fe(OH)_3$) has long been used in industry[5, 33, 34]. This process is often referred to as "iron sponge" because iron wool is used to form the reaction bed. The reaction takes place as following:

$$Fe_2O_3 + 3H_2S \rightarrow Fe_2S_3 + 3H_2O \quad (5)$$

Decomposition of H_2S by Fe_2O_3 is an endothermic reaction; therefore, a minimum temperature of 12°C is required for the reaction to take place. Optimal temperature for the reaction is between 25-50°C. One of the major advantages of using iron as an adsorbent is that it can be regenerated with oxygen according to the following reaction:

$$2Fe_2S_3 + 3O_2 \rightarrow 2Fe_2O_3 + 6S \quad (6)$$

This reaction is exothermic in nature therefore caution must be taken otherwise the reaction can lead to self-ignition.

A number of different other approaches have been studied and commercialized for removal of H_2S and other impurities in biogas. Use of aqueous solutions for chemical absorption of H_2S is one such method. These processes can be divided into two different methods: (1) oxidation of S^{2-} to S^0 and then capture of S^{2-} through precipitation of its metallic salts owing to their very low K_{sp} (water solubility product); (2) decomposition of H_2S by aqueous alkaline solution. The biggest disadvantage of this latter method is the high reactivity of CO_2 with alkaline solutions making H_2S removal highly inefficient.

The use of iron-chelated solutions for oxidization of H_2S has been commercialized since 1991. The first published study on this method was by Neumann and Lynn[39]. They found that that Fe-chelated solution involved the following redox reactions:

$$2Fe^{3+} + H_2S \rightarrow 2Fe^{2+} + S + 2H^+ \quad (7)$$

$$2Fe^{2+} + (1/2)\, O_2 + H_2O \rightarrow 2Fe^{3+} + 2OH^- \quad (8)$$

The advantage of this process is the conversion of H_2S into S^0 particles that can be disposed of easily and safely with high efficiency. In addition, regeneration of the aqueous solution can be carried out easily as seen from Eq. 8. Fe-EDTA (ethylendiaminetetraacetic acid) and Fe-HEDTA (hydroxyl-ethyletheylenediaminetriacetic acid) are the most commonly used chelating agents for H_2S conversion. Horikawa et al.[40] reported that use of Fe-EDTA chelate resulted in higher percentage of H_2S removal compared to H_2O. In a continuous counter current solution flow-rate of 68-84 ml min^{-1} with gas flow-rate of 1000 ml min^{-1} at room temperature and low pressure (1.2 - 2.2 bar), it was possible to completely remove H_2S from the gas stream, at concentrations of 2.2 - 2.36%. Unfortunately, this process is fairly complex, and industrial applications are possible only at high-capacity units.

Use of metal sulfate solutions to remove H_2S has also been studied. This process deploys a scrubber as a gas-liquid contractor-reactor. The H_2S gas diffuses in sulfates containing aqueous solutions and reacts with metallic cations to form an insoluble solid metal sulfate. This metal sulfate is oxidized with ferric ions, forming S^0 and regenerating the metal sulfate solution. The ferrous ions are reoxidized with air in a separate counter current bubble column. Broekhuis et al.[41] studied the absorption of H_2S on Cu and Zn sulfates solutions. Performance of Zn sulfate was linked to the pH of the solution, and was unsatisfactory for the pH range studied, while Cu sulfate

performed well under wide range of pH values. Copper solution allowed for rapid absorption rates and was limited by the diffusion rate of the gas. It was shown that 99% removal rate of H_2S can be achieved using this process. The biggest drawbacks for this process are that at small scale it is not economically feasible, it is more energy intensive, and the severity of the reaction is higher[5].

1.2.2 Water Scrubbing

The process of water scrubbing is used to remove CO_2 and H_2S from biogas since they are more soluble in H_2O than CH_4. In this process, biogas is pressurized to 150 to 300 psi, and introduced into the bottom of a tall vertical column, while H_2O is introduced from the top flowing downward over a packed bed. The packed bed is typically composed of high surface area plastic media that allow for efficient contact between water and gas phases in a countercurrent absorption regime. The CO_2 and H_2S saturated H_2O exits the column from the bottom. The H_2O in some cases can be regenerated and recirculated back to the column. This is done so by depressurizing or by stripping with air in a similar column[34, 35, 37]. Regeneration and recirculation is not recommended when high levels of H_2S are present in the gas because the contaminated H_2O can damage metal parts. Thus, in many instances a single-pass process with no H_2O regeneration stage is used.

The biggest advantages of H_2O scrubbing are the relative simplicity and low cost of the operation. Ninety-five percent CH_4 purity and relatively low CH_4 loss (2%) can be achieved in a single stage process. This type of system is suited for wastewater facilities which have large amount of free flowing H_2O. The use of this technology has declined since its introduction in 1970s.

1.2.3 Polyethylene Glycol Scrubbing

Polyethylene glycol scrubbing is a physical absorption process like H_2O scrubbing. Selexol is the trade name solvent used to drive this process. Just as in H_2O, CO_2 and H_2S are more soluble in Selexol than CH_4 but their solubility in Selexol is greater than in water resulting in lower solvent demand and reduced pumping. This is a proven process which is extensively used in the natural gas industry as well as other applications. The solvent is typically kept under pressure, which improves its capability to absorb the contaminants. These types of systems are designed with recirculation. Removal of contaminates from the solvent is done so by steam or inert gas. Stripping the Selexol solvent with air is not recommended due to presences of elemental sulfur, therefore prior H_2S removal is preferred[5, 35, 42]. The major issue with this process is that it is more expensive than water scrubbing or pressure swing adsorption.

1.2.4 Pressure Swing Adsorption

This technology uses columns filled with molecular sieves that can separate CO_2 and H_2O easily from the biogas while letting the CH_4 pass through. It usually employs four connected columns that work on the principle of pressure differential, which reduces the energy consumption for gas compression. The pressure released from one column is used by the others. The first column cleans the raw gas at 90 psi to an upgraded biogas with vapor pressure of less than 10 ppm H_2O and a CH_4 content of 96% or more. In the second column the pressure is released to 45 psi by pressure communication with the fourth column, which was previously degassed by a slight vacuum. The release gas flows back to the digester in order to recover the CH_4. The third column is depressurized from 15 to 1 psi. The desorbed gas, consisting of CO_2, is released into the environment[5, 33]. This process produces a water-free gas that is cleaner than other techniques such

as water scrubbing but requires more sophisticated process controls. Small-scale installations have shown excellent results in cleaning the gas, energy efficiency, and cost.

1.2.5 Membrane Separation

There are two basic systems of membrane separation: a high pressure gas separation with gas phases on both sides of the membrane, and a low-pressure gas-liquid absorption separation with liquid absorption occurring as gas molecules diffusion through the membrane to the opposite side. High pressure gas separation is the most common membrane separation technology used. Pressurized gas is first cleaned for hydrocarbons and H_2S. The raw gas is upgraded in three stages, where the pressure is increased from 41 to 150 to 525 psi, to a clean gas with 96% CH_4 or more. The waste gas in stage one and two can be recycled, while in stage three the waste gas is flared or used in a steam boiler. The clean gas is normally compressed and stored at 3,600 psi in large tanks. The tanks are kept at low, medium, and high pressures, allowing for sequential fast filling by fuel dispenser. Some of the major drawbacks are the short lifetime of the membranes, when compared to other methods, as they decrease in permeability by 30% after 18 months[35].

Gas-liquid absorption membranes separation is a recently developed technology that upgrades biogas to more than 96% CH_4. The technology is based on microporous hydrophobic membrane separation the gaseous from the liquid phase. The gas flows in one direction, and this allows H_2S and CO_2 to diffuse through the membrane to the other side where the liquid (NaOH), flowing in the opposite direction, captures the contaminate. This method is highly efficient and operates at 25 °C to 30 °C[35]. Contaminates in the absorbent can be recovered and sold for profit.

1.2.6 Amine Scrubbing

Amine scrubbing is a process that is widely used in food-grade CO_2 production and has become the preferred technology for large-scale systems that recover CO_2 from natural gas wells. The principle of amine scrubbing is given by the following reactions[43, 44]:

CO_2 sorption: $$RNH_2 + H_2O + CO_2 \rightarrow RNH_3^+ + HCO_3^- \ (under\ pressure) \quad (9)$$

CO_2 desorption: $$RNH_3 + HCO_3^- \rightarrow RNH_2 + H_2O + CO_2 \ (low\ pressure, heat) \quad (10)$$

where R represents the remaining organic component of the molecule that is not relevant to this reaction.

The biggest advantage of amine scrubbing is the high selectivity for CO_2. One to two orders of magnitude more CO_2 can be dissolved per unit volume than with H_2O scrubbing. Also, regeneration with waste heat lowers overall energy use, making it energetically more efficient than polyethylene glycol or H_2O scrubbing. These systems have issues regarding corrosion, amine breakdown, and contaminant buildup. Scaled-down systems have been developed for landfill and farm applications.

1.2.7 Cryogenic Separation

Cryogenic separation is the newest method under development for biogas upgrading. The idea stems from the fact that CO_2, CH_4, and other contaminate all liquefy in different temperature-pressure domains; it is possible to separate the CH_4 from biogas by cooling and compressing CO_2 out of the gas. This technology has been proposed by Acrion Technologies to purify landfill gas[34, 35]. A full development of the technology followed by an economic assessment is needed.

1.3 Biochar

The first known use of activated carbon dates back to the ancient Egyptians, where it was used for medicinal purposes. It was not until the late 19th century that large-scale use of wood based carbon was utilized for decolorization and purification of cane sugar. By the 1930's industrial scale use of carbon for gaseous and liquid phase applications and new manufacturing processes had been developed. Modern day use of carbon spans over many different industries including, medical, wastewater treatment plants, agricultural, and gas purification.

In most instances materials with high fixed carbon can be developed into solid carbon. The most commonly used raw materials are coal, coconut shells, and wood. Commercial production of carbon is limited, based on the raw material that is available. This is highlighted by the fact that 1000 tons of raw material will only yield approximately 100 tons of activated carbon[45]. During the carbonaceous phase most carbons develop a certain degree of porosity and BET surface area of 10-15 m^2g^{-1}. Additional surface area can be created by further oxidizing the carbon. This can be achieved by two different methods, physical activation (for example, use of steam, CO_2, and air) and chemical activation (for example, $ZnCl_2$, KOH and NaOH). During activation, an oxidation process begins at the edge groups on the external surface of the material, leading to formation of macropores (>50 nm in diameter). Secondary channels are formed within macropores soon after, known as mesopores (2-50 nm in diameters). Finally, the micropores (<2 nm in diameters) are formed by oxidization of the planes deep within the structure of the carbon.

Activated carbon having BET surface area well in excess of 200 m^2g^{-1} can be characterized as porous carbon. These types of carbons can easily be prepared by the carbonization and activation of variety of precursors. One of the biggest advantages of these carbons is its ability to

adsorb molecules. These phenomena are known as physisorption (physical adsorption) and chemisorption (chemical adsorption). These two processes are discussed later in the chapter.

1.3.1 Biochar Production

Slow pyrolysis produces bioenergy products in the form of bio-oil and syngas, which can be used to offset fossil-fuel emissions, while converting up to 50% of the C in the biomass into more stable biochar[15, 46, 47]. Biochar is a product obtained from thermal decomposition of biomass, such as wood, in an enclosed container with limited supply of oxygen. Lower process temperatures and longer residence times ensure higher production of biochar. Meanwhile, moderate temperature and shorter residence time leads to more bio-oil production[48]. Slow pyrolysis ensures that immediate decay of these biomass inputs does not occur. Biochar can be produced at many different scales ranging from large industrial setting to individual farms[17]. It can be produced of different forms of organic matter, such as agricultural plant residues, animal manure, wood and many other biomasses. The production process is typically self-sufficient in energy requirements and can produce surplus energy for use in various applications[48, 49].

A number of studies[12, 13, 15, 50, 51] have looked at biochar as a soil amendment which can improve agricultural productivity, especially in low-fertility and degraded soil. It can reduce losses of nutrients and improve water-holding capacity of the soil. Biochar application to soil has been shown to affect C and N transformation and retention processes in soil. Studies have also shown that incorporating biochar within soil reduces N_2O and CH_4 emissions from soil, which could contribute to mitigating GHG emissions[13, 51]. The potential of biochar as a C sink stems primarily from its refractory nature, which slows the rate at which photosynthetically fixed C is returned to the atmosphere[16]. Biochar is comparable to activated carbon and is extremely porous allowing it to have large surface area for adsorption or chemical reaction.

1.3.2 Physical and Chemical Properties of Biochar

Chemical and physical properties of biochar are difficult to generalize as they depend on the variety of biomass and pyrolysis conditions used. Operating parameters during pyrolysis that influence the physical properties of biochar include: heating rate, HTT, pressure reaction residence time, reaction vessel, pre-treatment, the flow rate of ancillary inputs, and post-treatment. Although all of these parameters contribute to the final biochar structure, HTT is expected to have the most influence. The physical and structural characteristics of biochar are influenced by the original structure of feedstock as well as the process parameters. During pyrolysis, volatile organics in biomass are lost resulting in a disproportionate amount of the volume loss. Consequently, during thermal conversion, the mineral and C skeleton formed retains the rudimentary porosity and structure of the original material. The residual structure accounts for majority of the macroporosity in biochar[12].

Biochar surfaces are heterogeneous with complex defect structures and a significant quantity of organic and metallic compounds. The highly porous surface has been shown to adsorb N_2O, CO_2, and CH_4. Just like activated carbon, pore sizes in biochar can be separated into three categories of micropores, mesopores and macropores. Micropores contribute most to the surface area of biochar and are responsible for the high adsorptive capacities for molecules of small dimensions such as gases[52]. Macropores serve as feeder pores for transport of molecules. All biochars contain a mixture of these three catagories of pore sizes; the distribution is dependent on the material being oxidized. In cases where micropores account for majority of the surface area, that carbon is better suited for adsorption of small molecular weight species and applications involving low contaminate concentrations. When meso and micropores are dominant, adsorption of larger molecular species is more appropriate [53].

Biochar density can be characterized as solid density and bulk density. Solid density is the density on a molecular level, related to the degree of packing of the C structure. Bulk density is that of the material consisting of multiple particles and includes the macroporosity within each particle and the inter-particle voids. The density of the biochar depends upon the nature of the starting material and the pyrolysis process. Solid density typically has values of 1.5 – 1.7 g cm^{-3}, while bulk density ranges from 0.30 – 0.43 g cm^{-3} for biochar made from wood[12].

The molecular structure of biochar determines its BET surface area and porosity. Biochar structure is essentially amorphous in nature, but contains some local crystalline structure[54]. During pyrolysis the crystalline structure in biomass is enlarged and made more ordered. This effect increases with increasing HTT until the temperature at which deformation occurs. High HTT causes orderly spacing between the planes, leading to decreased distance between interplanes and organization of molecules, all of which results to larger surface area per volume until a critical temperature is reached[12]. For example, Lua et al.[55] found that increasing HTT from 200°C to 500°C increases BET surface area in biochar made from pistachio-nut shells due to increasing evolution of volatiles. When the HTT was increased from 500°C to 800°C BET surface area decreased. They concluded that decomposition and softening of some volatile fractions formed an intermediate melt in the biochar structure.

1.3.3 Carbon Surfaces

The carbon surface can be both hydrophilic and hydrophobic based on the elements adsorbed onto the surface. If hydrogen is chemisorbed it becomes hydrophobic, whereas surface with oxygen-containing surface groups are hydrophilic. Hydrophobic surfaces shows type III isotherms on non-porous carbon and type V in the case of porous carbons[56].

1.3.4 Surface Oxides of Carbon

The most important surface complexes of biochar are those with oxygen. The majority of the surface oxides can be produced by treating the surface with O_2, ozone or NO_x[14, 57]. Oxidation of the C surface with O_2 or air is usually done at reaction temperatures of 250-400 °C. During oxidation, mostly acidic surface oxides are produced in a few hours. Carbons with clean surfaces and high surface area can also oxidize at room temperature. This reaction takes place quickly at the beginning but slows down gradually[56].

The addition of O_2 to the C surface can be done more efficiently in a slow reaction with moist air, a process known as aging. The presence of H_2O vapor accelerates the reaction significantly. It was found that surface oxidation occurs faster at low temperature with high humidity than at high temperature with low humidity. Aging is drastically increased in the presences of catalytically active metals. Due to the aging process the surface becomes more and more hydrophilic and the adsorption capacity for noxious gas is greatly reduced. The surface oxidation begins on the surface of the particles and progresses very slowly into their interior due to slow diffusion of O_2 [57]. This results in an activated carbon which has different adsorption properties on exterior and interior surfaces.

Treatment of carbons by aqueous solutions of hydrogen peroxide, ammonium peroxodisulfate, or sodium hypochlorite has been used to oxidize the surface. In addition, nitric acid is often used; it is easy to control the oxidizing effects but the disadvantage of this is that micropores become wider and the micropore volume is reduced. In addition to aqueous solutions, metal ions can also be used for oxidizing agents, including precious metals such as $[PtCl_6]^{4-}$, Ag^+, or Fe^{3+} ions[57].

1.3.5 Functional Groups

O_2 is chemically bound to the carbon surface in the course of oxidation. It is to be expected that most of it is bound by covalent bounds in the form of functional groups. In most instances the following functional groups are present on carbon surface: carboxyl groups, carboxylic anhydrides, lactones, lactols, phenolic hydroxyl groups, carbonyl groups, o-quinone-like structure, and ether-type oxygen atoms. Carboxyl groups are strong acids, while phenols and carbonyls are weak acids groups. Chromenes and pyrones are basic functional groups[14, 58].

It is well understood that there is a large difference in mineral matter content and composition on the surfaces of biochar. In high-mineral ash biochar, it is probable that some of the functional groups will contain metals. The presence of N- and S-based functional groups is more predominant in biochar derived from manures, sewage sludge, and rendering wastes than in lignocellulosic biochar. N-based functional groups are known areas of high basicity. Koutcheiko et al.[22] detected a range of different N- and S-based functional groups when preparing chicken manure biochar at 360 °C. The biochar was then heated to 800 °C and activated with CO_2. The main N-based functional groups present for the low temperature biochar were pyrrolic or pyridinic amines. Biochar treated at high temperature had nearly equal amounts of pyridinic and quaternary groups. In terms of S-based functional groups sulfonates and sulfates were seen on low-temperature biochar and thiophene and sulfide groups on high-temperature biochar. Bagreev et al.[59] observed similar results when sewage sludge was charred from 450-900 °C. At low temperature, amine functional groups were detected, while at high temperatures the same analysis suggested that the organic N was incorporated within the biochar as pyridine-like compounds.

A number of different studies has shown that the relative concentration of functional groups depends upon initial composition of the feedstock, reaction temperature, composition of the gas

surrounding the charring particle, the rate of heating, and any post-treatment[14]. Identifying such groups is normally done with infrared spectroscopy, TPD, and XPS. TPD normally observes H_2S, CO_2 and CO peaks from carbons. It is usually assumed that CO_2 comes from carboxyl groups, and CO from carbonyl and ether oxygen. However, the results can be misleading since carboxylic anhydrides or lactones will thermally decompose to CO_2 plus CO.

1.4 Adsorption Mechanism

Adsorption is a process in which a gas or liquid (adsorbate) attaches itself to the surface of an adsorbent. This is not to be confused with absorption in which gas or liquid is taken up within the volume of the adsorbent. Thus, adsorption is a surface based process and absorption is a volume based process. Adsorption is an exothermic process (i.e. $\Delta H<0$), however, entropy of the system is also decreased due to the decrease in number of microstates and degree of freedom of the molecules. Therefore, adsorption is thermodynamically favorable at low temperatures (Figure 1.2)[60]. As stated above, adsorption proceeds on two different paths: physisorption and chemisorption. Distinguishing between physisorption and chemisorption is hard in most reactions. Some of the features which are useful in recognizing physisorption are:

- In solid-gas systems at relatively high pressures physical adsorption increases with an increase in gas pressure and decreases with increasing temperature.
- The process of adsorption is reversible, with increases in the temperature of the system resulting in desorption of the adsorbate.
- The energy of interaction between the molecules of adsorbate and adsorbent is of the same order of magnitude as the energy of condensation of the adsorptive.

In the case of chemisorption the following features are useful:

- The chemical nature of the adsorbent is altered by surface dissociation or reaction, thus making it irreversible.
- The rate of the reaction increases with increasing temperature up to a critical point after which the reaction rate may start decreasing.
- There is no change in adsorption rate when small changes in the pressure are made but at high pressures the reaction rate increases.

1.4.1 Physical Adsorption

Researchers have long been trying to explain the underlying principles of physisorption. Polanyi was the first to explain these phenomena when he the depicted adsorbed state as a thick multimolecular film under the influence of long-range forces emanating from the surface. Later, Langmuir thought of adsorption as from a monolayer instead of multilayer process on the surface. The third approach, based on Kelvin equation, illustrate the effects of capillary condensation as described by Dubinin. It was not until 1938 that the first attempt to calculate the surface area of the carbons was published by Brunauer-Emmett-Teller (the BET theory of multilayer adsorption)[61]. Even though this theory has been subjected to considerable amount of criticism, it has remained the most common method for determining surface areas of adsorbents, catalyst, and other porous materials.

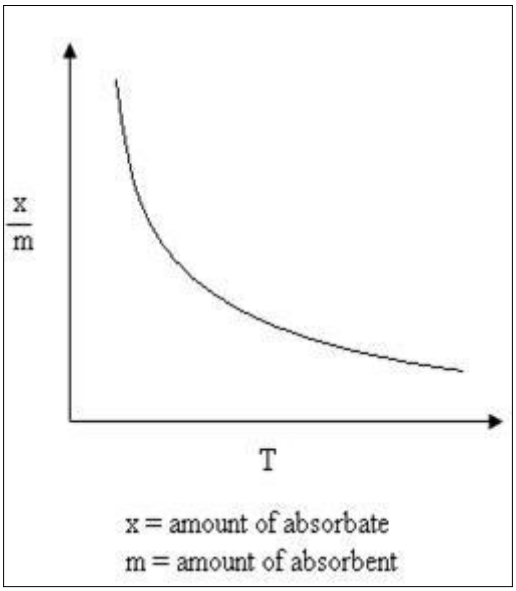

Figure 1.2*: Change in physical adsorption (x/m) as a function of temperature (T).*

Physical adsorption occurs in three steps. In the first step, the gas molecules near the surface are adsorbed on to the surface of the solid. As the outer surface of the solid fills up, the gas molecules diffuse into the micropores of the solid. Most of the adsorption will take place here as most of the surface area is found within the pores of the solid. Lastly, the gas molecules are physically adsorbed onto the surface of the porous walls[62].

The governing forces involved in physisorption are van der Waals forces. These forces are normally thought of being weak interaction forces but can play an important role in physisorption. Physical adsorption occurs when the inter-molecular attractive forces between the gas and the solid surface is greater than those between the gas-gas phase. No more then 40-50 kJ mol^{-1} of energy is needed for physical adsorption to take place. This process is quick and may results in a formation of a monolayer or multilayer on the solid surface. The resulting adsorption is exothermic; thus, heat is released during the reaction. Due to the low activation energy of the process it is reversible. The process of physisorption depends on the nature of the adsorbate. In

general, adsorbate with high critical temperatures is most likely to be physically adsorbed than ones with lower critical temperature. For example, SO_2 with a critical temperature of 630 K is adsorbed more than CH_4 (critical temperature of 190 K) over activated carbon.

The electrostatic effect that produces van der Waals forces depends on the polarity of both the gas and solid molecules. All molecules are either in polar or nonpolar state based on the chemical structure. This property of the molecules plays an important role in determining how physical adsorption takes place. There are three different methods in which physical adsorption can take place: (1) orientation effect, (2) dispersion effect, and (3) induction effect. The orientation effect takes place between polar-polar molecules. The negative charge of one molecule attaches to the positive charge of the other. An example is the removal of H_2O vapor (polar) from an exhaust stream using silica gel (polar). Dispersion effects take place between nonpolar-nonpolar molecules. It is well known that nonpolar molecules do not have a permanent dipole but have oscillating dipoles. In this instance, when two oscillating dipoles come close to each other, their total energy decreases, resulting in a paired system where each fluctuates in phase with each other. A good example of this system is the adsorption of organic vapors onto activated carbon. Attraction between polar-nonpolar molecules is known as the induction effect. A polar molecule can induce polarity on a nonpolar molecule when they come in close contact. The effect is small in comparison to the other two[62].

1.4.2 Chemical adsorption

A chemical bond involves sharing of electrons between the adsorbate and the adsorbent known as chemisorption. This bond is much stronger than that of physical adsorption, requiring nearly 40-240 kJ mol^{-1}. Due to the bond strength, chemisorption is difficult to reverse. Unlike physical adsorption, chemisorption is highly selective and occurs only between specific adsorptive

and adsorbent species. In most instances, chemical adsorption occurs on the external surface of the carbon, as a single layer process. Chemical adsorption can take place at any temperature. Increases in temperature lead to increases in adsorption initially, but the rate begins to decrease after a critical temperature point (Figure 1.3).

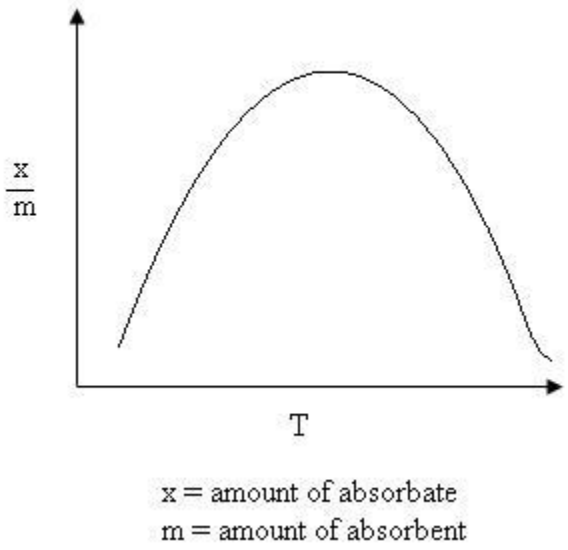

Figure 1.3: *Change in chemisorption as a function of temperature (T).*

Two chemisorption isotherms techniques can be used to characterize chemisorption: (1) static volumetric chemisorption and (2) dynamic chemisorption. The volumetric technique can be used to obtain high-resolution measurements of the isotherms from low to atmospheric pressure at wide ranges of temperature. The more often used method is the dynamic chemisorption technique. After the sample is degassed, small quantities of an adsorbant is injected until the sample is saturated. The quantity of adsorbant taken up by absorbent is measured by a TCD. The number of molecules of gas chemisorbed is directly related to the active surface area of active material.

1.5 Objective

The objective of this study is to develop a green processing technology for upgrading biogas in order to help local communities dealing with rising energy costs. In order to do this the following work was conducted:

- Assessment of local biogas potential on Long Island, NY, including surveying all potential biogas sources such as, landfills, wastewater treatment plants, farms and composting facilities. The feasibility of such production was performed.
- Development of a method to improve biochar performance as a purification media in a biogas stream. This involves further activation of biochar by means of environmentally friendly methods, such as, activation via CO_2, and O_2. Physical and chemical characterization of pre-activation and post-activated biochars were conducted using SEM, XRD, and FTIR. Effects of activation on removal capacity of H_2S were studied.
- Development of a metal oxide catalyst for removal of H_2S in biogas. An iron oxide catalyst was produced using sonochemical synthesis. The catalyst was characterized using a SEM, TEM, XRD, surface analysis and FT-IR. The catalyst was tested for H_2S removal.
- Development of computer simulations to aid in system optimization and prediction ofbiochar performance.

Chapter 2: Instrumentation and Experimental Design

2.1 Instrumentation

2.1.1 Gas Chromatography (GC)

A GC can be used to analysis various gas and liquid samples. Two Gow-Mac series 580 GCs equipped with TCD and FPD detectors were utilized in this study. The TCD was used to analyze CH_4, CO_2, CO, N_2 and H_2 gases. The FPD was used for detecting ultra-low concentrations (down to 200 ppb) of sulfur compounds. The FPD works on the same principal as a FID. Where the FID measures ions produced by organic compounds during combustion, the FPD analyzes the spectrum of light emitted by a compound as it luminesces in the flame. The detector housing is light tight to insure only the light from the flame is seen by the photomultiplier tube. The FPD used in this study is equipped with 394 nm band gap filter to allow detection of sulfur-containing compounds (see Table 2.1)[63, 64]. The signal was captured and analyzed via DataApex Clarity data acquisition board and software.

GC Model	Detector	Column	Carrier Gas	Analysis
Gow-Mac series 580	FPD	Hayesep R (4' x 1/8")	He	Gaseous sulfur compounds
Gow-Mac series 580	TCD	Mol. Sieve 5Å (8' x 1/4")	N_2	H_2
	TCD	Mol. Sieve (9' x 1/8")	He	N_2 and CO
	TCD	Carboxen 1000 (5' x 1/8")	He	CH_4 and CO_2

Table 2.1: *Instruments on which gas analysis was carried out on.*

2.1.2 Fourier Transform Infrared Spectroscopy (FTIR)

FTIR is a quick non-destructive method for identifying chemical bonds (functional groups) in organic or inorganic compounds. The infrared measurements were done on a Parkin-Elmer FTIR - Frontier spectrophotometer equipped with a universal attenuated total reflectance (UATR) module. A small amount of powder sample was directly put onto the UATR lens for analysis. The data was used to identify the phase of the solid catalyst being tested.

2.1.3 Powder X-Ray Diffraction (XRD)

X-Ray Diffraction is a commonly used technique to study crystal structure and atomic spacing. It is based on principle of constructive and distractive interference that take place when an incident x-ray beam hits a solid sample. When the diffraction pattern satisfies Bragg's Law (Eq. 11) the signal is recorded and processed.

$$n\lambda = 2d * \sin(\theta) \tag{11}$$

where n is an integer, λ is the wavelength, d is the spacing between planes in the atomic lattice and θ is the angle between the incident ray and scattering plane. In this study, XRD measurements were conducted for phase identification of the solid samples.

2.1.4 Surface Area Analysis

Surface area analysis has become an important tool in number of different fields including pharmaceuticals, catalysts, and activated carbons. The surface area of a powder is determined by the physical adsorption of a gas onto the surface of the sample at liquid nitrogen temperatures. The choice of gas used in the measurement is based on the sample being characterized. N_2 and

CO_2 are the two most often used gases for analysis. The adsorption data is usually plotted into adsorption isotherms. The graphical representation of the adsorption data describe the physical characteristics of the sample. There are six basic forms of adsorption isotherms (Figure 2.1).

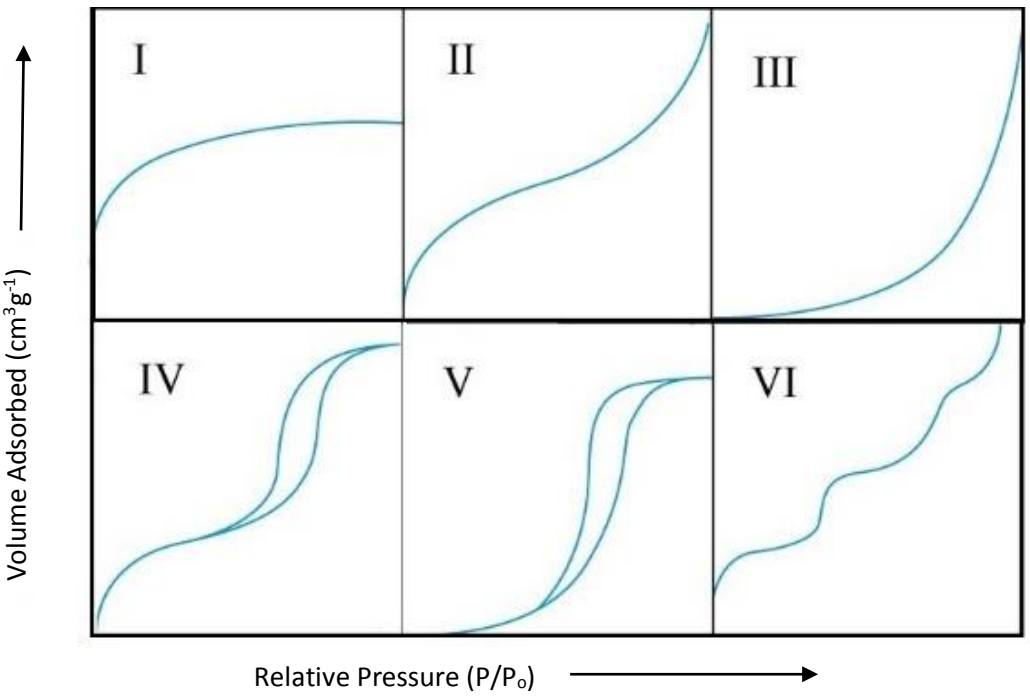

Figure 2.1: *Six observable forms of adsorption isotherms.*

A type I isotherm is also known as pseudo-Langmuir isotherm. The steep increase at low pressure means adsorption is taking place in narrow highly porous material, most likely micropores. The plateau indicates the filling of micropores and beginning of adsorption on the external surface at a very slow rate. This type of isotherm is associated with adsorption on activated carbon. A type II isotherm shows the formation of a monolayer at relatively low pressure resulting in the bend and a low slope region in the middle as a sign of multilayer adsorption. The material is saturated at a relatively high pressure. This type of isotherm corresponds to non-porous solids which have macro size pores. Type III and V isotherms do not exhibit any bend as in Type II isotherm. This indicates the lack of monolayer formation. This results from greater interaction

gas-gas interaction then gas-solid interaction. Type IV isotherm is closely related to Type II isotherm. Type IV shows a formation of hysteresis due to adsorption and desorption taking placed on different paths. Lower path of the hysteresis loop shows adsorption taking placed with multilayer formation. The upper path indicates capillary condensation in meso and macropores. Type VI isotherm corresponds to non-porous adsorbent with uniform surface. The uptake of gas takes place layer by layer leading to step like formation.

The BET theory is commonly used to evaluate the gas adsorption data and generate estimates of specific surface area. The BET equation is given as following:

$$\frac{P}{V(P_o - P)} = \frac{1}{V_m C} + \frac{c-1}{V_m C}\frac{P}{P_o} \tag{12}$$

where P_o is saturation pressure of the gas (1 atm pressure if carried out at atmosphere); V is the volume of the gas adsorbed per unit mass of material at pressure P; V_m is the volume of gas required to cover a unit mass of the material with a complete monolayer of gas; C is a constant. This linear equation can easily be solved and is plotted in terms of $\frac{P}{V(P_o-P)}$ versus $\frac{P}{P_o}$, also known as the BET isotherm. The total surface area is given by:

$$Total\ Surface\ Area = \frac{a_o N_A V_m}{V} \tag{13}$$

where a_o is the cross sectional area of gas molecule being adsorbed, N_A is Avogadro's number, and V is the molar volume of adsorbing gas. Finally the specific surface area of the powder is calculated using:

$$Specific\ Surface\ Area = \frac{Total\ Surface\ Area}{Mass\ of\ the\ Sample} \quad (14)$$

An alternative theory referred to as the Langmuir equation can also be applied to calculate surface area. The Langmuir equation is usually preferred when nonporous or microporous samples are being analyzed since the theory predicts only monolayer formation on the surface of the sample. The linear form of the Langmuir equation is given as (Eq. 15):

$$\frac{P}{V} = \frac{1}{V_m b} + \frac{P}{V_m} \quad (15)$$

where b is the Langmuir constant. The Langmuir isotherm is plotted as $\frac{P}{V}$ versus P. Both Langmuir and BET equations result in graphs with a straight line. If sufficient data points are collected, the mean pore volume and pore size distribution can be calculated using *t*-plot method and Dubinin-Radushkevich (DR) theory respectively.

Before a sample can be analyzed, it must be degassed to remove any impurities from the surface. This is usually done by heating the sample to an elevated temperature in conjunction with vacuum or continuously flowing inert gas. This process is very important in order to generate the most accurate and repeatable results. In this study, surface area calculations were conducted using Micromeritics TriStar 3000 surface analyzer under N_2 adsorption at -196 °C. The samples were degassed for four hours at 350°C under continuous He flow before each analysis.

2.2 H_2S removal unit

An indigenous unit was built for testing H_2S removal. The testing unit is show in Figure 2.2. A pyrex glass column (6.25 mm o.d x 170 mm) served as the packed bed reactor. Electric

heating tape was wrapped around the reaction column to provide uniform heating to the sample. A K-type thermocouple was used to monitor the temperature of the packed-bed. Sample ports were installed at the inlet and outlet of the reactor column to allow continuous monitoring of H_2S concentration. The flow meter was used to control biogas flow into the reaction column. Pressure transducers were installed near the inlet and outlet of the system to monitor the system pressure. Due to the hazardous nature of biogas all reactions were carried under the fume hood.

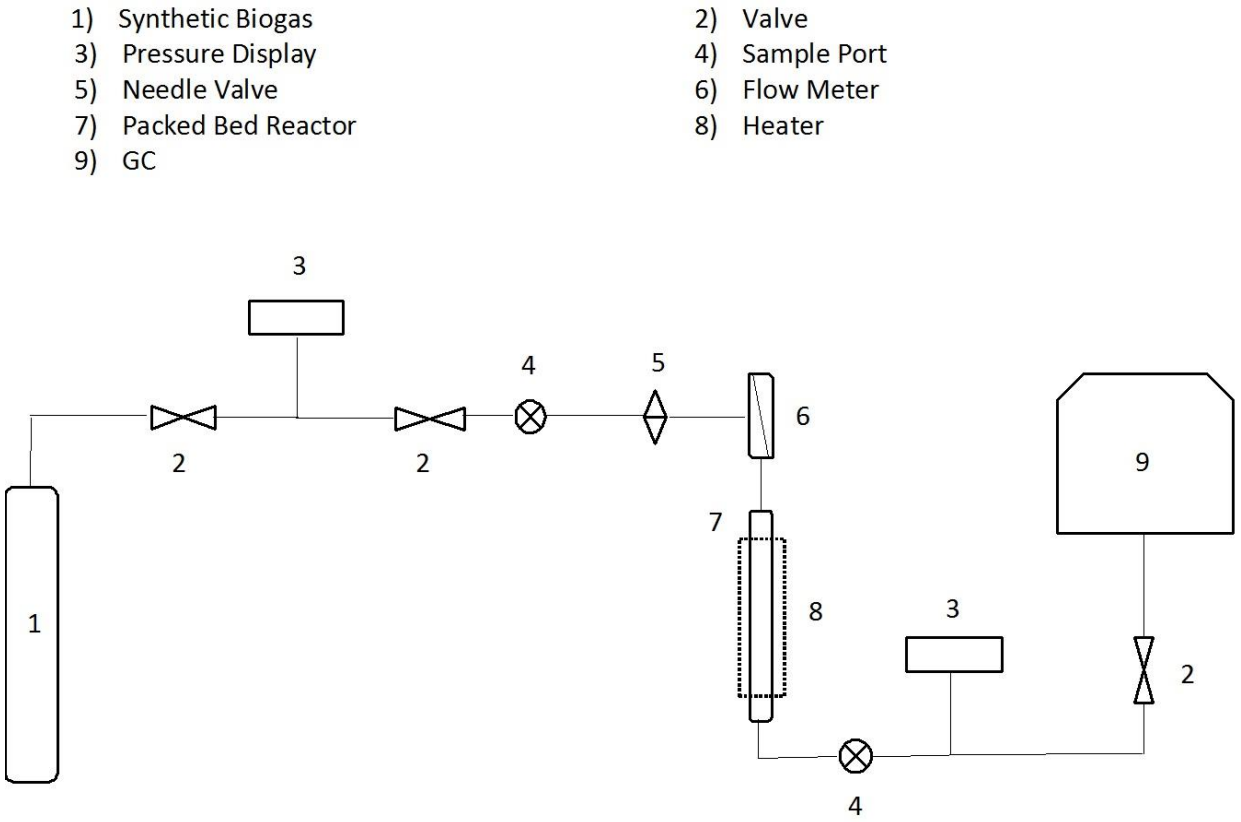

Figure 2.2: *The test unit was built for H_2S adsorption testing.*

Chapter 3: Biogas Potential on Long Island, New York: A Quantification Study

3.1 Introduction

Fossil fuels currently provide 86% of the world's energy needs and will continue to do so until suitable replacements are discovered. Burning fossil fuels releases GHGs, mostly in the form of CO_2, which results in trapping of heat and thus contributes to global climate change. Energy related CO_2 emissions are forecasted to grow from 32.5 billion metric tons in 2013 to 43.2 billion metric tons by 2035, an increase of 25%. During the same period the total world energy consumption is projected to increase by 56% as fossil fuels reach peak production rates. The price of oil is projected to rise from $79 per barrel in 2007 to $133 per barrel in 2035[1, 65]. Moreover, widespread agreement across all U.S. constituencies to reduce dependency on foreign fuels has vastly increased support to develop domestic renewable energy sources. This combination of environmental, economical, and political factors has led to increased interest in alternative and renewable fuels.

In 2004, New York State adopted a Renewable Portfolio Standard (RPS), which requires that 25% of the state's electricity come from renewable sources by 2013. The standard identifies two tiers of eligible resources: a "Main Tier" and a "Customer-Sited Tier." The main tier is mandatory and is to account for 24% of the standard. Eligible sources include biogas, biomass, liquid biofuel, fuel cells, hydroelectric, solar, ocean or tidal power, and wind. The customer-sited tier will make up the remaining 1% of renewable energy sales and is to come from voluntary green market programs. In order to meet the 25% target, the state will need to add approximately 3,700 MWs of electricity generated from renewable resources. Reaching program goals is forecast to

reduce air emissions of NO_x by 6.8%, SO_2 by 5.9%, and CO_2 by 7.7%, with a greater proportion of emission reductions expected in New York City and LI[66].

Unfortunately, six years after the RPS was adopted, LI is not on track to achieve its goals, nor has it formulated plans to do so. In 2007, residential, commercial, and industrial electricity consumption increased by 2.5% over the previous year, corresponding with an overall 21% electricity use increase over the previous decade. In that decade, residential electricity use grew 27% while population increased by less than 9%. In order to achieve its RPS target, LI would need to reduce its annual electric consumption growth to 0.4%[67].

LI extends 118 miles into the Atlantic Ocean east from Manhattan, making it one of the longest and the largest islands in the U.S (Figure 3.1). With a population of approximately 2.8 million, LI is one of the more densely populated areas in the U.S. LI is often defined as comprising of Nassau and Suffolk counties, excluding areas that are part of New York City. The Long Island Power Authority (LIPA) provides electric service to over 1.1 million customers on LI but it does not own any power plants. The maintenance of LIPA's transmission and distribution systems is the responsibility of National Grid USA, which delivers 20 TW-hrs of electricity annually. National Grid manages nearly all local electrical generation and natural gas distribution on LI.

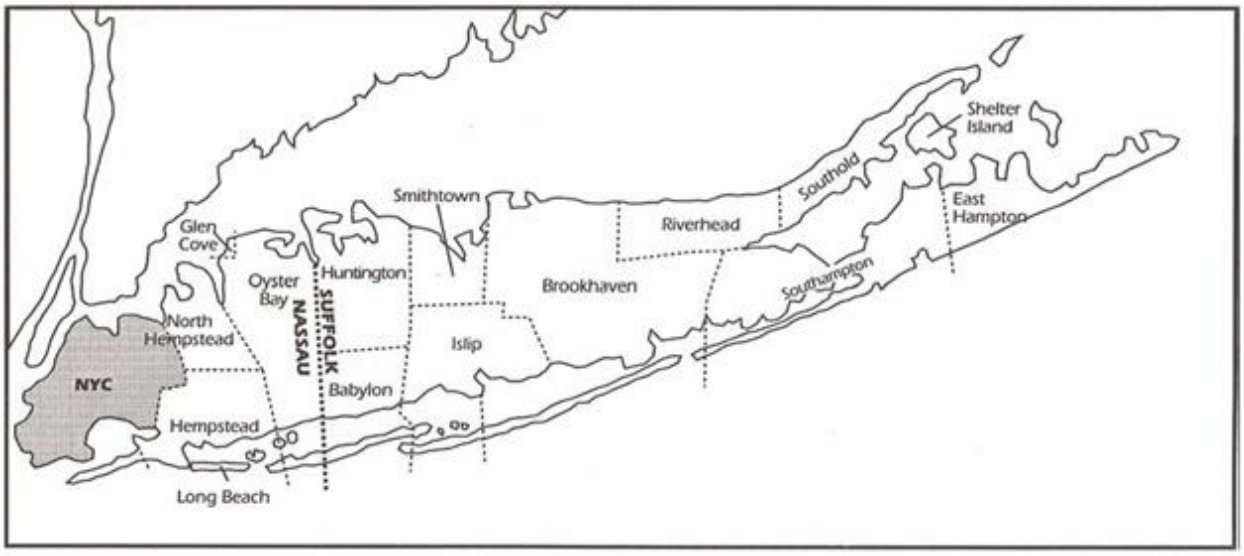

Figure 3.1: *Map of Long Island and its municipalities.*

LI is not self-sufficient for electricity, importing 41% of the electricity it consumes, transported through long-distance transmission lines and undersea cables. Long distance transmission lines are known to be inefficient, adding to already high local electrical costs. The remaining 59% of local electricity use is provided by power sources located on LI; however, almost all fuel sources to generate the electricity are imported. Therefore, nearly all electricity used on LI is either imported or made with imported fuel. Most suburban areas in the US are similar in that they rely on fuel sources located outside of their immediate vicinity. National Grid operates five of the largest power plants on LI with generating capacity of 4,000 MW. The three largest power plants on LI are outdated and inefficient; however, they have the ability to switch between oil and natural gas. There is some current exploitation of waste sources to create electricity with four waste-to-energy incinerators, and two landfill gas-to-energy plants. The four incinerators generated a combined 1,042 GW-hrs of electricity in 2009, while landfill gas-to-energy plants made 3,424 MW-hrs of electricity. Production from renewable energy sources such as solar and wind in 2009 produced a minor portion of LI's power (10 MW-hrs in 2009) (Figure 3.2).

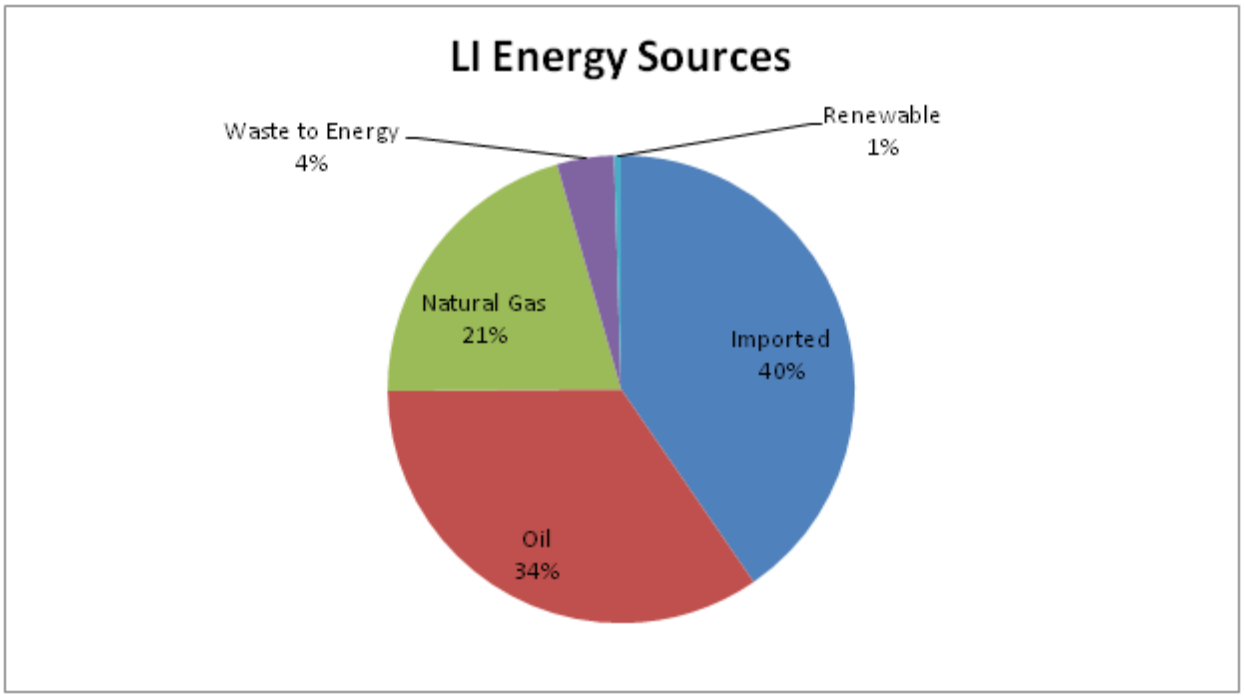

Figure 3.2: *Long Island's energy sources: 41% imported, 35% oil, 21% natural gas, 4% waste-to-energy incinerator, and 0.5% renewable (does not add up to 100% due to rounding).*

The transition to alternative energy sources such as solar and wind requires major restructuring of the electrical grid and the creation of energy storage. Biofuels, as renewable energy, are closer to immediate implementation and so have received much government support although many biofuels do not exactly match current fuel needs. However, there exist large distribution networks for natural gas which can be used for biogas, as it can be purified to methane. Therefore, biogas can serve as a ready-to-use source of fuel that has low CO_2 emissions and avoids the use of imported energy products. An important consideration, however, is the extent that local biofuel sources can displace the use of other energy.

Degradation of biomass under anaerobic conditions leads to the formation and release of biogas. Biogas typically contains 50 – 70% CH_4, and 30 - 50% CO_2, with the balance being trace gases[68]. Anaerobic digestion is a natural phenomenon that can occur in landfills and wetlands. It

can also be reproduced in a controlled manner in an AD. Anaerobic digestion offer the possibility of using a large variety of waste products, including municipal solid waste, sewage sludge, manure, food waste, and crop residues to produce biogas. In addition, anaerobic digestion is a well understood technology that can operate on large scales[20, 69].

Although the technologies needed to produce biogas and generate electricity from it are well understood and demonstrated they are often not implemented in situations where they may be feasible. We believe this stems partly because the quantity and quality of the resources are not well appreciated. If the resources were well documented and defined, local governments or private enterprise might take action to realize the opportunities, as biogas resources that are locally available and fill local needs would be extremely useful. Thus, we have undertaken this work as a template for other areas to rapidly create or approximate biogas potentials in places such as suburban U.S. that are not usually thought of as sources of renewable energy.

In this paper, we identify potential sources of biogas in addition to ones currently being exploited, and we quantify the amount that can be produced on LI, based on previously published data as well as data provided by local governments and private companies[70-72]. The report sums the total biogas generating potential from sources such as WWTPs, solid waste management facilities (landfills), agricultural residues, and yard waste. We believe this is the first published complete evaluation of the biogas energy potential for primary organic residues to be made on a local scale. This is significant because production of biogas is dependent on locally available biomass sources.

3.2 Background

3.2.1 Biogas Production from Anaerobic Digestion

3.2.1.1 Anaerobic Digestion of MSW in Landfills

Anaerobic digestion in landfills produces biogas commonly known as landfill gas. On average, landfill gas is composed of 50% CH_4 and 50% CO_2 with traces of other gases[73]. The quality and quantity of biogas at landfills is a function of the types of waste in place, the age and quantity of the waste, and the climatic conditions in which the landfill is located. For instance, landfills in hot, dry areas produce less biogas because water inputs to the waste are less[74]. Nearly 22% of the anthropogenic-sourced CH_4 released into the atmosphere in the U.S. comes from landfills, making it the third-largest human-related source[75].

Degradation of MSW under anaerobic conditions depends on the characteristic of the waste. For instance, paper and wood products are composed of celluloses and hemicelluloses, which are the major fast biodegradable polymers in MSW; the other major organic component, lignin, is slow to degrade under methanogenic conditions. Eleazer et al.[76] defined the amount of cellulose, hemicellulose, lignin, and volatile solids in grass, leaves, branch, food, coated paper, old newsprint, old corrugated containers, office paper, and MSW, which allowed projections of the total CH_4 yield; CH_4 potential was measured under optimum anaerobic decay conditions in a laboratory study (Table 3.1).

Product	Cellulose	Hemicellulose	Lignin	Volatile Solids	Yield (ml of CH_4/dry g)
Grass	26.5	10.2	28.4	85.0	114.4
Leaves	15.3	10.5	43.8	90.2	30.6
Branch	35.4	18.4	32.6	96.6	62.6
Food	55.4	7.4	11.4	93.8	300.7
Coated Paper	42.3	9.4	15	74.3	84.4

Old Newsprint	48.5	9	23.9	98.5	74.33
Old Corrugated Containers	57.3	9.9	20.8	98.2	152.3
Office Paper	87.4	8.4	2.3	98.6	217.3
MSW	28.8	9.0	23.1	75.2	92.0

Table 3.1: *Composition data for different items present in the waste stream with corresponding CH_4 yield*[76].

3.2.1.2 Anaerobic Digestion of Other Landfilled Wastes

Other materials besides MSW are often landfilled. C&D debris is solid waste resulting from construction, remodeling, repair and demolition of buildings, roads, bridges, and land clearing. C&D is comprised of large amounts of wood, concrete, roofing shingles, drywall and cardboard (Table 3.2). Land clearing debris is often differentiated from C&D, but is sometimes included in the C&D category. Land clearing debris includes vegetative matter, soil, and rock resulting from land clearing and grubbing, utility line maintenance, or seasonal or storm-related cleanup, such as trees, stumps, brush, leaves, and wood chips. Land clearing debris does not include yard waste which is collected curbside. Although much C&D is degradable, its waste gases are commonly contaminated by H_2S, generated from anaerobic decay of drywall.

Component	Percent in Dry Weight
Wood	33.2
Concrete	29.2
Roofing Shingles	13.7
Drywall	12.4
Cardboard	8.0
Others	3.5

Table 3.2*: Composition of construction and demolition as estimated by Jang and Townsend*[77, 78].

The decay of these materials depends on how much is readily degradable. Approximately 41% of C&D is degradable, mostly as wood and cardboard[77, 78].

3.2.1.3 Enhanced Digestion of Landfilled Leachate

Landfill leachate can potentially be used to enhance gas generation. This is done through pumping the leachate from the collection layer at the bottom of the landfill to infiltrate back through the waste mass, a process known as leachate recirculation. Leachate recirculation has shown to reduce waste-stabilization time, enhance gas production and improve leachate quality, through reduction in COD. It also increases waste volume reduction rates at landfills[79, 80]. Enhanced gas production has been reported between 4-12 times due to leachate recirculation versus non-circulation in controlled bioreactors[79, 81, 82]. US-EPA may allow leachate recirculation at landfills where modern liner systems are in place.

3.2.1.4 Digestion of MSW in Anaerobic Digesters

In an AD, organic matter in MSW (such as food waste, yard waste, cardboard, and paper) (Table 3.3) is consumed by the bacteria in absence of oxygen, producing biogas, solid byproducts, and reclaimed water. Treatment of MSW in ADs can be broken into three parts: pre-treatment, digestion of the feedstock, and post-treatment. The need for pre-treatment and post-treatment is determined by the particular digestion technology being used and the overall objective of the user. Pre-treatment requires the separation of organics from other waste and the size reduction of the feedstock, while post-treatment requires the disposal of residuals after digestion.

Material	NYS Estimated Waste Discarded (%)
Paper	29.9
Coated Paper	1.6
Office Paper	2.4
Newspaper	1.6
Corrugated Paper	6.4
Others	19.3
Organics	25.1
Food Scraps	18.2
Yard Trimming	2.4
Wood	4.5

Table 3.3: *Estimated amount of paper and organics discarded comprise of 55% of the total waste landfilled in suburban New York*[83].

Use of full scale ADs for MSW management is practiced extensively in Europe[84-86]. Many reports in literature suggest full scale plants typically achieve biogas yields of 0.10-0.15 m^2/wet kg of waste on average. However, biogas yield depends greatly on reactor configuration and source of feedstock. For instance, the Valorga plant in Netherlands produces much 0.93 m^3/wet kg of biogas, while the Dranco plant in Germany only yields 0.147 m^3/wet kg[85, 86].

3.2.1.5 Digestion of Yard Wastes in Anaerobic Digesters

Anaerobic digestion of yard waste reduces waste volumes, produces CH_4 as decomposition gas and the process byproducts can also be used as a soil amendment. Overall, anaerobic digestion is a net energy producer. In addition, anaerobic digestion requires less space than many large-scale composting facilities. Waste decomposition estimates from Table I can be used to determine gas generation, assuming brush produces 46.6 ml of CH_4 g^{-1}.

3.2.1.6 Digestion of Sewage Sludge in Anaerobic Digesters

Digesting WWTP sludge to generate energy is a common practice throughout the world, and produces a biogas that is typically 60% CH_4 and 40% CO_2. WWTPs that do not utilize ADs have to incinerate or compost sludge, which can add 20% to operational costs. In addition, biogas can be used to generate electricity, offsetting the annual U.S. WWTP power demand of 21 billion kw-hrs $year^{-1}$, and any excess electricity can be sold for profit. A projection of sludge processing at WWTPs can be made based on the number of people connected to WWTPs. Given wastewater generation rates of 450 liters per person per day, and that total solids present in an average sanitary wastewater is 800 mg L^{-1}, and assuming 75% of solid in sludge is volatile, and 50% reduction in

volatile solids after digestion, and 16 m^3 of CH_4 produced per kg of volatile solids destroyed[23], the per capita generation of biogas is 2.3 m^3 of CH_4 per day.

3.2.1.7 Digestion of Agricultural Residues in Anaerobic Digesters

Nationwide, agricultural wastes are increasingly used as feedstocks for ADs, especially for livestock manure management in the United States. This has relatively low yield of biogas (cow manure produces 0.025 m^3 kg^{-1}, and pig manure 0.036 m^3 kg^{-1}) because the organic dry matter content is low (2-10%). Digestion of co-substrates, such as crop residues, can help increase biogas production. Quantifying biogas potential from diverse agriculture residues is difficult, but one generalized estimate is 0.23 m^3 of CH_4 per m^2 per year[87].

3.3 Methods

The assessment of the energy potential of different organic waste is based on the amount of each that is generated on Long Island. Local and state tonnage data were used to calculate MSW, and C&D generation potentials. Biogas potential from MSW and C&D was calculated based on the chemical characteristics of the waste using:

$$B_l = W_l \times P_l \times Y_l, \quad (16)$$

where B_l is total CH_4 yield, W_l is total weight of the waste, P_l is percentage of degradable waste in question, and Y_l is CH_4 yield per gram (see Table 3.1). The potential for gas generation from WWTP sludge digestion was calculated based on the percentage of population connected to WWTPs using:

$$B_w = N \times P_w \times Y_w \quad (17)$$

where B_w is the total CH_4 yield, N is the population of the area, P_w is the percentage of the population connected to WWTPs, and Y_w is CH_4 yield per person.

The potential for gas generation from agricultural residues was calculated based on the area of farmland devoted to crops using:

$$B_a = A \times P_a \times Y_a \quad (18)$$

where B_a is the total CH_4 yield, A is the total area of agricultural land, P_a is the percentage of farmland devoted to crops and Y_a is the CH_4 yield per meter. Farmland area was derived from local agricultural extension offices.

In some cases, current biogas generation from a particular waste source was used, instead of creating an estimate of potential generation. Otherwise the background research provided a framework for evaluating any area's biogas potential. It was relatively straightforward, but not particularly easy to collect the necessary information to populate the framework. For LI, for instance, the fragmented nature of local governance means that 15 different authorities manage solid waste. There are two primary sewage plant managers and approximately ten other wastewater authorities, and no single local government agency tracks agriculture. There are some unofficial aggregations of information, but finding appropriate data required contacting the correct municipal officials who had the data at hand. For many areas, replicating this work will be much simpler.

3.4 Results

3.4.1 Landfills

LI is a special case for landfills. Due to observations of leachate plumes in the sandy sole source aquifers on LI, the New York State legislation passed a law banning landfilling of MSW on LI to take effect in 1990. All local landfills were in compliance by 1995[72]. Most landfills closed to meet the law; four remained open to manage wastes such as incinerator ash and C&D.

Biogas production and extraction from landfills has been studied extensively[88, 89]. Two landfills collect gas from areas that formerly received MSW. The Brookhaven landfill has been closed to MSW since 1996 but the 8 billion kgs of MSW in place has generated gas to produce 350,000 MW-hrs of electricity. Gas generation has declined considerably since 1996, and in 2009 the landfill generated 64 MW-hrs of electricity from 56,633 m^3 of gas collected[70]. The landfill located in Oceanside, which has been closed for the past two decades, collected 2.63 million m^3 of gas and generated 3,360 MW-hrs of electricity in 2009[71]. There are more than 40 other closed landfills located on LI, four of which have been identified as potential candidates for energy recovery projects by the US-EPA[73]. The US-EPA believes that gas recovery can be accomplished if a landfill has enough waste in place as well as meeting other criteria. Most of the closed landfills have been deemed unfavorable for gas recovery because they may be smaller than 25 acres, closed for more than 25 years, are "low height" landfills, and/or are not capped.

3.4.2 C&D

There are three active landfills on LI that mange C&D. Much of the C&D managed by the LI landfills is generated in New York City. In 2008, nearly 1.5 billion kgs of C&D was landfilled

on LI. Using the degradation potential of these materials (Table 3.1) and Eq. 16 the estimated annual potential of CH_4 yield from C&D at active landfills is 42.8 million m^3 (Figure 3.3).

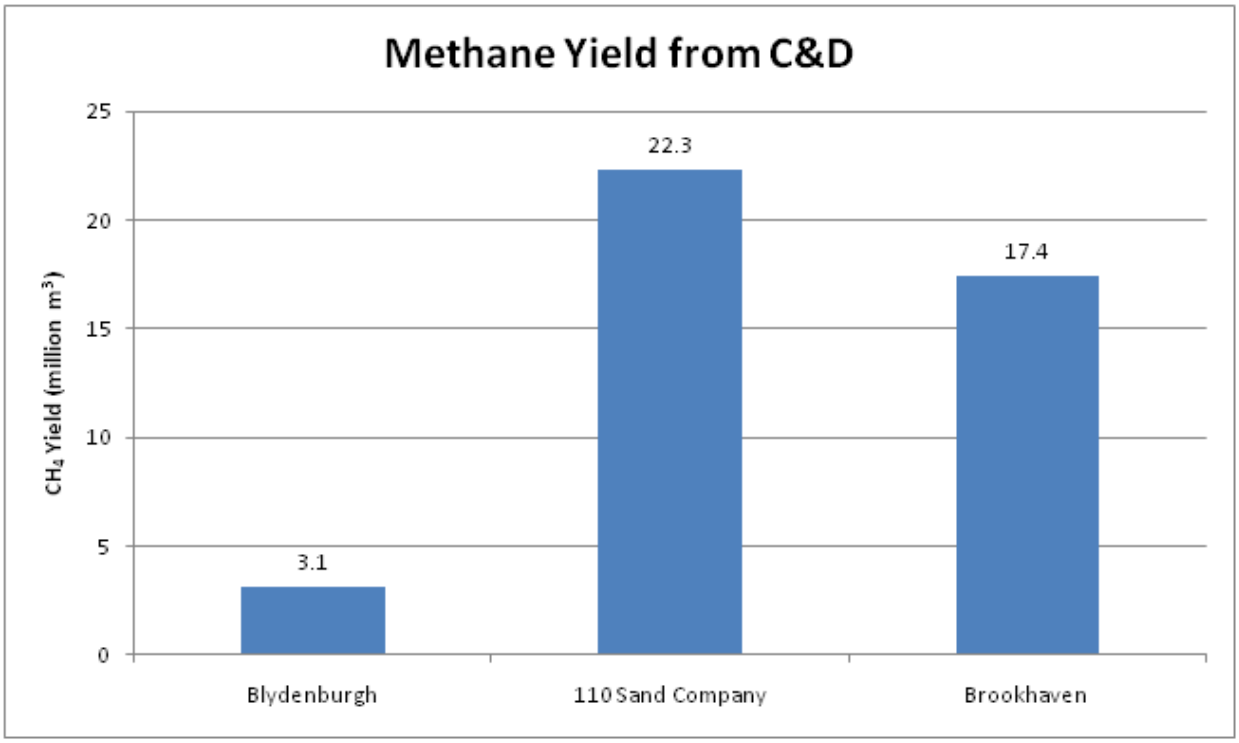

Figure 3.3. *Estimated amount of methane yield annually from construction and demolition from active landfills.*

The potential gas generation from C&D can be compared to actual output at the three landfills which contain LGRF. In 2009, 42.48 million m^3 of biogas was collected; however, CH_4 concentrations were approximately 30%, meaning the calculated 42.8 million m^3 of CH_4 is three times higher. In addition, the gas was heavily contaminated by H_2S (up to 8,000 ppm). All three landfills currently flare the C&D gas. This reduces GHG impacts, but fails to utilize any energy potential in the gas.

3.4.3 Enhanced Landfill Degradation

In 2009, the landfills produced 253 million liters of leachate, which were treated at the local WWTPs. Recirculation of leachate could enhance C&D degradation and reduce leachate

treatment costs. It can also increase landfill gas generation by much as 4-12 times the current level. However, the estimates in Table 3.1 for gas generation from particular waste elements are optimized, as they are based on laboratory experiments. The actual degradation of waste in ADs and, especially, landfills, is likely to be less. In a landfill, for instances, distribution of moisture through the wastes is uneven, and much waste is enclosed in plastic bags (therefore relatively unavailable for decay). Although recirculation of leachate could enhance degradation in a landfill by redistributing moisture, it does not seem appropriate to increase the theoretical yields listed in Table 3.1. Landfill gas recovery is only small portion of the biogas potential on LI. In other areas of the country where wastes are still landfilled, factoring in reduced decomposition of matter in landfills, and the potential to increase the degradation through leachate recirculation will be more important.

3.4.4 MSW

At least partially because of the landfill ban, LI municipalities built four waste to energy incinerators. Long Island also has a relatively well developed recycling and yard waste composting infrastructure. Thus, it was estimated that 42% of LI's MSW was incinerated and 28% was recycled. The remaining 30% was transported off LI for landfilling. Only the transported portion of the waste has been considered for biogas production. Based on the assumed composition of these materials (Table 3.3) and Eq. 16, CH_4 potential for MSW if it was managed through anaerobic digestion would be 44.9 million m^3 (Figure 3.4).

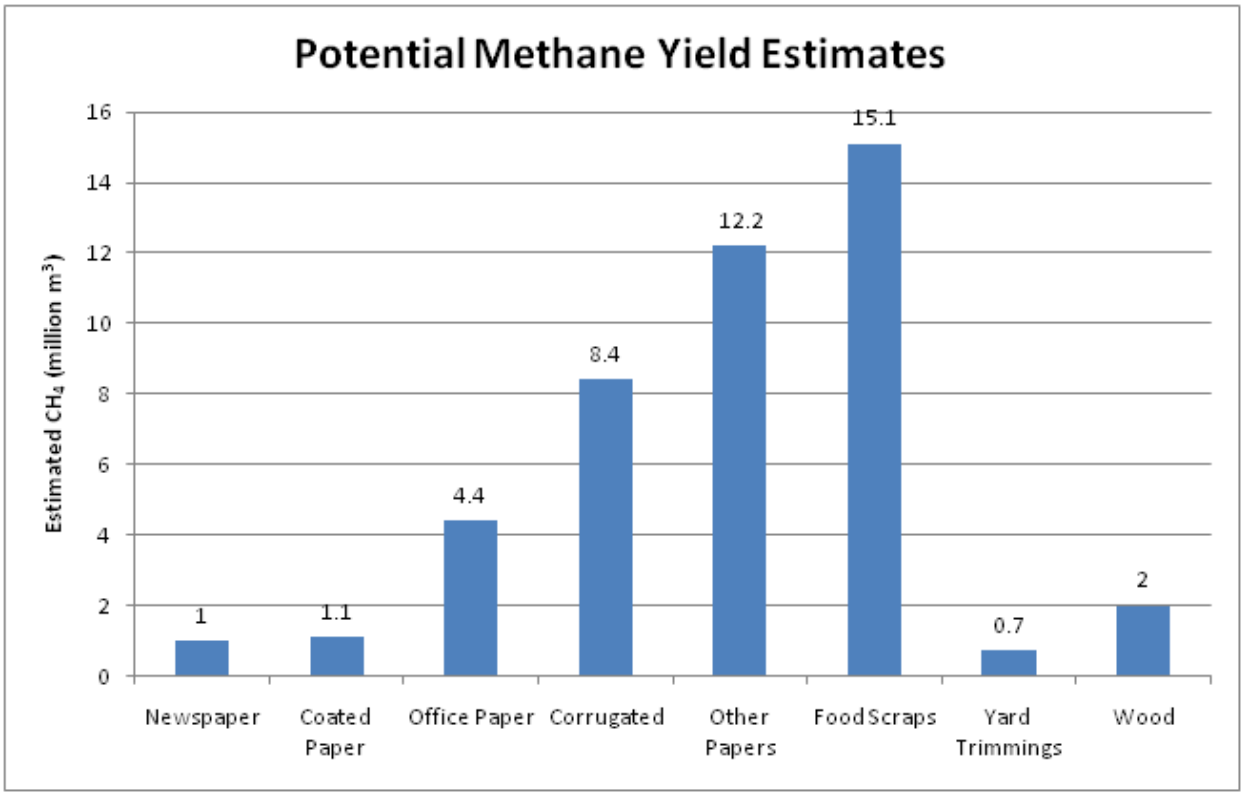

Figure. 3.4: *Potential methane yield estimates per year from the transported paper and organic waste on Long Island.*

3.4.5 Yard Waste

Long Island generates approximately 365 million kgs of yard waste annually, of which 65% was leaves and 35% was brush. Most yard waste was recycled through composting. Composting is a process where organic matter is digested by aerobic decomposition. It requires energy for equipment and transportation, but has no energy output and produces CO_2 [90]. The byproduct of composting can be used as a soil amendment. However, if the yard waste were diverted from composting to digestion, based on the assumptions for yard waste degradation and Eq. 18, yard waste could potentially produce 4.8 million m^3 of CH_4 per year.

3.4.6 WWTPs

There are 34 conventional WWTPs and over 100 package treatment plants (for apartment complexes, shopping centers, etc.) on LI. Three of the WWTPs can be categorized as large, accepting 110-225 mld of wastewater. The two of the large WWTPs, located in Nassau County, have ADs, but only flare the produced biogas. The remaining large WWTP, located in Suffolk County, dewaters its sludge and transports it off LI for management. Several of the smaller plants (<19 mld) have ADs, but they too flare the biogas. When package treatment plants, along with septic and cesspool systems, require sludge management, the sludge is generally brought to one of the larger treatment plants as a "scavenger" waste. At 50% WWTP connection rates, approximately 207 million kg of sludge was generated annually (Eq. 17). This was a conservative estimate, as it does not include solids from scavenger waste generated by package treatment plants, septic, and cesspool systems. The CH_4 potential from AD of sludge could be 70.8 million m^3 $year^{-1}$.

3.4.7 Agricultural Residues

Although LI is primarily residential, in Suffolk County extensive agriculture still remains. In 2007 there were 144 million m^2 of farmland on LI. Nearly 75% is for crops, while the remainder are pastures, woodland, and other usage. Famers on LI prefer raising crops over livestock, and crops grown in Suffolk County account for the highest market value of any county in the nation[91]. Vegetables, sod, potatoes, and grapes were the most common crops. Ducks were the most valuable livestock, with 2 million raised annually (significantly reduced from peak production in the 1960s when most ducks in the US were raised on LI). There were relatively small numbers of horses, goats, and dairy cows present.

Using Eq. 17, 25 million m^3 of CH_4 might be produced from local crop residues. Local duck waste is currently managed through ADs, but the gas is flared due to difficulties in maintaining complicated generator equipment. 4.24 million m^3 of CH_4 appear to be generated at local duck farms.

3.5 Discussion

Thus, 234 million m^3 of CH_4 can be produced annually on Long Island (Table 3.4). This can potentially generate 2.52 TW-hrs of power, nearly 12% of total electricity consumed on LI annually. In New York State, pipeline grade natural gas has a residential value of $0.53 per m^3, which means that biogas potential found here has an estimated value of $125 million annually[92]. Its value as a transportation fuel, especially in terms of replacement value for fossil fuels, is much greater. This implies that significant investment in infrastructure and process improvements can have large returns, which may indicate economic viability. In addition, if landfill leachate recirculation were adopted at the current landfills, the amount of gas produced could be increased. Note that this estimate did not include any production at the four landfills identified by the US-EPA as good gas exploitation sites or any of the small 40 closed landfills.

Potential Source	Currently Exploited	Current/Potential CH_4 Yield (million m^3)	Optimal Use	Technology Barriers
Sludge	No	70.5	Pipeline quality gas	ADs are needed. Upgrading Tech.
LGRF	Yes	46.4	Pipeline quality gas	Upgrading Tech.
MSW	No	44.7	Pipeline quality gas	ADs are needed; Upgrading Tech.
C&D	No	43	Pipeline quality gas	Upgrading Tech.

Agriculture Waste	No	24.9	On-site electricty	ADs are needed.
Yard Waste	No	4.8	On-site electricity	ADs are needed.

Table 3.4: *The total potential of biogas from major sources on Long Island.*

Use of ADs for waste management is a well understood technology, and it can be inexpensive compared to other methods of managing wastes. However, AD reactor efficiency is more important than overall biogas yield for determining financial performance of a system. The overall biogas production rate and waste throughput rate are important determinants of a system's efficiency. The efficiency of a digester in terms of gas production per unit digester volume can be calculated by multiplying the waste throughput rate by the biogas yield. Based on this, a study of digestion of MSW in New York City found "kitchen waste" plus paper had the highest biogas yield per unit reactor volume[22, 93]. One estimate suggested a New York City MSW digester could recover costs with a tipping fee of $0.043 per kg, compared to $0.069 per kg for mass-burn incineration[94, 95].

There are some disadvantages of using ADs for waste management. Different feedstocks can affect the quality of the gas. Feedstocks that are not homogenous lead to gas streams that may contain compounds other than CO_2/CH_4 which can cause operational difficulties. For instance, large WWTPs on LI tend to manage scavenger wastes and may receive difficult-to-manage wastes such as landfill leachate or industrial waste water, although at relatively low input volumes (landfill leachate is less than 0.5% of the annual throughput at the WWTPs). Still, process upsets are apparently common enough to discourage operators from trying to produce energy from an available feedstock. Similarly, digestion of wastes currently managed at landfills produces high

levels of H_2S due to mixture of different wastes. This implies any MSW or C&D anaerobic digester plant will require a careful pre-loading sorting process. Avoidance of gas contamination at solid waste digesters in Europe is striven for by carefully sorting the waste components to be used as feedstocks, and extensive in-vessel process monitoring[96].

Removal of CO_2, H_2O, and H_2S is important to upgrade biogas to 90% or more CH_4 content, so that it can be used as transportation fuel or be used in the natural gas grid. Untreated biogas (dried and desulfurized) has low heating value due to impurities; it is used in boilers, dryers, and kilns, when equipment is modified to compensate for the low heating value and impurities. It is also used to generate electricity. Untreated biogas is currently used in industries such as auto manufacturing, chemical production, food processing, and pharmaceuticals (Figure 3.5)[73].

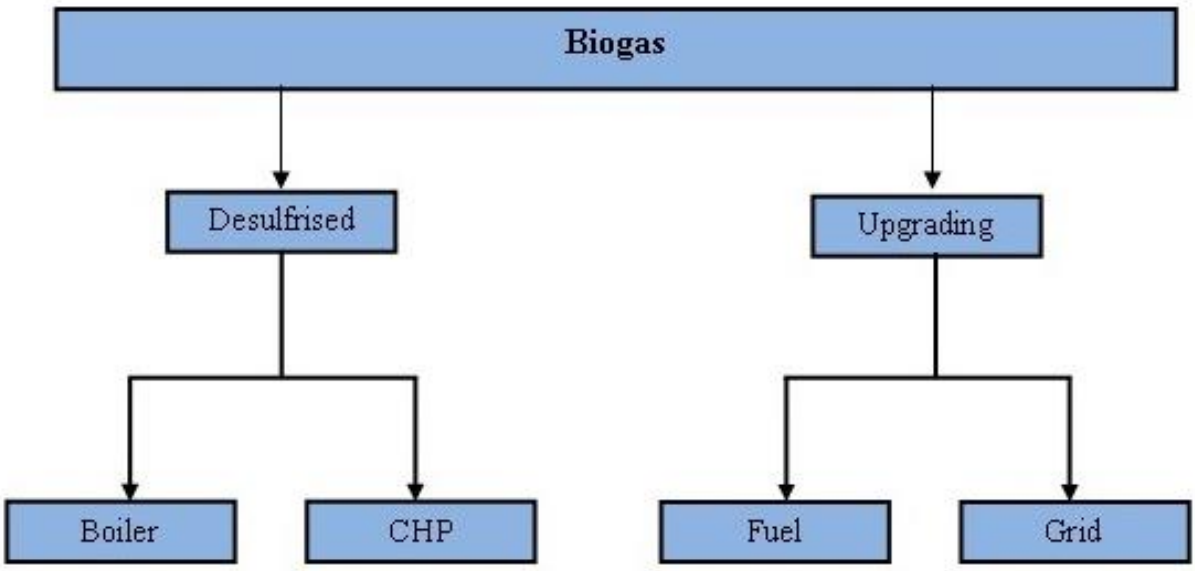

Figure. 3.5: *Potential different uses of biogas by end-user.*

3.6 Conclusion

Biogas is a renewable source of energy that can satisfy the needs of many Long Islanders, while offsetting the use of non-renewable resources such as natural gas, coal, oil. This can reduce local air pollution generated by conventional fossil fuels. By capturing biogas from landfills, release of CH_4 into the atmosphere can be prevented, helping to address climate change concerns since CH_4 is about 20 times more potent a greenhouse gas than CO_2. In addition, utilization of locally available biomass for production of biogas has the potential to reduce waste management costs, reduce waste odors, and create local jobs and revenues, and generate system cost savings, including costs for complying with state and federal waste disposal regulations. The co-products of the digesters can be used as a compost product. Green credits can be potentially earned, if legislation regulating CO_2 is enacted.

Various federal and state financial incentives are available to support biogas as a substitute for natural gas. These incentives include personal, corporate, sales, and property tax credits. A number of rebates, grants, loans, industrial support, and performance based incentives are also available.

Biogas potential and feasibility are usually assessed on national platforms. However, biogas feedstocks are localized and transportation of these feedstocks over long distances usually result in much higher costs, suggesting these resources will need to be exploited locally. Therefore, it is logical that accurate assessments of biogas potentials need to be constructed for local situations. This study closely examined the potential for one area, Long Island, to produce biogas from a variety of feedstocks from a particular set of generators. Similar studies conducted elsewhere will identify different amounts of waste products with different degrees of availability. However, the set of wastes (landfill gas, sewage sludge, yard waste, MSW, and agricultural wastes

including livestock manure) are likely to be the same across the U.S. and most of the world and, the procedures and estimation processes used here to quantify biogas potentials are likely to transfer well, giving this study general applicability beyond the specific results reported here.

There still exists a gap between technical and achievable feasibility. As with any new development, social, political, and economic barriers may impede the exploitation of biogas. The manner in which the gas is utilized can also affect the feasibility of such projects; for instance, the use of untreated biogas for electricity generation provides less revenues compared to upgrading biogas for automotive fuel or direct grid injection. Selection of end users depends on local conditions which need to be included in any careful feasibility assessment.

Chapter 4: Brookhaven Landfill

The gas collection data from the previous five years in Cells 5-6 at Brookhaven landfill on Long Island was examined. Biogas modeling using US EPA's Landfill Gas Emissions Model was utilized to forecast gas generation and recovery based on past and future C&D disposal in the landfill.

4.1 Site Description

Figure 4.1: *Arial view of the Brookhaven Landfill: Blue-cell 1, Yellow-cell 2, Green-cell 3, Pink-cell 4, Black-cell 5, and Red-cell 6.*

The Brookhaven Landfill is the largest active landfill on Long Island, NY. The landfill covers approximately 150 acres in the Town of Brookhaven, NY. The landfill does not accept any MSW but does process: ash from WWTP sludge, ash from MSW Energy Recovery System, C&D,

sewage treatment plant sludge, downtime waste, and bypass waste. In 2012, the landfill processed nearly 3,600 tons day^{-1}; about 30% is incinerator ash form LI WTE plants, 10% is locally-generated material, and 60% is C&D, much of which is thought to be from New York City.

The landfill is divided into two sections, of which only one section is operational. Cell 1-4 are located in section one and have been closed and 100% capped with approved final cover system since 1997. Section one is 100 acres in size and has approximately 10 million tons of MSW in place. Section two (100 acres) began operations in 1995 (Cells 5-6). While Cell 5 no longer accepts waste and currently being capped, Cell 6 continues to accept waste. Only 20% of section two is capped and covered. Approximately 11.5 million tons of waste was in place. A total of 50 vertical gas recovery wells have been drilled into Cells 1-5, while over 100 horizontal wells were drilled into Cells 5-6.

Currently, the Brookhaven facility is the only active landfill on LI generating electricity via biogas. The LGRF at Brookhaven, which originally cost $7.2 million, was established in 1983. It is currently managed by Wehran Energy Corporation. The landfill was closed to MSW in 1995 but the 10 million ton MSW landfill has generated over 350,000 MW-hrs of electricity since operation. The Long Island Power Authority pays 8.5 cents per kW-hr for power delivered to its grid. Currently the gas is collected from all six cells. The annual operation and maintenance cost for the 2012 fiscal year was approximately $350,000. In 2012, Brookhaven recovered over 17 million m^3 of gas and generated 1,800 MW-hrs of electricity. The electricity is generated via one internal combustion engine, which consumed over 1.4 million m^3 of biogas. The facility also operates two flares - one enclosed and one open - which flare the remaining biogas. The CH_4 percentage in the gas used for electricity generation was 53%, while the flared gas contained 33%. Declining levels of CH_4 have forced the facility to look for alternative ways to stay operational.

Landfill gas collection data was provided by Town reports to the New York State Department of Environmental Conservation (NYS DEC). US EPA model LandGEM was used to calculate landfill CH_4 emissions. LandGEM model is a free software which can be obtained from the EPA website. The model follows a first-order decomposition rate equation to estimate annual emissions over a time period:

$$Q_{CH_4} = \sum_{i=1}^{n} \sum_{j=0.1}^{1} kL_o \left(\frac{M_i}{10}\right) e^{-kt_{ij}}$$

where

Q_{CH4} = annual CH_4 generation in the year of the calculation (m^3 $year^{-1}$)

i = increment by 1 year

n = (year of the calculation) – (initial year of waste acceptance)

j = increment by 0.1 year

k = CH_4 generation rate ($year^{-1}$)

L_o = potential CH_4 generation capacity (m^3 Mg^{-1})

M_i = mass of waste accepted in i^{th} year (Mg)

t_{ij} = age of the j^{th} section of waste mass M_i accepted in the i^{th} year

The LandGEM provides CH_4 generation constant and potential for CAA (Clean Air Act) standards though these values were not used as they are based on decomposition of landfilled waste in MSW landfills. The k. L_o, and M_i values were calculated based the data provided from the Brookhaven landfill.

4.2 Results

The results from landfill gas collection in Cell 5-6 are presented in Figures 4.2-8. Note the average CH_4 concentration in Cell 5-6 was 40% lower then what was normally produced from Cells 1-4 which has MSW.

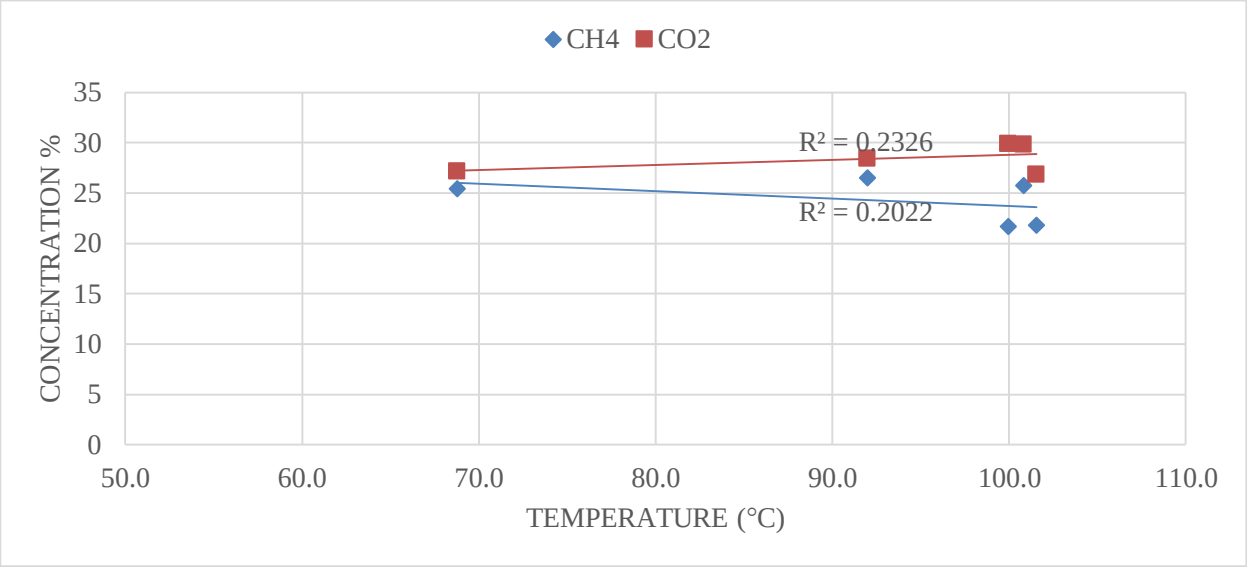

Figure 4.2: *Annual (2008-20012) change in CO_2 and CH_4 concentration as a function of landfill temperature in cells 5-6. R^2<0.24 is an indicator of a weak relationship between overall landfill temperature to CH_4 or CO_2 concentration.*

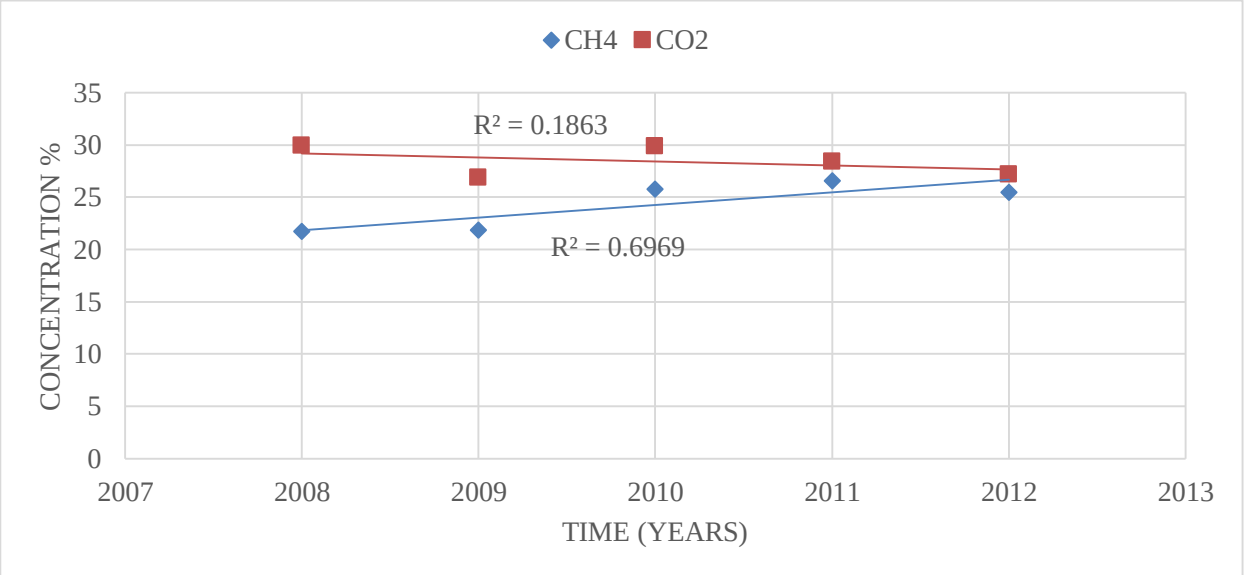

Figure 4.3: *Increase in CH_4 concentration was noted from 2008-2012 as new gas collection wells were drilled and the aging C&D started to decompose. Meanwhile, the CO_2 shows a slight decrease in concentration.*

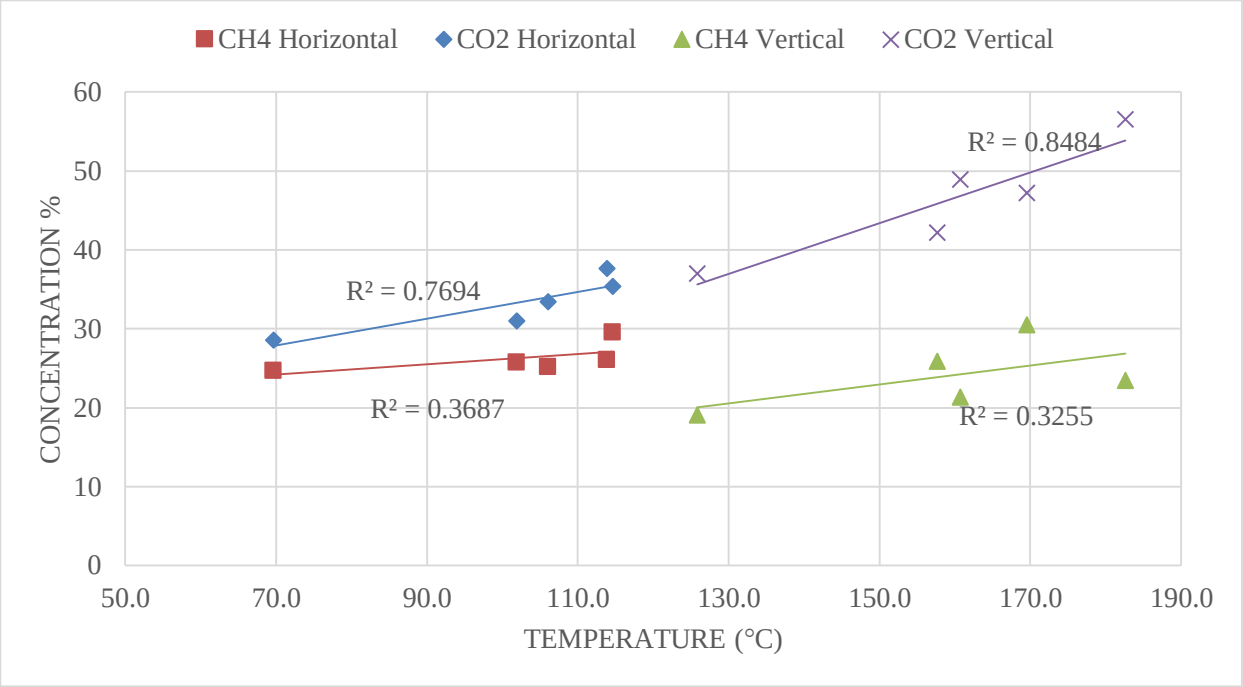

Figure 4.4: *Closer look at the gas concentration of Cell 5 in the horizontal and vertical wells was much different than the overall landfill. The average temperature in the vertical wells was 50 °C higher than in horizontal wells. This large temperature gradient may be due to the higher concentration in CO_2 at the base of the landfill. While overall CH_4 concentration was the same in both vertical and horizontal wells. A strong correlation between temperature and CO_2 was also established ($R^2 > 0.76$).*

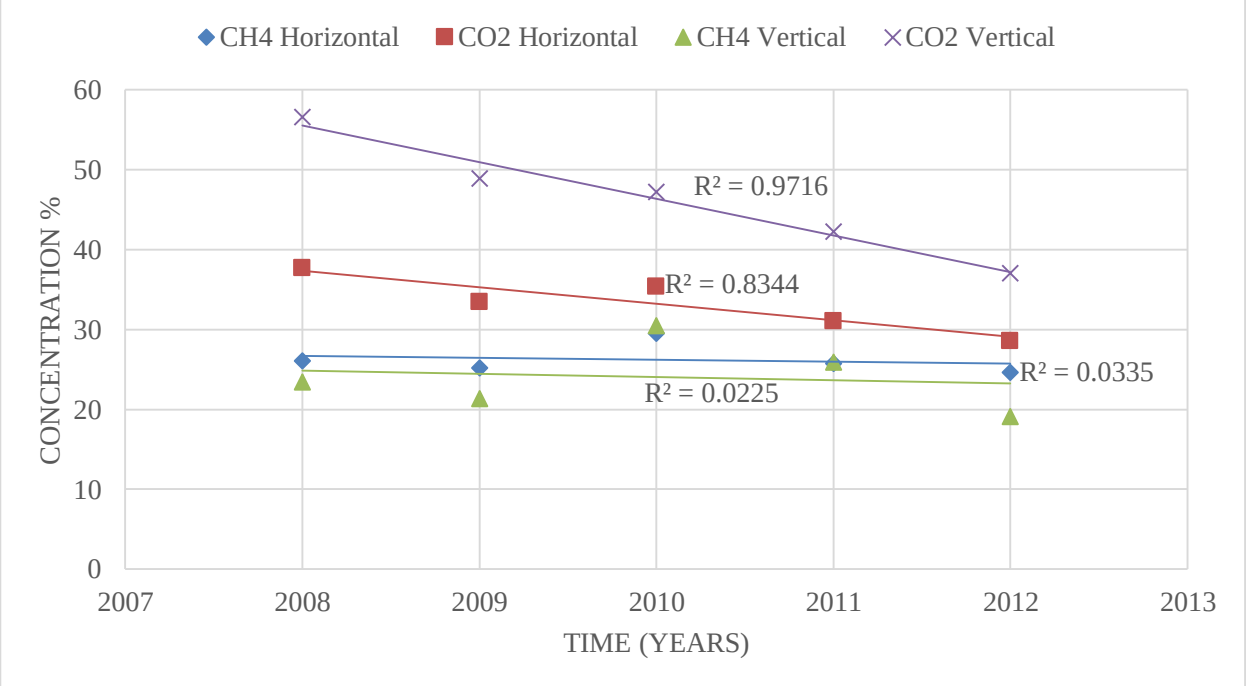

Figure 4.5: *From year to year the CO_2 concentration decreased in both the horizontal and vertical wells, while the CH_4 concentration held steady.*

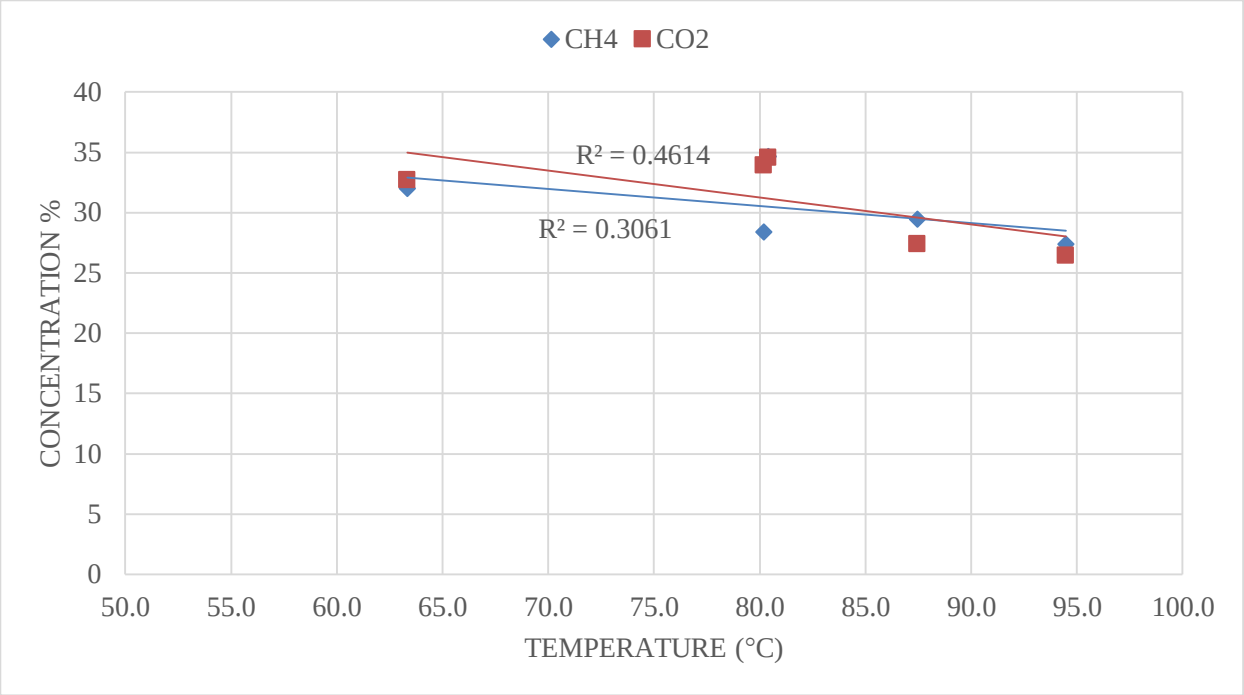

Figure 4.6: *Concentration of CH_2 and CO_2 in Cell 6 was close to 1:1 ratio. Note that Cell 6 only had horizontal wells present. The average temperature was 20 °C cooler in Cell 6. A slight negative slope in the trend line was shown in both CH_4 and CO_2 concentration.*

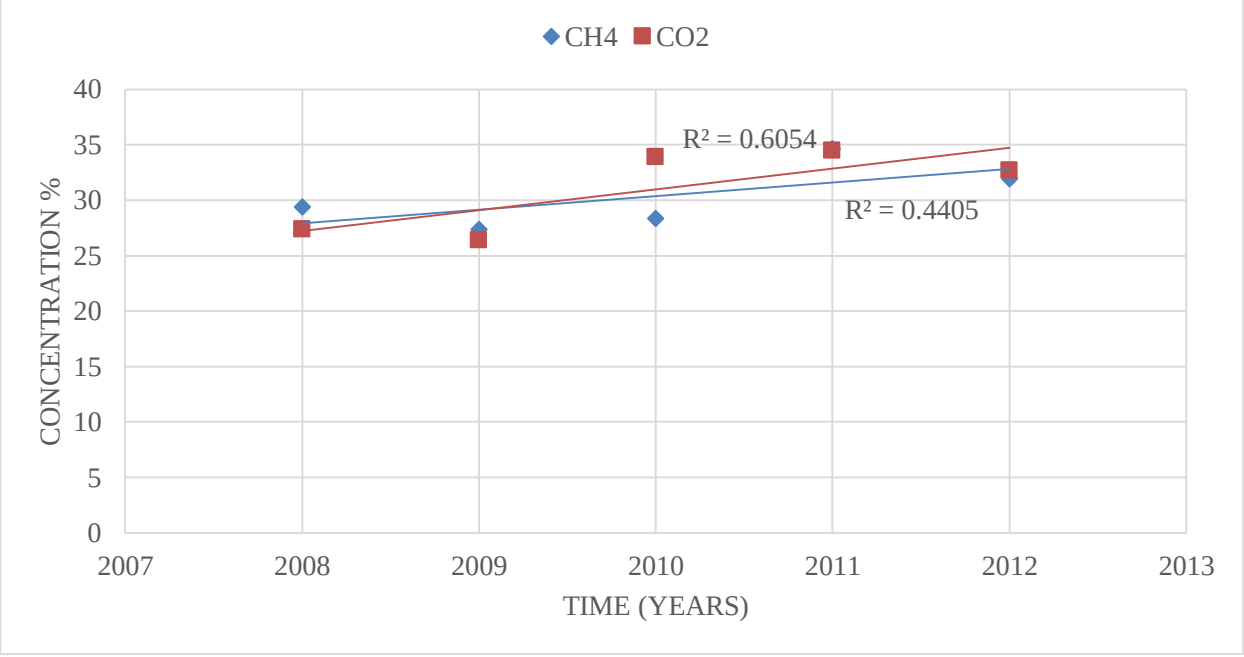

Figure 4.7: *Cell 6 showed a steady increase in both CH_4 and CO_2 concentration from 2008-2012. The concentration of CH_4 in Cell 6 was 13% higher than in Cell 5, while the CO_2 content was equal to that of Cell 5***.**

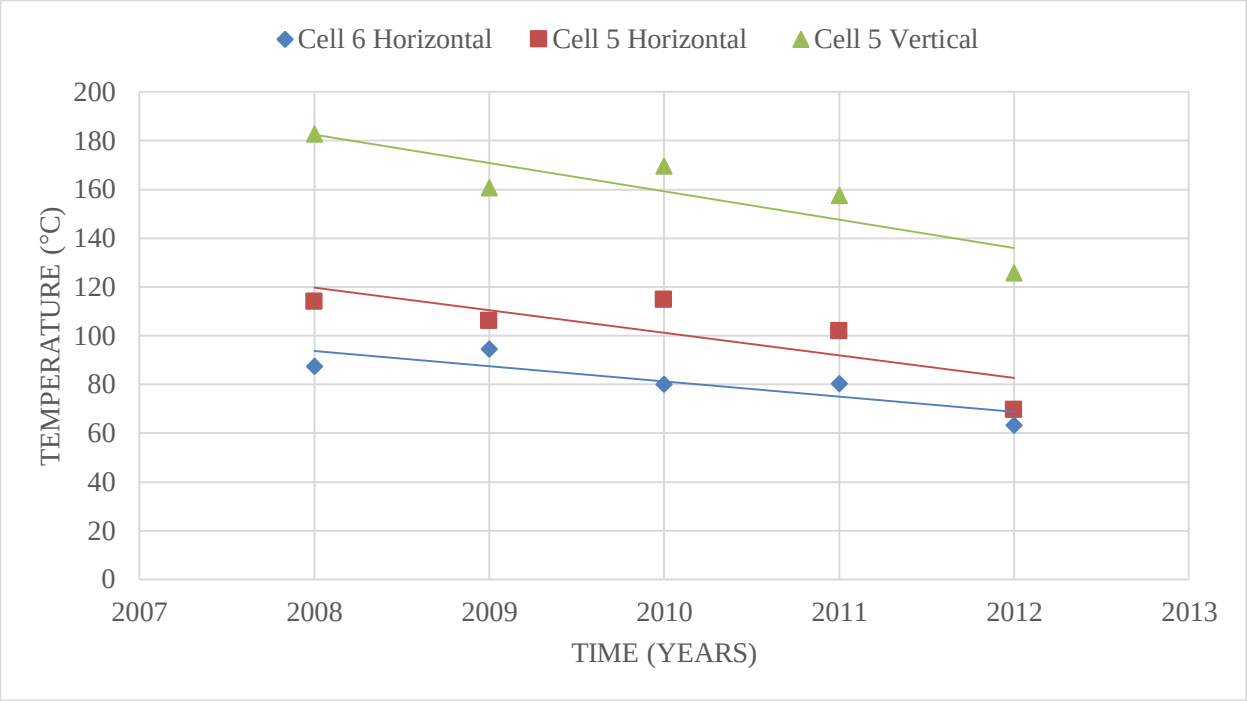

Figure 4.8: *Overall decrease in landfill temperature in Cell 5-6 was noted from 2008-2012.*

Chapter 5: Catalyst Synthesis

5.1 Introduction

Nanotechnology has become increasingly applied in many different fields. The use of iron oxides in particular has drawn a lot of attention. These particles have number of different applications in chemical industries, biotechnology, medicine, and electromagnetic devices. Present methods to synthesize iron oxide nanoparticles consist of thermal decomposition, co-precipitation, microemulsion, hydrothermal synthesis, and sonochemical synthesis[97, 98].

5.1.1 Thermal Decomposition

Thermal decomposition of iron precursors in hot surfactant solution has been used to develop iron oxide nanoparticles. Decomposition of $FeCup_3$ (Cup = nitrosophenylydroxylamine)[99], $FeAcac_3$ (Acac = acetylacetonate)[100], and $Fe(CO)_5$[101] has been shown to produced monodispersed nanoparticles. Formation of nanoparticles after decomposition is followed by oxidation, which usually requires relatively higher temperatures and a complicated procedure. The biggest disadvantage of this method is the resulting nanoparticles are generally only soluble in nonpolar solvent[97].

5.1.2 Co-Precipitation

The co-precipitation method is the most often used method for obtaining iron oxide nanoparticles. This method consists of mixing ferric and ferrous ions in a 1:2 molar ratio in highly basic solution. The size and shape of the nanoparticles depend on the reaction temperature, the pH value, the ferric and ferrous ions ratio, the type of salts used, and the ionic strength of the media. This process has been recognized for its industrial importance because it can be scaled up, and its reproducibility[97, 98, 102]. Unfortunately, in most cases the generated particles have a wide particle size distribution. This can affect the magnetic properties of the particles as reported by

Kang[103]. Additionally, the aqueous solution synthesis requires high pH values for the reaction to take place. This leads to the generation of a highly basic aqueous solution that requires proper waste management.

5.1.3 Microemulsion

The "water in oil" microemulsion technique has been widely used to synthesize uniform size nanoparticles of various kinds. A microemulsion is a thermodynamically stable isotropic dispersion of H_2O, oil, and a surfactant. The surfactant molecules lower the interfacial tension of the water and oil, resulting in the formation of a transparent solution. Each H_2O nanodroplet present in the bulk oil phase serves as a nanoreactor for the synthesis of nanoparticles of different kind of materials. The size of the H_2O pool greatly influences the size of the nanoparticles[104]. This way the size of the nanoparticles can be controlled. However, despite the presence of surfactants, the aggregation of the produced nanoparticles usually needs several washing processes and further stabilization treatments, making the process very complicated[97].

5.1.4 Hydrothermal Synthesis

Hydrothermal synthesis includes various wet chemical technologies for crystallizing substances at high temperatures and vapor pressures in aqueous solutions. This synthesis is performed in H_2O at elevated temperatures, where the dielectric constants of H_2O approach those of polar organic reagents. This will allow the water and surfactants to mix into a single phase. This single phase solution works as reaction medium for both hydrothermal synthesis and surface modification[105]. This technique has also been used to grow dislocation free single crystal particles, and products formed in this process could have a better crystallinity than when formed through other processes. Hydrothermal synthesis results in highly crystalline iron oxide nanoparticles[97, 98].

5.1.5 Sonochemical Synthesis

The use of acoustics, initially developed by Suslick[106, 107], are now being used extensively to develop nanoparticles. Sonolysis techniques have been extensively used to generate novel materials. Sonochemical synthesis uses ultrasound in aqueous solutions to initialize chemical reactions. The chemical effects of ultrasound arise from acoustic cavitations, that is, the formation, growth, and implosive collapse of bubbles in liquid. The implosive collapse of the bubble generates a localized hotspot through adiabatic compression or shock wave formation within the gas phase of the collapsing bubble. The conditions formed in these hotspots have been measured at temperatures of 5200 K, pressures of 1800 atm, and cooling rates in excess of 10^{10} Ks^{-1}. The calculated lifetime of these bubbles is <2μs. These conditions are important in forming nanoparticles.

One of advantage of sonochemistry is that it can be applied for the synthesis of amorphous metal oxides which are nanometer in size without the addition of glass formers, as done in cold quenching of bulk metals. Additionally, researchers have been able to control the shapes of the products, such as nanotubes, nanorodes, and hollow spheres. Sonochemistry has been used to prepare various kinds of amorphous magnetic nanostructures. Finally, the formation of nanoparticles at high conversion rates (>70%) in a limited amount of time has been a major draw to sonochemistry.

Application of this method has been successfully demonstrated to form nanoparticles[108-111]. Vijayakumar et al.[112] studied the formation of Fe_3O_4 powder via sonochemical synthesis. The samples were prepared by sonication of iron(II)acetate in water under an argon atmosphere. The prepared nanometer-size Fe_3O_4 powder had a particle size of 10 nm as measured under TEM. The Fe_3O_4 particles were superparamagnetic and magnetization at room temperature was very low

(<1.25 emu g^{-1}). Kenneth et al.[113] synthesized nanostructured Fe, Co, and Fe-Co alloy materials by using various concentrations of $Fe(CO)_5$ and $Co(CO)_3(NO)$ in decane at 0°C for 3 hours under argon. The resulting nano-catalyst exhibited higher catalytic activities in comparison to commercially available catalyst. The catalyst had high surface area of 188 m^2g^{-1} and was amorphous in nature. Synthesis of mesoporous iron oxides was conducted by Srivastava and coworkers. Iron (III) ethoxide was used as an inorganic precursor and CTAB as an organic structure directing agent. The surface area of the nanoparticles was found to be 274 m^2g^{-1}.

Iron nitride nanoparticles were prepared by Koltypin at el.[114] using two different methods. In the first method, a mixture of $Fe(CO)_5$ and decane was sonicated in a gaseous mixture of NH_3 and H_2 (3.5:1 mole ratio) at 0 °C. In the second method, amorphous iron was sonicated at 400 °C under NH_3 and H_2 (3.5:1 mole ratio) at 400 °C. Decomposition of $Fe(CO)_5$ formed $Fe_{2-3}N$ with impurities of Fe_3O_4. The second method resulted in pure agglomerated Fe_4N of 30-50 nm diameter with a surface area of 40.6 m^2g^{-1}. Iron oxide nanoparticles coated with different surfactants were prepared by Shafi and coworkers[115]. Sonochemical decomposition of $Fe(CO)_5$ was carried out in the presences of undeconoate, dodecyle sulfonate and octyl phosphonate. Nanoparticles of 5-26 nm in diameter were obtained. The binding of the surfactants was confirmed by FTIR measurements. Phosphonate coated samples showed much more unique behavior compared to the other samples. It was concluded that the extra negative charge of the phosphonate made it more superferromagnetic.

Decomposition kinetics and product characterization of nano iron particles produced by sonolysis were carried out by Mahajan et al.[116] The iron nanoparticles were produced by decomposition $Fe(CO)_5$ at 302-327 K in hexadecane. The decomposition data showed a first-order reaction with a correlation coefficient (R^2>0.95) for all runs. TEM micrographs showed particle

diameter of less than 10 nm in size. Meanwhile, XRD spectra confirmed the formation of amorphous Fe particles.

In this study we synthesized iron oxide nanoparticles via decomposition of $Fe(CO)_5$ in hexadecane and n-decane solvents using sonochemical synthesis. Kinetics and product characterization of the synthesized produce were carried out by SEM, XRD, FTIR and BET. Effects of sonication time on particle development was extensively studied.

5.2 Experiment

5.2.1 Materials

Hexadecane (99%, anhydrous), hexane (98.5%, ACS reagent grade), pentacarbonyl iron ($Fe(CO)_5$) (99.5% purity) and n-decane (99% purity) were purchased from Sigma Aldrich Chemical Co. Argon gas was obtained from Scott specialty gases. Due to the toxicity and flammability of $Fe(CO)_5$, all manipulations were carried out in a fume hood with appropriate precautions.

5.2.2 Sonolysis unit and Experimental Setup

All experiments were carried out using an ultrasonic liquid processor Sonicator 3000 from MIXONIX, Inc. with a variable power output of up to 100 W at a fixed frequency of 80 kHz. The unit was fitted with 12.7-cm.-long half wave extender tip with a probe tip of 1.27 cm in diameter. The unit allowed precise control of power output, processing time, and pulsar cycle for cyclic intermittent operation to avoid heat buildup during synthesis.

The setup for the sonolysis experiment was as follows: (1) the reaction vessel, purchased from Ace Glass, Inc., was a borosilicate glass four-neck flask with walls tapered inward toward the bottom that allowed maximum solution in the middle of the flask for adequate immersion of

the sonication probe; (2) a series of O-rings and standard greased ground-glass joints ensured tight seals to maintain rigorous exclusion of air or gas leakage from the flask during sonication; (3) any gas evolved during sonication was collected and analyzed; and, (4) the flask was immersed in a constant-temperature bath.

5.2.3 Synthesis of Fe Nanoparticles

Prior to sonication, the solvent was thoroughly degassed with argon followed by the addition of $Fe(CO)_5$. In a typical run of the Fe system, a degassed yellow homogeneous solution of $Fe(CO)_5$ (0.015 mol) in 50 ml of solvent was sonicated at 100% intensity and 80% pulsed cycle settings. Sonication of the solution resulted in gas formation which was collected and analyzed. Within minutes of starting the sonication the yellow solution evolved into black slurry. After sonication the product was centrifuged and the upper solvent layer was decanted to separate the product. The remaining black solid was washed three times with hexane to remove any residual solvent. The resulting black solid was dried in an oven over night at 200 °C.

5.2.4 Analysis

The gases collected during sonication were analyzed using a Gow-Mac model 580 gas chromatograph fitted with molecular sieve column (22.8 cm. x 0.3 cm) with He as the carrier gas. The solid samples were characterized using number of different techniques. The infrared measurements were done on a Parkin-Elmer Fourier FTIR equipped with an UATR module. A small amount of powder sample was directly put onto the UATR lens for analysis. The TEM images were recorded on a FEI Biotwin scope (120 KV model) to determine the particle size. The SEM images were recorded on L.E.O 1550 (20 KV model). EDAX spectra were recorded along with SEM images. Powder XRD measurements were conducted for phase identification of the solid samples. The sample was annealed at 200°C for five hours before XRD measurements. BET

surface area calculations were carried out using a Micromeritics TriStar 3000 surface analyzer at -196 °C with N_2 adsorption.

5.3 Results and discussion

The sonochemical decomposition of $Fe(CO)_5$ has been shown to yield Fe nanoparticles. The stoichiometry of 5 mol CO per mol of $Fe(CO)_5$ determines the percent Fe yield. The iron oxide yield varied from 40-90%. The yield was based on the final dried product obtained and it did not account for any losses due to vaporizing or an incomplete $Fe(CO)_5$ decomposition. The reactions were allowed to progress between 2-8 hours. The sonication was stopped once CO gas evolution rate slowed. The gas chromatography analysis showed the CO concentration was <99%. Although the constant temperature bath was set at 23 °C, the measured temperatures inside the flask were 10-20 °C higher than the bath temperature.

The decomposition of $Fe(CO)_5$ in n-decane led to the formation of red-orange colored product. Four separate samples were synthesized with run times of two (ND-2), three (ND-3), four (ND-4) and eight (ND-8) hours. The SEM micrograph (with corresponding EXAD spectra) of the final product confirmed the formation of iron oxide in each case. The duration of the sonication plays an important role in the physical size of the particles, as determined by SEM. Longer periods of sonication resulted in particles which were smaller in size. A sonication time of eight hours resulted in particles with diameters of <10nm in size, which is much smaller than those created by thermal decomposition of $Fe(CO)_5$[116]. A sonication time of two hours resulted in particles with a diameter 100-200 nm in size. Individual particles are difficult to view under the SEM (see Figure 5.1). Particles in the ND-8, ND-4, and ND-3 samples were amalgamated together resulting in cloudy images. These amalgamated particles are spherical in size as expected. Closer examination of the samples under the TEM was required to calculate the precise size of the

amalgamated particles. Meanwhile, micrographs of sample ND-2 clearly showed large spherical shaped particles.

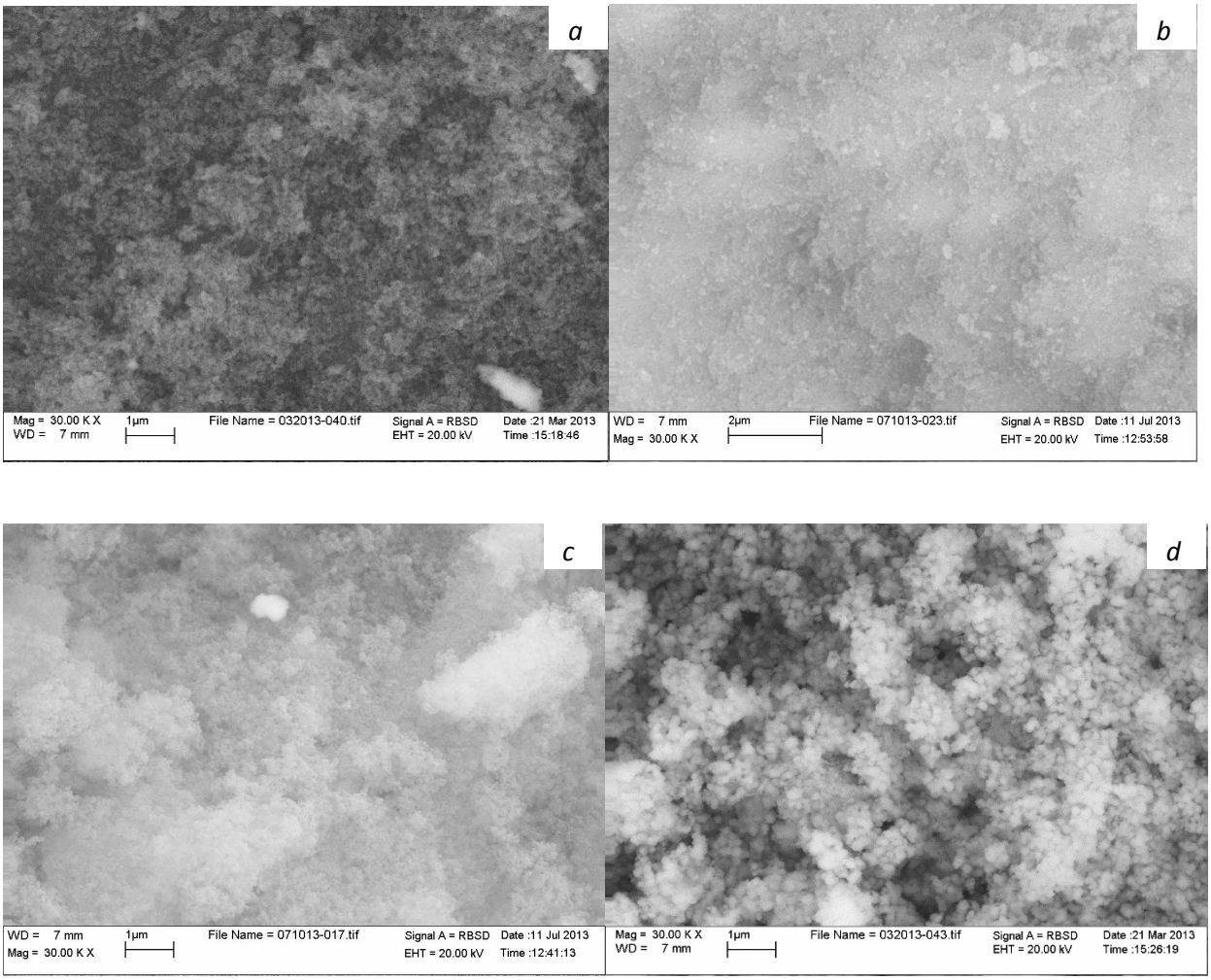

Figure 5.1: *SEM micrographs and the corresponding EDAX spectra of sample (a) ND-8, (b) ND-4, (c) ND-3 and (d) ND-2.*

Figure 5.2 shows the XRD pattern of the product at room temperature. The XRD spectra of sample ND-2 matched well with that of Fe_3O_4 (magnetite) spectra. Seven main peaks at 2θ equal to 30°, 35°, 37°, 43°, 53°, 57° and 62° for Fe_3O_4 were observed along with small beta peaks. The peaks in the XRD spectra indicated the product was a crystalline solid unlike the product produced in other studies[106, 116]. Comparing the XRD spectra of ND-2 and ND-8 highlighted the

effects of particle size on XRD spectra. Smaller particles resulted in broader peaks as shown by Suslick et al[106]. There was an increase in the signal observed at $2\theta = 35°$, which did not resolve as a peak for the ND-8 sample.

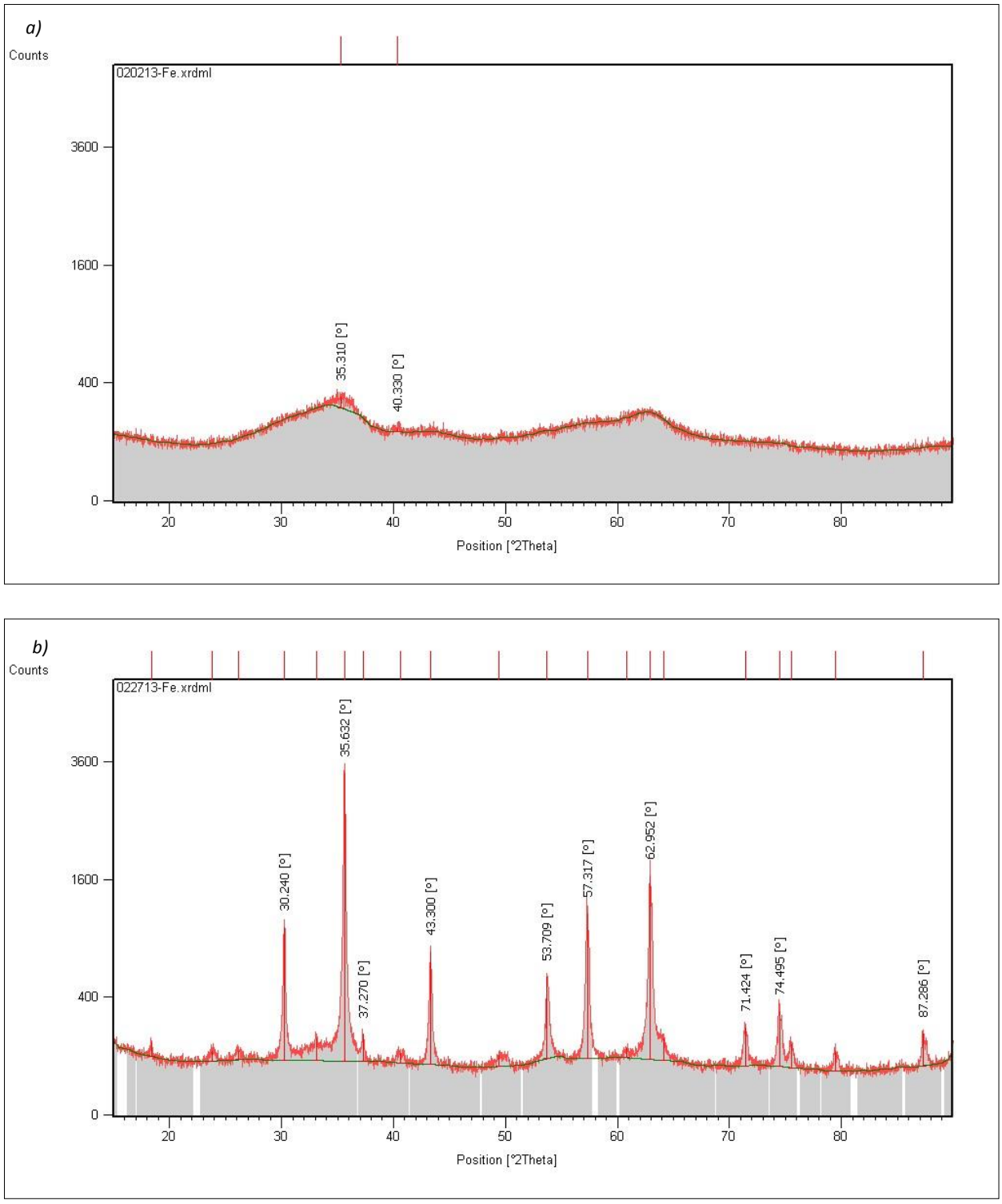

Figure 5.2: *XRD spectra of sample (a) ND-8 and (b) ND-2.*

A similar analysis of iron oxide particles produced from the decomposition of $Fe(CO)_5$ in hexadecane was conducted. Samples were sonicated for two (HD-2), three (HD-3), four (HD-4) and eight (HD-8) hours. The dried products were brown in appearance, unlike samples produced using n-decane. Sample HD-8 had particles of diameters <20nm in size, making them slightly larger compared to ND-8, but the samples developed under short sonication times were larger in size. Six peaks at 2θ equal to 30°, 35°, 43°, 53°, 57°, 62° were recorded on the XRD spectra of HD-2, HD-3, HD-4 and HD-8 (see Figure 5.4). The XRD spectra of all the samples closely matched with the spectra of α-Fe_2O_3 (hematite); however, peaks resolved for HD-8 are slightly broader in comparison to others, which was attributed to the particle size of the samples. The use of n-decane may have allowed for the formation of smaller particles compared to hexadecane over the same period of time. Peaks in the XRD spectra of HD-2 were of a lower intensity compared to ND-2, which may have been due to the decreased crystallinity of the sample. Sample HD-8 had an XRD spectra much sharper in contrast to the ND-8 sample, indicating the formation of crystalline product with a larger particle size.

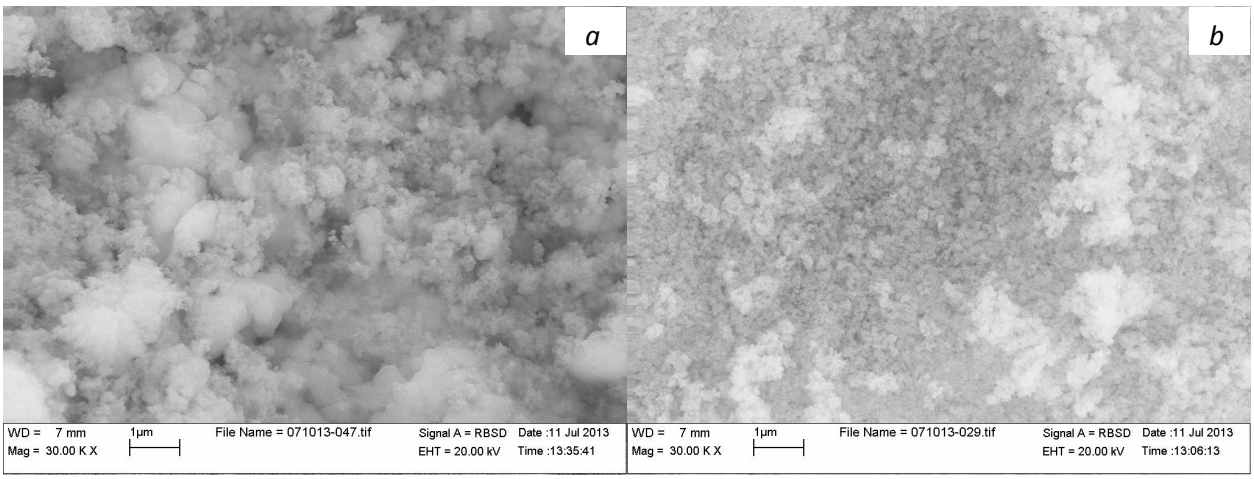

Figure 5.3: *SEM micrographs of (a) HD-8 and (b) HD-2.*

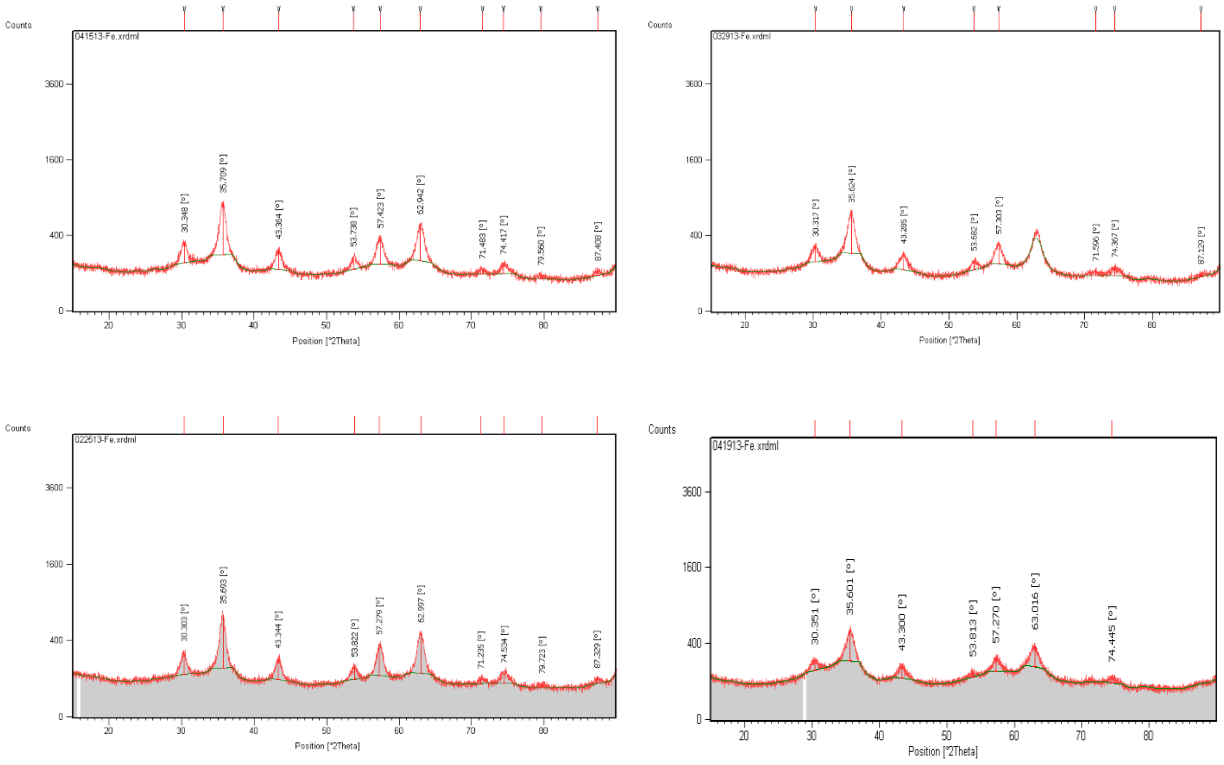

Figure 5.4: *XRD spectra of sample of (left to right) HD-2, HD-3, HD-4, and HD-8.*

5.3.1 Decomposition Kinetics

First order plots of $Fe(CO)_5$ decomposition in hexadecane and n-decane are shown in Figure 5.5. The plot shows the change in $Fe(CO)_5$ concentration in log scale versus time from which the first-order rate constant (k) was calculated at 303 K. Rate constant of 2.6 x 10^{-3} m^{-1} (HD-8) and 2.3 x 10^{-3} m^{-1} (HD-3) were calculated. Doubling the concentration of $Fe(CO)_5$ in sample HD-3(a) had no effect on the reaction kinetics, confirming the validity of the first-order analysis. However, sample ND-3 showed k=6.0 x 10^{-4} m^{-1} which is a magnitude smaller than any sample produced in hexadecane. This indicated the reaction proceeded at a slower rate in n-decane compared to hexadecane. Smaller k values pointed to the lower product yield of iron oxide in n-decane compared to hexadecane. A linear regression analysis showed a correlation coefficient of $R^2 > 0.93$ for each run.

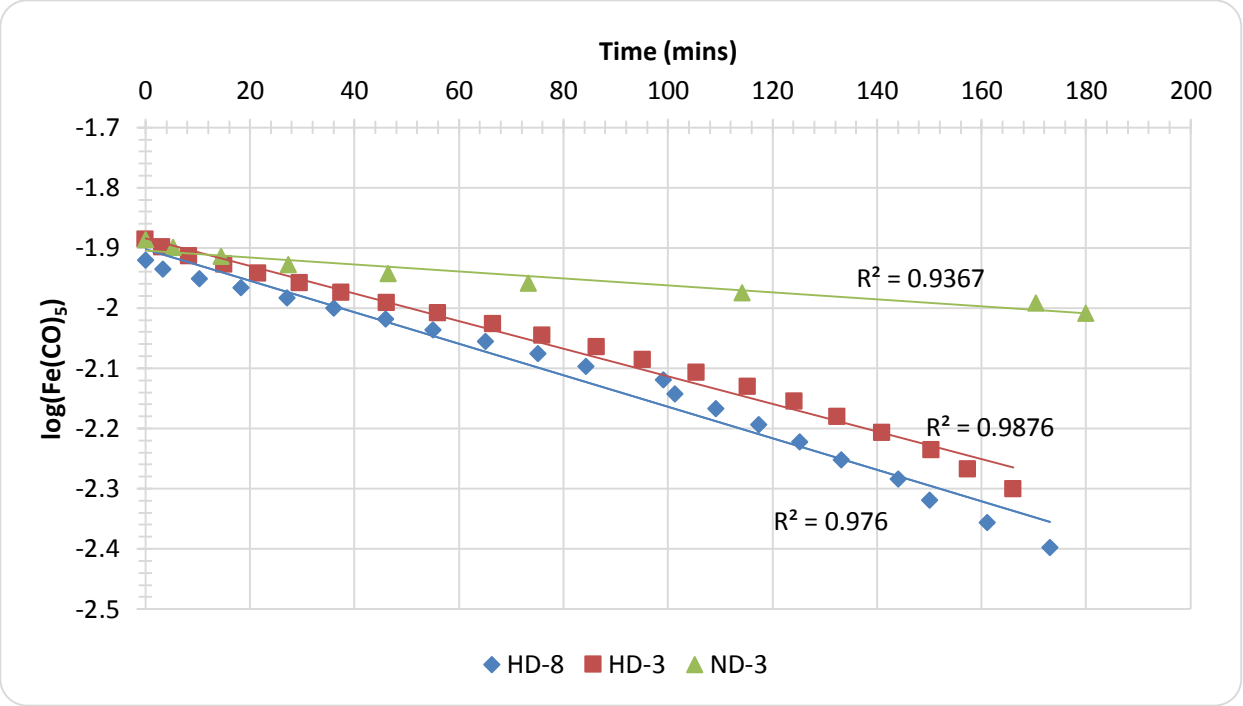

Figure 5.5: *First order rate reaction as calculated at 303 K from decomposition of $Fe(CO)_5$ in hexadecane and n-decane. The reaction processes were much quicker in hexadecane compared to n-decane.*

5.3.2 Surface Area

Surface area measurements of the samples showed wide ranges of calculated area. Table 5.1 shows the differences in surface area as measured using BET and Langmuir equations. A strong correlation between the sonication time and the development of surface area was drawn from the data. Sonication time of less than three hours led to larger particles (100-200 nm) regardless of the solvent used, while a sonication time ≥4 hours led to smaller particle sizes thus higher measured surface area. Longer period of sonication meant longer reaction time thus smaller particles being produced. This process of increasing sonication time to obtain smaller particles was limited by the solvent being used. As seen from Table 5.1 the difference in surface area between ND-4 and ND-8 was 49 m^2g^{-1}, whereas the surface area of HD-4 and HD-8 was only 6 m^2g^{-1}. Use of n-decane results in iron oxide particles which had higher surface area. The measured

surface area of samples synthesized in n-decane were approximately twice as much when compared to hexadecane. A linear regression study showed a correlation coefficient of $R^2 \geq 0.85$ for ND samples and $R^2 \geq 0.59$ for HD samples.

The effect of $Fe(CO)_5$ concentration on surface area development was studied by doubling the amount of $Fe(CO)_5$ and sonicating for three hours (sample HD-3(b)). Surprisingly, sample HD-3(b) had a 22% increase in surface area compared to HD-3. This meant the particle size of the product decreased in order for the surface area to increase. Higher concentrations of $Fe(CO)_5$ equated to higher concentrations of iron particles produced in the solvent. The resulting higher concentration of iron particles amalgamate into larger size particles than before. Due to the nature of sonochemical synthesis, larger amalgamated iron particles lead to more violent and frequent collisions between the particles. Consequently, this may have helped break the particles down further into smaller sizes, thus increasing the overall surface area.

Sample	***Sonication Time (hrs):***	***BET (m^2g^{-1}):***	***Langmuir (m^2g^{-1}):***
ND-8	8	194.30	269.60
ND-4	4	145.21	202.25
ND-3	3	70.26	97.46
ND-2	2	35.23	50.08
HD-8	8	76.50	106.10
HD-4	4	71.23	99.34
HD-3	3	53.71	74.40
HD-2	2	16.48	23.49
*HD-3(b)**	3	65.65	91.67

Table 5.1: *Surface area measurements as calculated by BET and Langmuir equations. *HD-3(b) sample had twice as much concentration of $Fe(CO)_5$ (0.032 mol).*

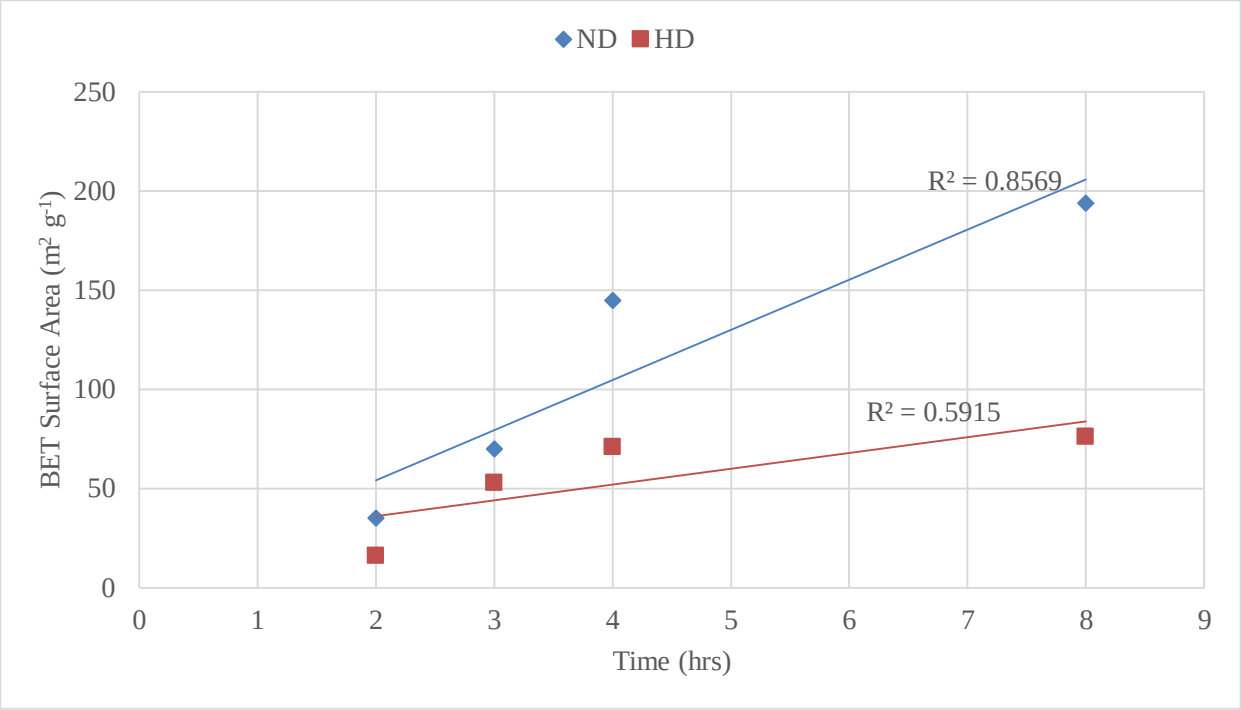

Figure 5.6: *Linear regression analysis of the surface area vs. sonication time.*

5.3.3 FTIR spectroscopy

Figure 5.7 illustrates the IR spectra of sample HD-2-8. All HD samples exhibited a broad IR band around 3370 cm^{-1}, which was associated with the surface H_2O molecules or to an envelope of hydrogen-bonded surface OH groups[117]. Sample HD-2 showed sharp peaks at 2923 and 2853 cm^{-1} due to residual hexadecane present in the sample. These two bands were attributed to C-H stretch mode. Strong IR bands around 630, 550 and 390 cm^{-1} were also present in HD-2, HD-3 and HD-4. Work by Vedonck et al.[118] and Cambier[119], showed the IR band at 634 cm^{-1} can be assigned to Fe-O stretching vibration. Bands at 550 and 390 cm^{-1} might have been assigned to the Fe-O bending mode of the tetrahedral and octrahedral sites respectively[120]. The positions of these two bands depend on the stoichiometry of the iron oxide.

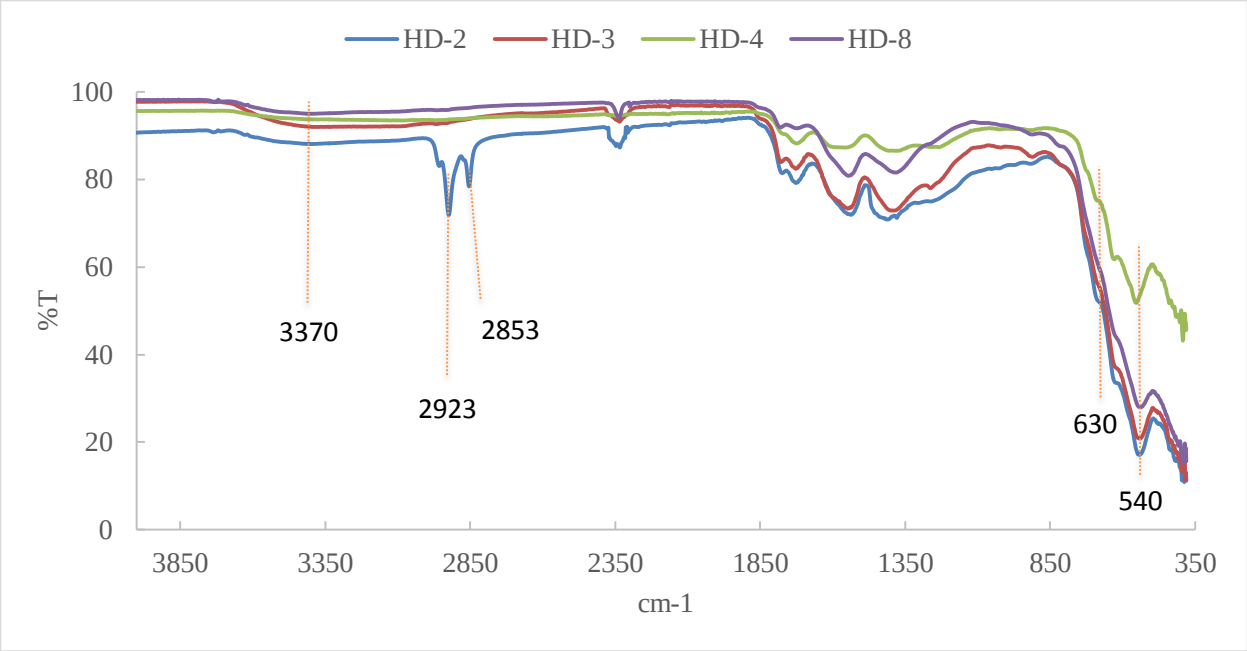

Figure 5.7: *FT-IR spectra of iron oxide samples formed in hexadecane.*

Samples ND-2-8 displayed a broad band at 3370 cm^{-1} assigned to H_2O molecules (see Figure 5.8). The sample ND-2 displayed strong peaks at 638, 535, and 390 cm^{-1}, while sample ND-4 showed a peak at 535 and 392 cm^{-1}. These peaks were assigned to stretching and bending mode of Fe-O. Sample ND-3 and ND-8 exhibited sharp bands at 394 and 392 cm^{-1} respectively. Bands around 390 cm^{-1} were assigned to the Fe-O bending mode of the octrahedral site. The sample ND-2 showed weak peaks at 2923 and 2853 cm^{-1} given to C-H stretching mode like its HD-2 counterpart.

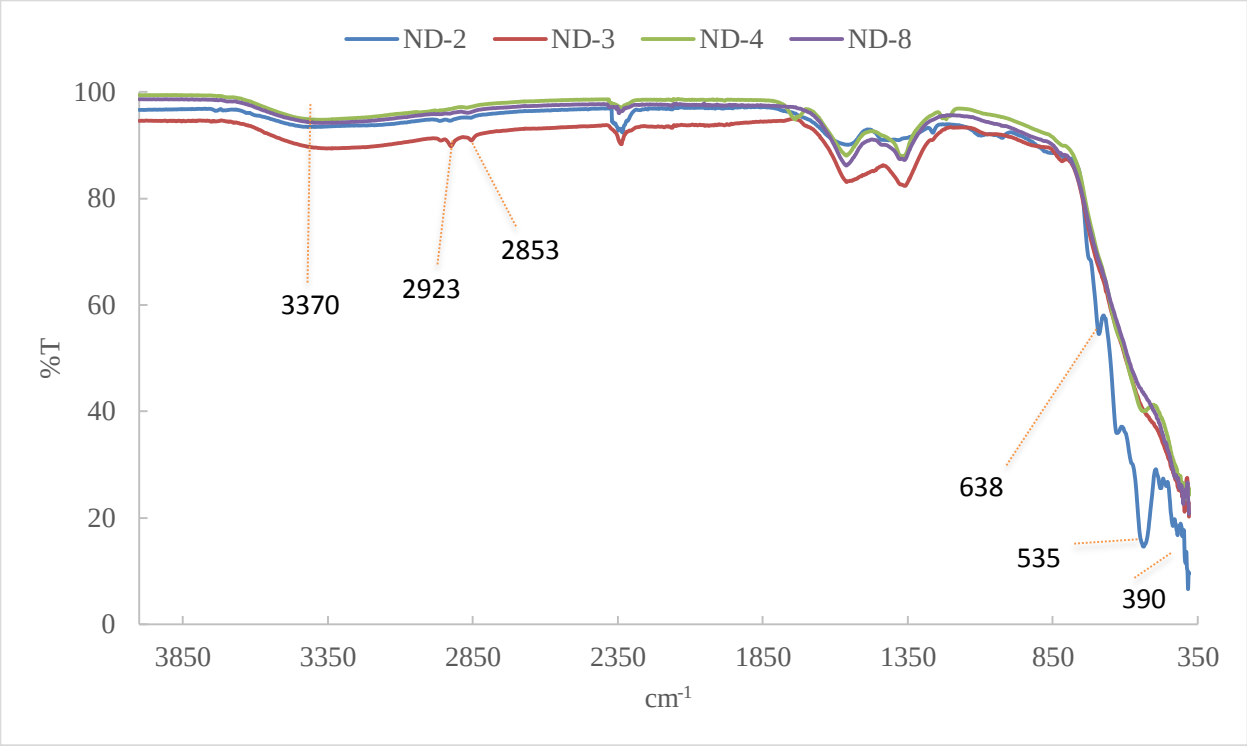

Figure 5.8: *FT-IR spectra of samples ND-2, ND-3, ND-4 and ND-8.*

5.4 Conclusion

Sonochemical synthesis of iron oxide from the decomposition of $Fe(CO)_5$ in hexadecane and n-decane was reported. The characterization of the powder product via XRD and FTIR confirmed the production of α-Fe_2O_3 hematite in all cases, except the ND-8 sample. No conclusive data were obtained to identify the iron oxide phase of ND-8 sample. A strong correlation between sonication time and particle size formation was established by the measurement of surface area. It should be noted that the solvent used in producing iron nanoparticles played an important role in particle size and surface area formation. Particles with surface area ranging from 195-34 m^2g^{-1} were produced when using n-decane, while surface areas ranging from 76-16 m^2g^{-1} were produced using hexadecane. Sonication time between 2-3 hours led to particles of 100-200 nm in diameter and 4-8 hours led to particles of <30 nm in diameter. Prolonged sonication time improved surface

area development. Increasing sonication time from 4 hours to 8 hours resulted in 25% and 8% increase in surface area of particles produced in n-decane and hexadecane, respectively. Iron oxide particles produced in n-decane had smaller particle diameters and higher surface area then those produced in hexadecane. However, there was a trade off in having produced iron oxide nano-particles in n-decane compared to hexadecane. The reaction processed at a lower rate in n-decane than hexadecane, thus resulting in lower product yield.

Chapter 6: Characterization and Activation of Biochar

6.1 Introduction

Commercially available activated carbons are produced by carefully controlling the process of carbonization, dehydration, and oxidation of organic matter. The most commonly used organics included coal, lignite, wood, coconut shell, and other agricultural residues. Pyrolysis of these materials normally leads to a porous structure mainly formed of carbon (biochar). Unfortunately, the resulting material has low surface area thus low adsorption capacity. This issue can be resolved by "activating" the carbon by introduction it to an oxidizing agent in a form of gas or chemical agents[121-124].

The use of chemicals for activation is known as chemical activation. The most commonly used chemicals in this process are phosphoric acid (H_3PO_4), zinc chloride ($ZnCl_2$), potassium hydroxide (KOH), and sodium hydroxide (NaOH). The main advantages of chemical activation are higher yields, lower activation temperatures, less process time, and generally higher formation of porosity. The disadvantages are that the activation agents are expense relative to physical activation, an additional washing stage is added to the method, and hydroxides are very corrosive, and need proper disposal. Nonetheless, chemical activation is still a popular method for activating carbons[125-127].

A large literature has been published on different chemical agents being used for formation of activated carbons. Ros et al.[128] used physical (CO_2) and chemical activation (H_3OH, NaOH, and KOH) to activate sewage sludge-based precursors. The results showed that CO_2 and H_3OH lead to BET surface area of 1-300 m^2g^{-1}, making them not every effective. However, the hydroxides lead to a much higher BET surface area 300-450 m^2g^{-1} when the ratio of

hydroxides:precursor was 1:1. Once the ratio of hydroxides:precursor was increased to 3:1 the calculated surface area increased to as much as 1700 m^3/g. Macia-Agullo et al.[122] also tested the performance of physical and chemical activation on carbon fibers. Physical activation was done by steam, while chemical activation was done with KOH and NaOH. They concluded that chemical activation leads to higher porosity, and thus higher surface area on carbon fibers. In addition, they found that chemical activation leads to higher yields and the surface is less damaged in compression to physical activation.

Chemical and physical activation of coal based carbons was conducted by Ahmadpour and Do[126]. A series of activated carbons were prepared using potassium hydroxide and zinc chloride for chemical activation and CO_2 for physical activation. They found that chemical activation done at lower temperatures with KOH resulted in higher surface area compared to $ZnCl_2$. Nonetheless, $ZnCl_2$ produced higher surface area and yield when compared to KOH. Meanwhile, physical activation of coal char with CO_2 led to highest measured surface area overall, when the activation time was allowed to continue for 20.5 hours.

The combination of physical and chemical activation of carbon is known as physicochemical activation. Hu and Srinivasan physicochemically activated coconut shell based carbon with $ZnCl_2$ plus CO_2 to form mesoporous activated carbon[129]. Physicochemical activation leads to a higher surface area (1000-2700 m^2g^{-1}) meaning higher mesoporosity. An activation time of four hours produced the highest surface area with 20% yield at 800°C. Activation of waste tires was studied by Ariyadejwanich et al.[130] The tires were initially carbonized at 500°C under N_2 and the char obtained was characterized. The BET surface area and mesopore volumes were found to be 737 m^2g^{-1} and 1.09 cm^3g^{-1} respectively. To further improve porosity, the char was treated with

1M HCl at room temperature for one day and then steam activated. The resulting surface area and mesopore volume increased to 1119 m^2g^{-1} and 1.62 cm^3g^{-1}.

Activation of carbon by steam and CO_2 has also been extensively studied. Molina-Sabio et al.[131] studied the effects of steam and CO_2 activation on microporosity of the carbon. It was found that CO_2 activated carbon exhibited a large micropore volume and a narrower micropore size distribution then those prepared by steam. Micropore widening is the predominate effect of steam activation, while the development of narrow microporosity is the effect of CO_2. Effects of burn-off and activation temperature were studied by Chang et al[132]. Steam and CO_2 were used as activation agents to form activated carbon from corn cob. The activation took place at 800 °C and 900 °C within the limits of 50 wt% burn-off. The steam was carried using N_2 at100 cm^3-min^{-1}, while CO_2 was flown at 200 cm^3-min^{-1}. They concluded that higher activation temperatures can account for shorter activation times to form high surface area carbon. The largest BET surface area obtained from CO_2 activation at 900 °C with 71 wt% burn-off was 1705 m^2g^{-1}. They also observed that the levels of development and widening of microporosity depends on activation temperature, time, and gasifying agents. Comparing the BET surface area from both the agents at 900°C indicated that steam in N_2 with a concentration of 40 vol% as an oxidizing agent was more favorable than pure CO_2.

Azargoha and Dalai compared experimental and simulation work on steam and KOH activation of biochar[133]. They developed two models: one was for BET surface area and the product yield as a function of activation conditions; the second was an optimization of the operating conditions to produce activated carbon with relatively high surface area and large yield. During steam activation the resulting BET surface area was increased by increasing the temperature but volume yield decreased. It was also noted that increasing the amount of oxidizing

agent had similar effects on the process. During KOH activation BET surface area increased with temperature and flow-rate of N_2. Study of jute stick char derived from the pyrolysis process for bio-oil production thermally activated under steam was done by Asadullah[134]. The char was activated between 700-850 °C at 150 ml-min^{-1} N_2 flow rate with different ratios of steam to N_2. Increasing temperature beyond 850 °C resulted in higher burn-off and lower BET surface area. Increasing the steam to N_2 ratio above a certain limit also resulted in high burn-off.

Sugarcane bagasse was carbonized and activated under CO_2 atmosphere at various periods of time from 1 to 15 hours by Valix and coworkers[135]. Thermal carbonization of bagasse generated surface areas as great as1579 m^2g^{-1} when it was activated for 15 hours. Increased activation time was shown to increase the measured surface area in this study. The surface pH of the char shifted from highly acidic to neutral values 6-7 after activation.

The intent of this study was to carefully characterize and prepare high surface area adsorbents from various premade biochars for H_2S adsorption. Physical activation with O_2 (air), and CO_2 were carried out and the effects of different oxidizers, activation time, temperature, and flow rate were closely investigated. The biochar samples were characterized by evaluating the surface chemistry with pH measurements and surface morphology with a SEM and XRD.

6.2 Experiment

6.2.1 Materials

Four sets of biochar pellets were used in this study. Set-1 was derived from hardwood ($BC\text{-}1_o$), set-2 was blend of chicken waste plus hardwood ($BC\text{-}2_o$), set-3 was switchgrass ($BC\text{-}3_o$), and set-4 blend of swine waste plus rye ($BC\text{-}4_o$). The biochar samples were donated by The United

States Department of Agriculture (USDA) and North Carolina State University. The oxidized samples were labeled as BC-1, BC-2, BC-3 and BC-4.

6.2.2 Characterization

Biochar was characterized using a number of different techniques to better understand its physical and chemical properties. Surface and elemental analysis was accomplished using a SEM equipped with an EDAX, and powder XRD. N_2 isotherms were measured using a Micromertics TriStar 3000 analyzer at -198 °C. Before analysis, the samples were degassed at 350 °C for four hours. The BET surface area was calculated by using the BET equation, and the Langmuir surface area using the Langmuir equation. Micropore volumes were calculated by Dubinin and t-plot methods. Bulk density of the samples was calculated from the weight of the biochar at 22 °C , that is contained within a volume of 10 cm^3. pH value of biochar and activated product were measured according to ASTM D3838 (10 g of biochar was added to 100 ml of DI water; the mixture was boiled for 15 minutes and filtered out; the pH of the product was measured).

6.2.3 Process

6.2.3.1 Biochar Activation

Figure 6.1 shows the schematic diagram of the experimental setup. A fixed bed quartz reactor with a Lindberg/Blue M tube furnace was used to produce activated carbons from biochar. Five grams of sample was loaded into the reactor and heated at 20 °C-min^{-1} under N_2 atmosphere. Upon reaching the activation temperature the oxidizing agent was introduced into the system. The biochar was activated at different temperatures, time, and flow rates according to experimental design. At the conclusion of the run, the reactor was cooled to room temperature under N_2. The resulting sample was passed through a 250 µm size sieve to remove any ultrafine particles and ash

that may have been produced during the process. Surface area and pH measurements of the product were carried out.

1) Quartz Tube
2) Tube Furnace
3) 3 way-valve
4) N_2 gas tank
5) CO_2/air gas tank

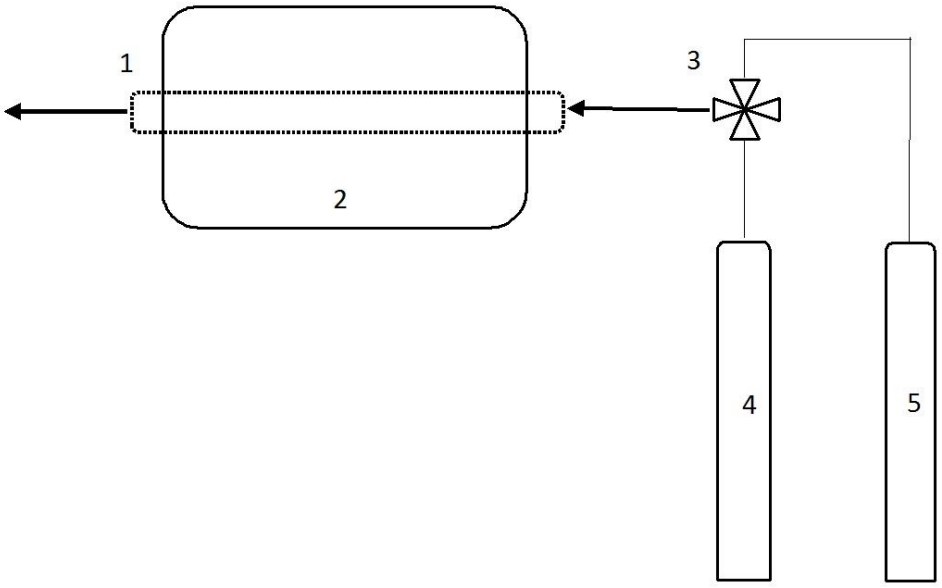

Figure 6.1: *Biochar activation unit setup.*

6.3 Results and Discussions

The usefulness of activated carbon is based its adsorption capacity which is limited by the specific surface area, pore volume and pore size distributions. In most cases, a higher surface area indicates a larger pore volume, thus a larger adsorption capacity. Use of an oxidizer to develop highly porous carbon is therefore desirable. Process temperature, time, and flow rate of the oxidizing agent play important roles in developing porosity in activated carbon. In most instances, three stages of pore development takes places during activation process: (i) development of

previously inaccessible pores; (ii) development of new pores; (iii) widening of the existing pores[53, 56, 136].

6.3.1 Surface Analysis Pre-Activation

In order to understand adsorption behavior of different biochar samples, the physical structure and surface chemistry of the samples were investigated. The microscopic structure of BC-1_o, BC-2_o, BC-3_o, and BC-4_o are shown in Figure 6.2. The images show a highly ordered skeletal frame left behind from volatiles escaping during thermochemical degradation. Each sample displayed a unique structural features based on the structure of the starting feedstock and pyrolysis conditions. The SEM micrograph shows porous structures on the surface of the biochar. The macroporosity of the biochar ranged from 2-15 μm. Unfortunately, this macroporosity does not contribute the adsorption capacity of the biochar, though it lead to the underlying meso and microporosity, which does play an important role in adsorption. The presence of such voids was an encouraging sign as a potential candidate for gas adsorption.

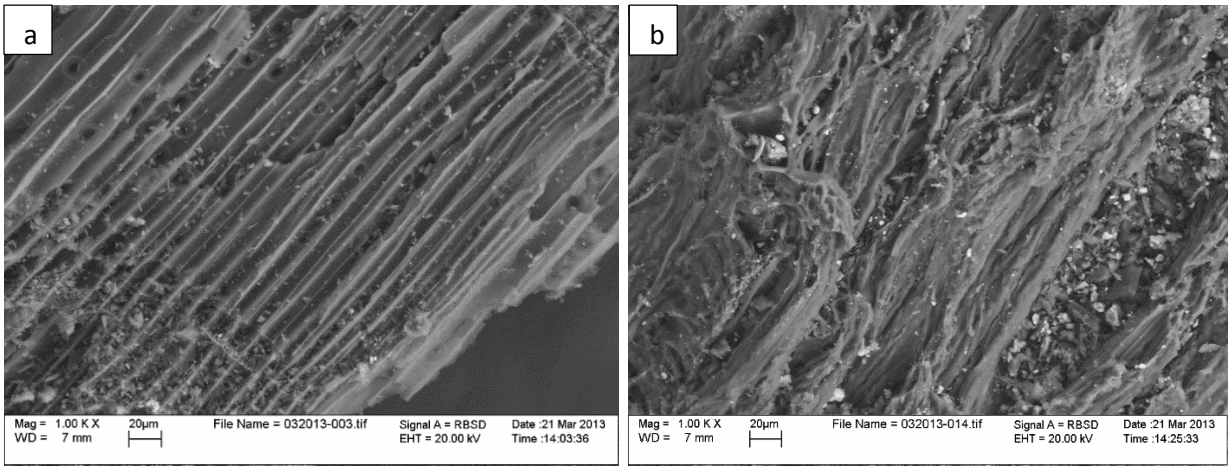

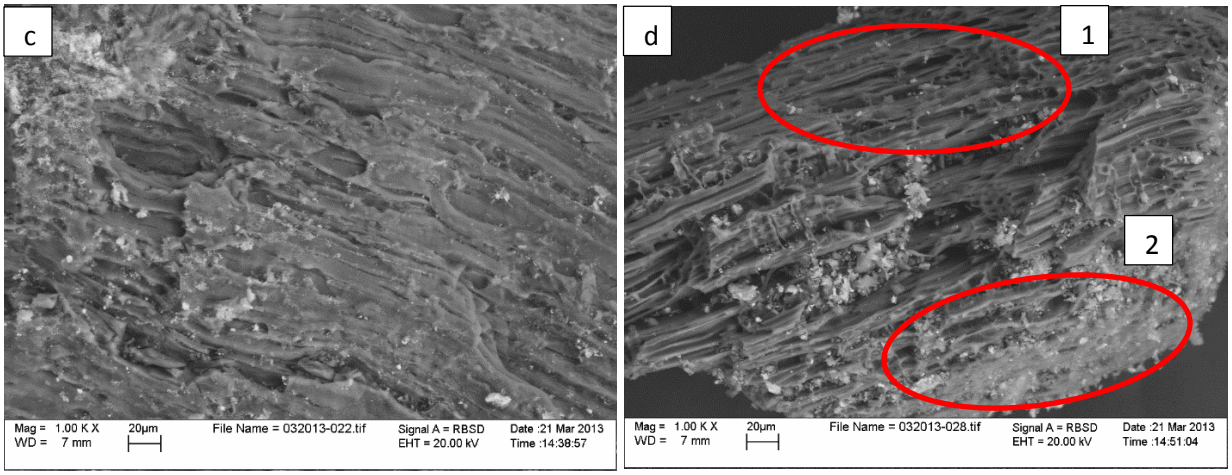

Figure 6.2: *SEM micrograph of (a) BC-1_o, (b) BC-2_o, (c) BC-3_o, and (d) BC-4_o sample. Each sample has its own unique features based on the physical structure of the feedstock it is derived from.*

Figure 6.2a shows the existence of long narrow channels on the BC-1_o sample. These narrow channels are known to form in wood based carbons. The presence of cellulose, hemicellulose, and lignin in the feedstock was responsible for these channeled structure in BC-1_o. The mixture of volatile organics and hardwood gave BC-2_o a randomized structure with no well-defined form. Smaller channel like structures were identifiable in the BC-2_o but were not as prominent as ones in BC-1_o. Images of sample BC-3_o showed a flat featureless surface much different than other samples. This was likely due to the high pyrolysis operating temperature. The surface of BC-3_o lacked evidence of macroporosity as observed in other samples. Sample BC-4_o shows two unique features on its surface as seen in Figure 6.2d. Region 1 shows long narrow channels equivalent to BC-1_o, while region 2 was more flat and featureless. This may be due to uneven mixing of the feedstock or low concentration of the swine waste. The BC-4_o surface showed evidence of large amount of macropores.

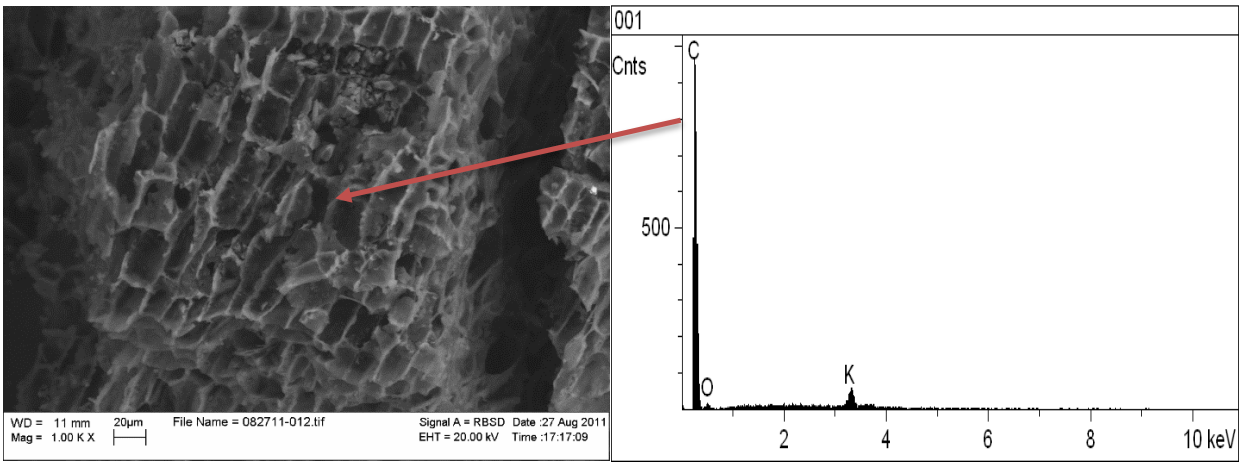

Figure 6.3: *SEM micrograph of BC-1 sample with its corresponding EDAX spectra. Long narrow channels on the surface of the sample are observed.*

The surfaces of these sample included seattered with heavy metals. The white spots in the SEM images show the extent at which these minerals exist on the surface of the biochar samples. Figure 6.4a shows the presences of metal oxides on the surface of BC-2. The existent of iron oxide particles on the surface of the char highlights another path for decomposition of H_2S on the biochar surface. The reaction between iron oxide and H_2S leads to[33, 137]:

$$Fe_2O_3 + 3H_2S \xrightarrow{yields} FeS + FeS_2 + 3H_2O, \tag{19}$$

$$Fe_2O_3 + 3H_2S \xrightarrow{yields} Fe_2S_3 + 3H_2O. \tag{20}$$

It was likely that H_2S oxidation was taking place simultaneously on the carbon surface via adsorption and catalytic conversion over metal oxides. The utilization of such metal oxides was highly dependent on the operating temperature of the system. This can vastly improve the adsorption capability of carbon. Figure 6.4b shows large amount of alkali salts, in the form of sodium, chloride, and potassium, present on surface of BC-2_o, and BC-4_o. Smaller quantities of these salts were also present on BC-1_o and BC-3_o samples. Presence of salts were linked to the

starting composition of the feedstock being used to produce the biochar. Samples derived from animal waste, BC-2_o and BC-4_o, had larger amount of these salts present compared to BC-1_o and BC-4_o as expected. Occurrence of such particles greatly affects the surface chemistry of the samples.

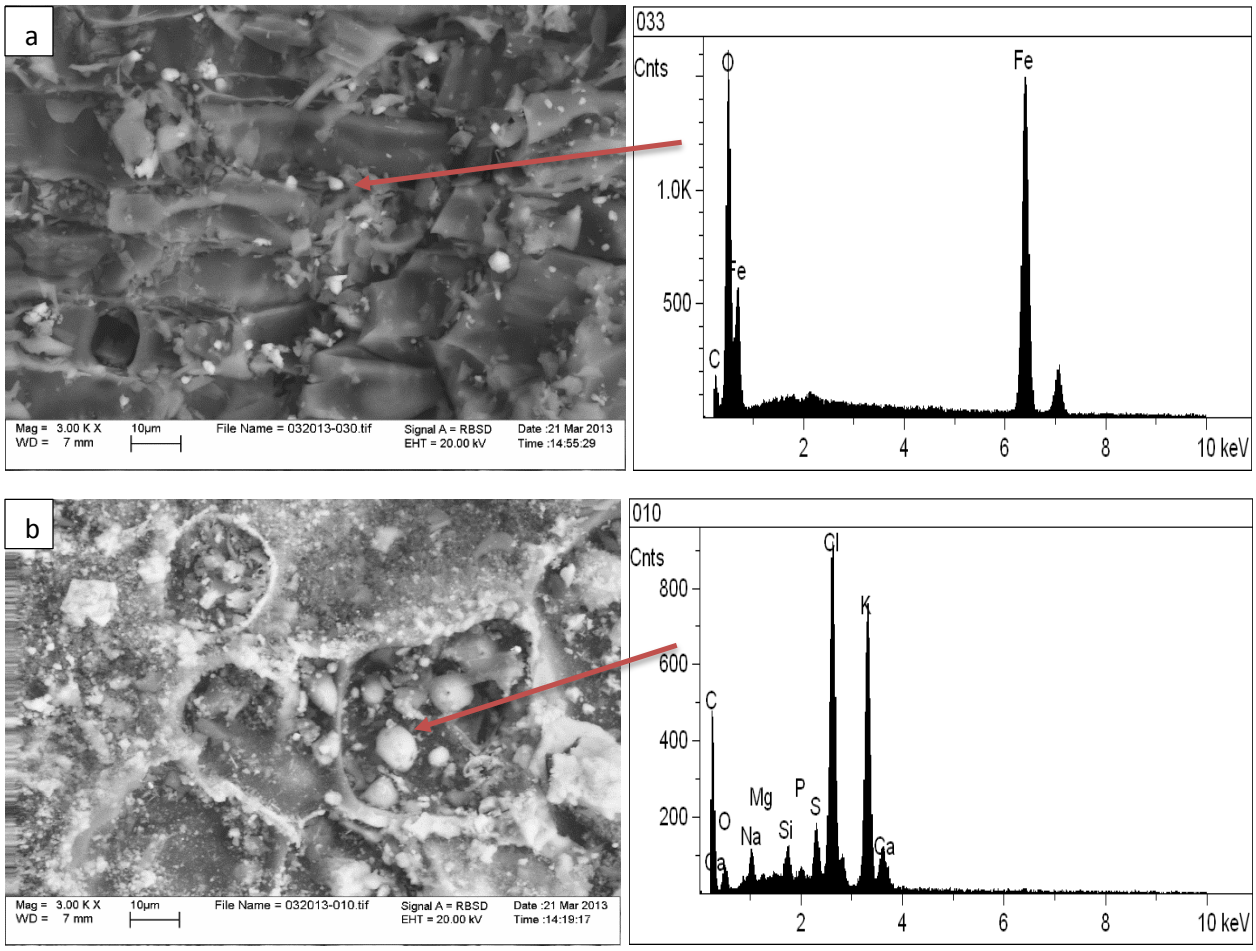

Figure 6.4: *(a) EDAX spectra of BC-2 confirmed the presence of metal oxides including iron-oxide. (b) Large amount of salts present on the surface of BC-2 can be seen under the SEM.*

The surface chemistry of biochars was determined by measuring the surface pH and identifying surface functional groups of the samples. The identification of surface functional groups is significant to promote the applicability of activated biochars for H_2S adsorption. Figure 6.5 shows the FTIR spectra for sample BC-1_o, BC-2_o, BC-3_o, and BC-4_o over the wavelength range

of 4000-380 cm^{-1}. Samples BC-1_o and BC-2_o showed no identifiable peaks in their FTIR spectra. Sample BC-3_o and BC-4_o showed sharp peaks at 1100-1000 cm^{-1} assigned to C-O stretching vibrations of carboxylic acids, esters and ethers groups. The 790 cm^{-1} peak in BC-3_0 was assigned to C-H bending of aromatics. Sample BC-4_o showed a peak at 555 cm^{-1} representing C-Cl stretching in alkyl halides.

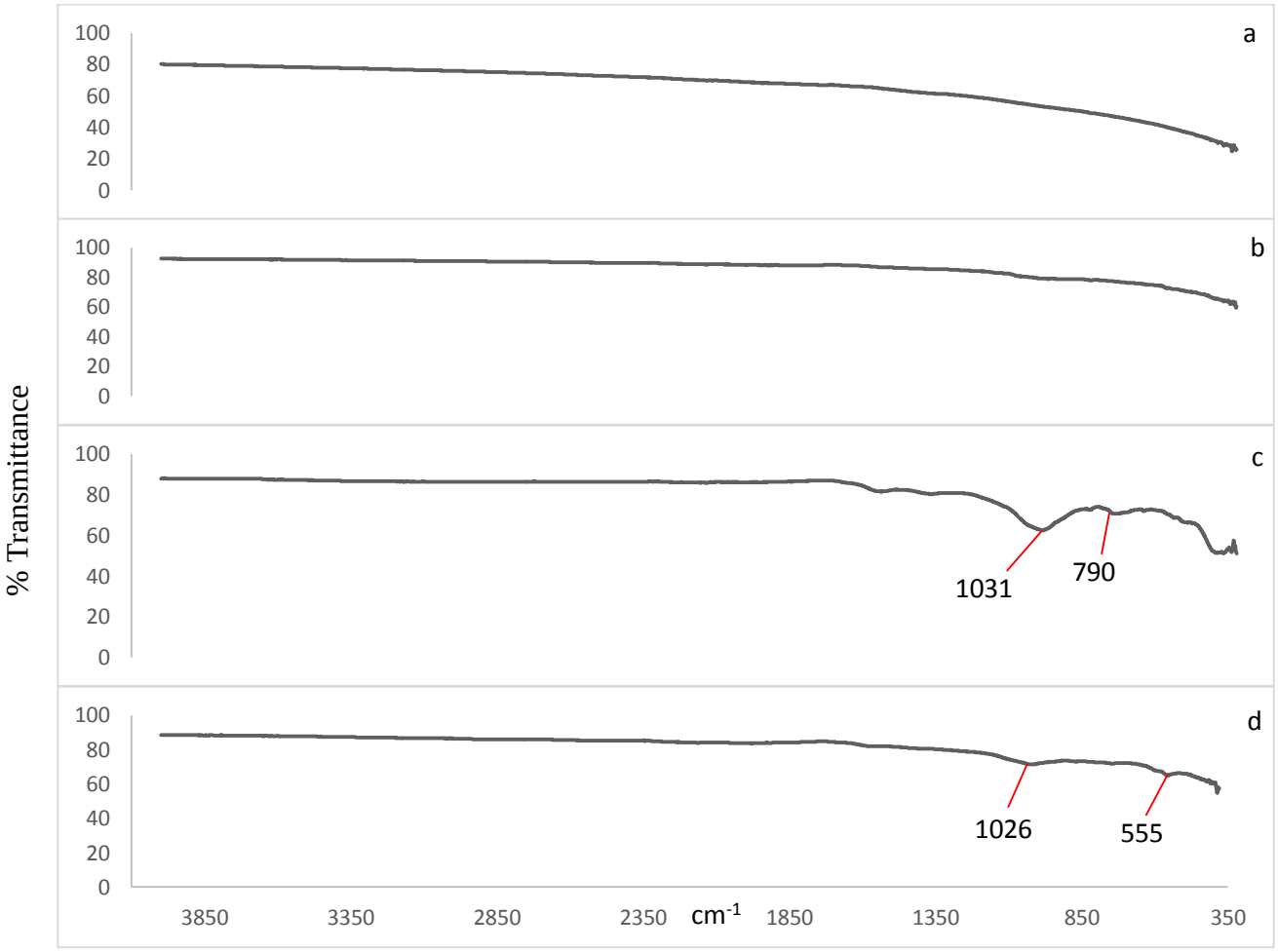

Figure 6.5: *FTIR spectra of (a) BC-1_o,(b) BC-2_o, (c) BC-3_o, and (d) BC-4_o.*

The pH values of BC-1_o, BC-2_o, BC-3_o, and BC-4_o are given in Table 6.1. The results suggested that basic functional groups existed on the surface of the carbons. Sample BC-3_o had highest pH value of 9.44 while BC-1_o had the lowest value at 6.64. The presences of basic

functional groups on the surface of BC-2_o, and BC-4_o was explained by the large amount of alkali salts observed their surface. The importance of the pH level of carbon surfaces and its effectiveness as a sink for H_2S has been closely studied. Bagreev et al.[59] concluded that unmodified carbons with a surface pH greater than 5.0 tended to be effective adsorbents for H_2S. Additionally, it should be noted that surface pH is a parameter related to the heat of immersion, electron work function, and zeta potential, which are linked to the catalytic activities of carbons in electron transfer reactions.

Sample	pH	Bulk Density (g cm^{-3})	BET (m^2 g^{-1})
BC-1_0	6.64	0.42	<0.5
BC-2_0	8.80	0.50	<0.5
BC-3_0	9.44	0.23	<0.5
BC-4_0	9.43	0.57	<0.5

Table 6.1: *Initially measured pH and bulk density of all the samples.*

Table 6.1 also shows the bulk densities of the biochar samples. Sample BC-4_o contained the largest measured bulk density at 0.57 g-cm^{-3}, while BC-3_o had the lowest at 0.23 g-cm^{-3}. The bulk densities of BC-1_0, BC-2_0, and BC-4_0 were in range of commercial activated carbons used for gas adsorption. The bulk densities of the samples decreased with increased ash content and process temperature. This was evident from the ash content produced from each of the samples. BC-3 sample had the highest ash contents at 1.2 wt%. This resulted in a lower bulk density compared to other samples. The surface areas of all the samples in their initial state were

significantly lower than commercial activated carbons (500-1200 m^2g^{-1}). The surface area of BC-1_o, BC-2_o, BC-3_o, and BC-4_o were well below the resolution limit of the instrument (<0.5 m^2g^{-1}) therefore exact values could not be reported. The XRD measurements of the BC-1_o confirmed its amorphous nature but contained some local crystalline structures. Majority of the XRD spectra was smoothly curved, expect for small peaks at 2θ = 29°, 39°, 43°, 47°, and 48° as seen in Figure 6.6.

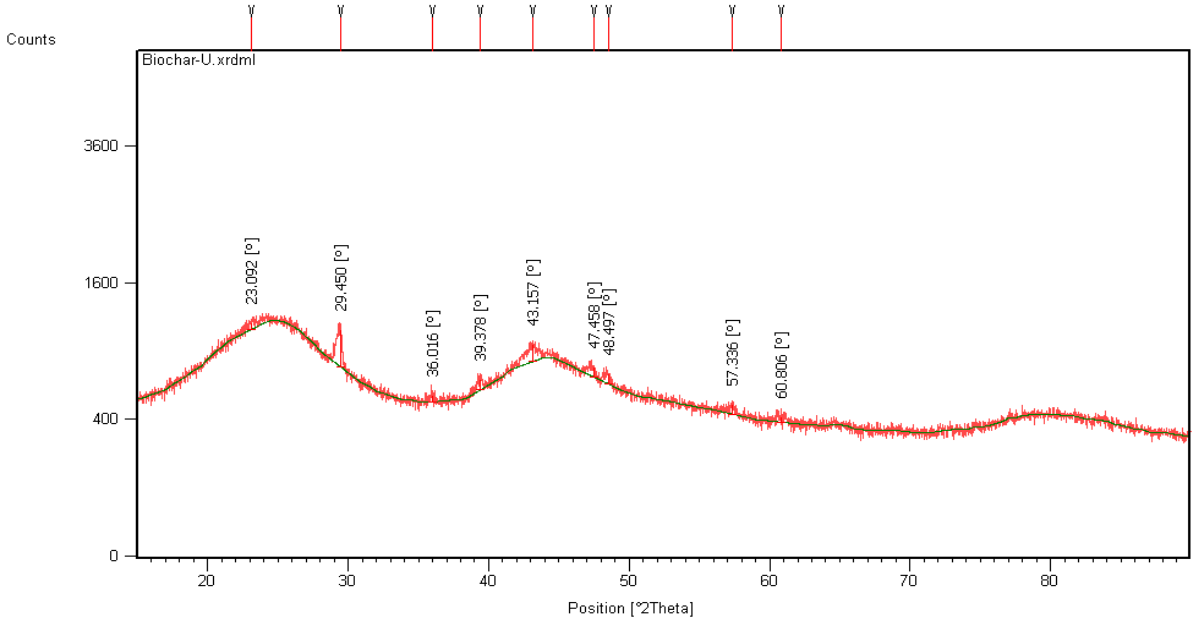

Figure 6.6: *XRD spectra of BC-1_o sample. The Amorphous nature of the biochar is highlighted by the lack of sharp diffraction peaks.*

6.3.2 Surface Analysis Post-Activation

Physical activation with oxidizing agents such as air and CO_2 involves C-O_2 and C-CO_2 reactions, respectively, which resulted in the removal of C atoms and caused weight loss in the resulting char. At elevated temperatures the first layer of C on the external surface was removed, forming microporosity. These microspores allow entry to the underline layers of the biochar. In this manner the crystalline structures were exposed to the oxidizing agent. This leads to further

development of meso and microporosity with increasing burn-off. The extent of burn-off was closely related to the amount of activation that took place.

The choice of oxidizing agent greatly affects the development of porosity in the activated carbon. Equation (21) describes the endothermic reaction that took place when CO_2 was introduced onto the carbon, while gasification by O_2 was an exothermic reaction as described by Eq. (22)-(23).

$$C(s) + CO_2(g) \xrightarrow{yields} 2CO, \tag{21}$$

$$C(s) + O_2(g) \xrightarrow{yields} 2CO, \tag{22}$$

$$C(s) + O_2(g) \xrightarrow{yields} CO_2. \tag{23}$$

The reactions of CO_2 and O_2 with C surface also produced chemisorbed surface oxygen complexes, which possessed a broad range of chemical functionality. The formation of these O_2 complexes were highly dependent on the temperature and oxidizing agent being used. In most instances O_2 was chemisorbed on the surface of the C via:

$$C(s) + CO_2 \xleftrightarrow{Yields} CO + C(O), \tag{24}$$

where C(O) is shorthand for surface O_2 complexes. During activation these surface O_2 complexes play a duel role as reaction initiators and inhibitors during gasification of the carbon. During C-CO_2 interaction surface oxygen complexes become stable under the reaction conditions and act as inhibitors by blocking reaction sites:

$$C(O) \xleftrightarrow{Yields} C - O. \tag{25}$$

They also decomposed and left the surface as CO, thus leaving free carbon sites for reactions to take place[53]. In this manner the surface oxygen complexes played an important role in determining the degree of porosity formation.

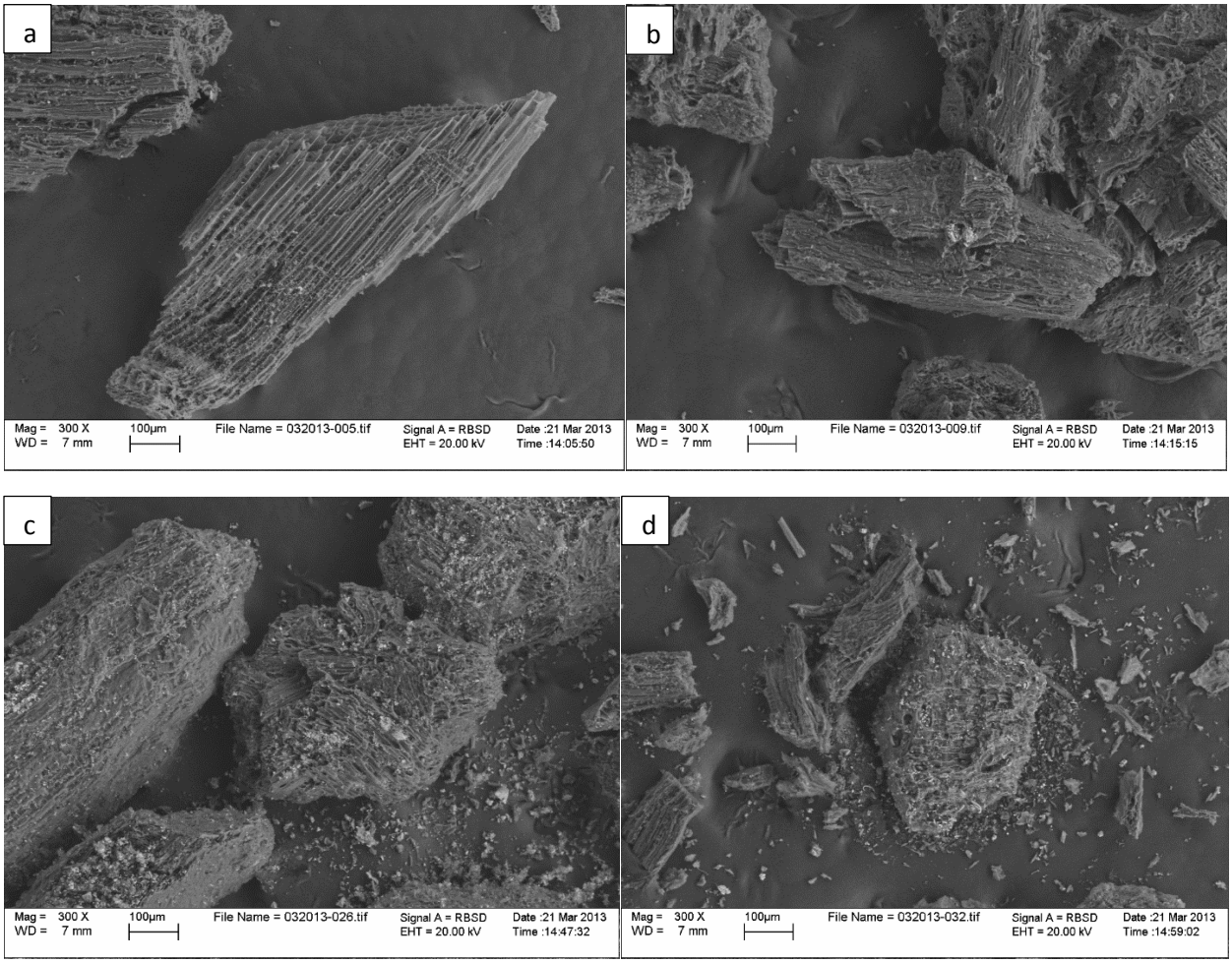

Figure 6.7: *Post-activated images of (a) BC-1_o, (b) BC-2_o, (c) BC-3_o, and (d) BC-4_o.*

Post-activation imaging of the BC-1 sample did not show any observable structural change (see Figure 6.7). In contrast, BC-2 shows a slightly more ordered structure with formation of long ridges, resembling a series of parallel lines. The amount of observable alkali salts had decreased on the surface of BC-2. The surface of BC-3 showed a more textured surface with large

development of macropores. BC-4 developed a more uniformly channeled structures rather than what was seen in BC-4_o.

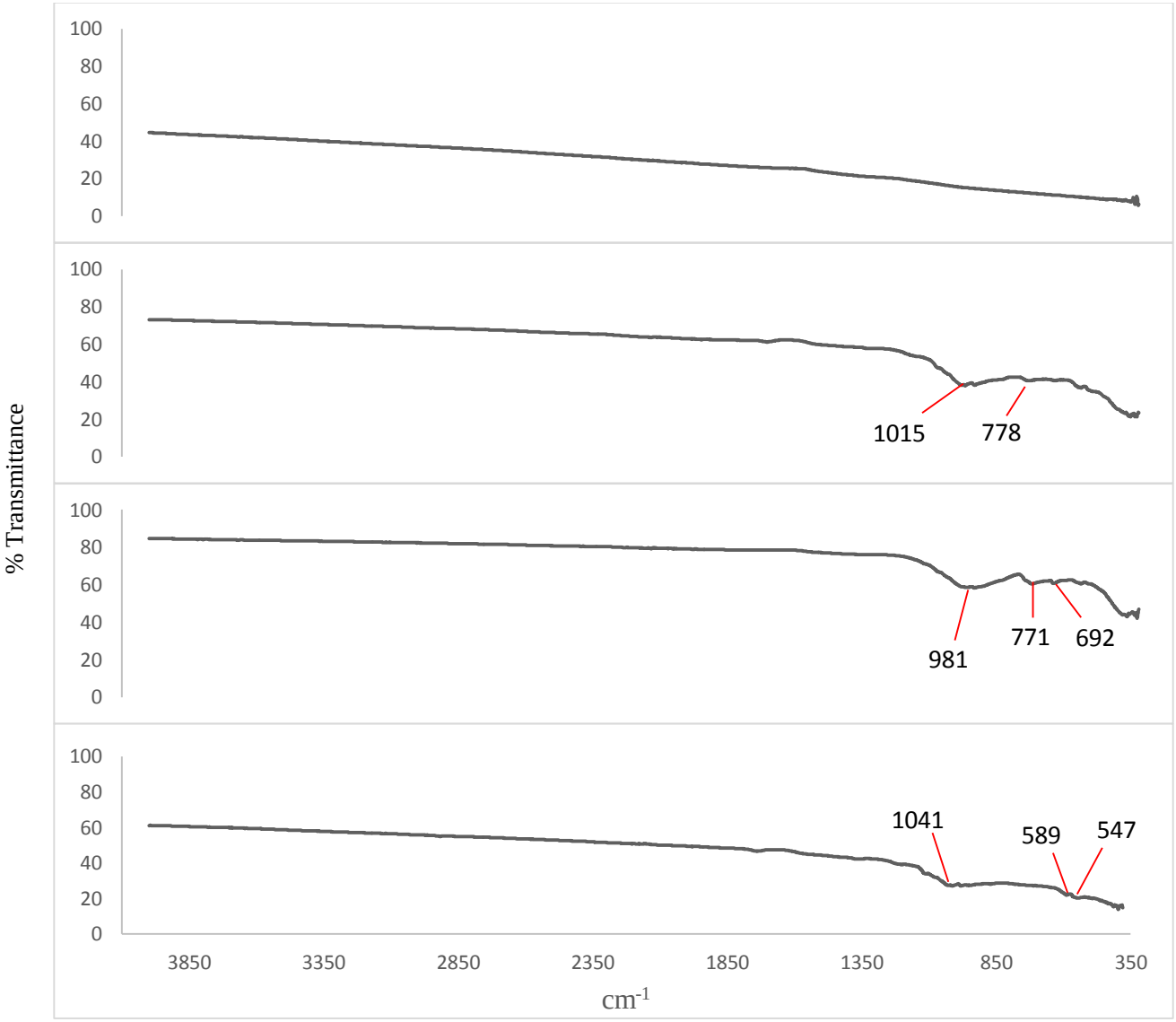

Figure 6.8: *FTIR spectra of post-activated biochar sample (a) BC-1, (b) BC-2, (c) BC-3, and (d) BC-4.*

The change in surface chemistry after activation was studied. Four samples activated at 900 °C for 60 minutes under CO_2 oxidization were analyzed using a FTIR (see Figure 6.8). Sample BC-1 was comparable to BC-1_o as no peaks were observed even after activation. Once more, bands at 1100-1000 cm^{-1} were assigned to C-O stretching vibrations of carboxylic acids, esters and

ethers groups. The strong bands at 1000-750 cm^{-1} were assigned to =C-H bending vibration of alkenes. Sample BC-3 and BC-4 showed peaks between 600-550 cm^{-1} assigned to C-Cl stretching of alkyl halides. A peak at 692 cm^{-1} in BC-3 was assigned to N-H in amines. A strong peak at 1738 cm^{-1} was given to C=O stretching in esters, and saturated aliphatic in BC-4.

6.3.3 Effect of Temperature on the Yield and Surface Area

Experiment No:	T_f (°C):	BET:	Langmuir:	pH	Burn off:
1	275	416.18	536.94	8.54	27%
2	375	564.79 ± 22.02	782.19 ± 9.10	7.40	82%
3	475	458.96 ± 19.14	669.08 ± 5.27	10.12	65%
4	575	423.91 ± 16.7	581.73 ± 4.8	9.69	69%

Table 6.2: *Sample: BC-1; Oxidizer: O_2; Activation Time: 3 hrs; Flow Rate: 200 ml min^{-1}.*

The results of BC-1 activation via O_2 are given in Table 6.2. The largest surface area (564 m^2g^{-1}) development took place at 375 °C, after which decrease in surface area occurred with increasing temperature. Oxidizing via air (an exothermic reaction) resulted in consumption of C material without enhancement in porosity at temperatures above 375 °C. During the course of oxidation the outside surface was completely consumed without O_2 penetrating the interior of the carbon. Extensive burn-off of the C layers caused the collapse of the pore walls and led to decrease in surface area. Surprisingly, the burn-off percentage was only 69% at 575 °C compared to 82% at 375 °C. Applying least-square regression analysis expressed in terms of degree of burn-off to BET surface area, a correlation coefficient $R^2 > 0.48$ was found.

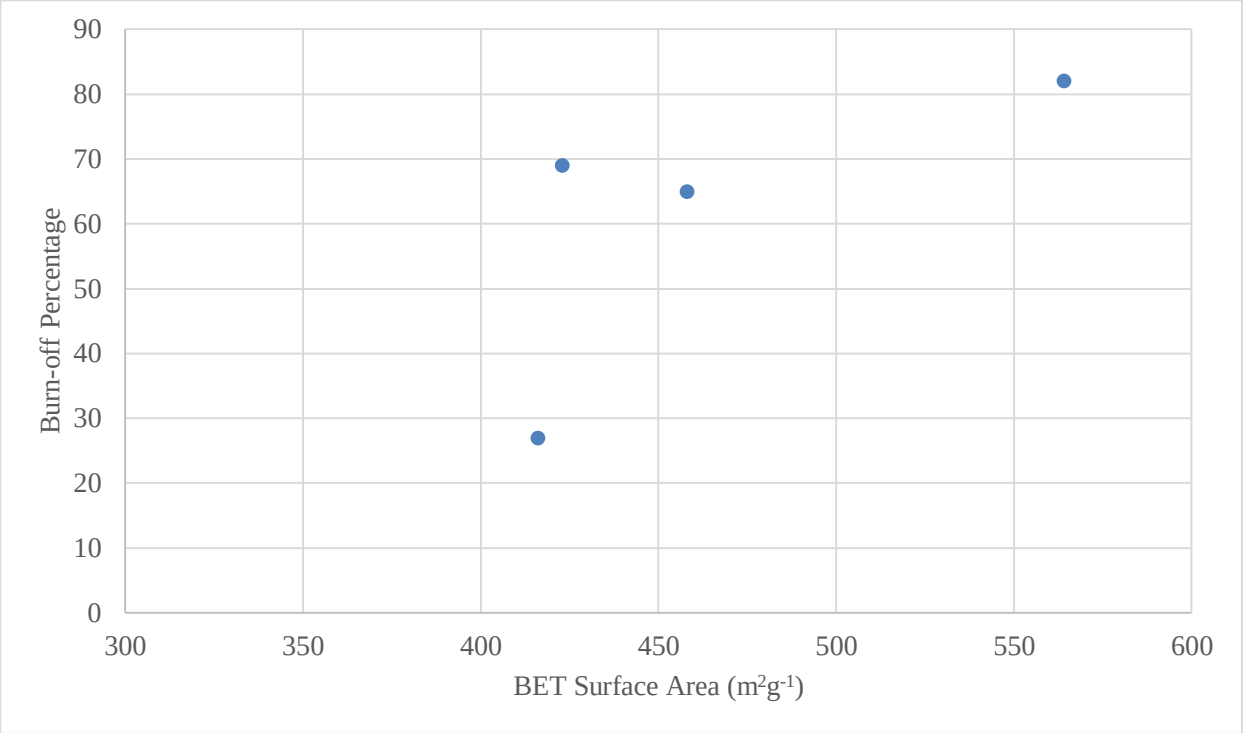

Figure 6.9: *Linear regression analysis of burn-off vs surface area when BC-1 was oxidized under O_2.*

Samples were activated from 750-850 °C for three hours at 200 ml min^{-1} flow rate of CO_2. The results from these experiments are shown in Table 6.3. Sample BC-1 attained the maximum surface area value of 1103 m^2g^{-1} at 850 °C with 86% burn-off. The largest surface area values for BC-2 (504 m^2g^{-1}), BC-3 (343 m^2g^{-1}), and BC-4 (461 m^2g^{-1}). Activation of BC-2 at 850 °C resulted in 100% burn-off of the sample. Sample BC-3 showed no significant improvement in surface area when temperature was increased from 750 °C to 850 °C. When activated at 750 °C, BC-4 failed to develop any additional surface area but it showed a loss of mass and increase in surface pH value. As expected, the pH values of the all activated samples shifted strongly towards the basic region. This was consistent with previous reports that suggest basic surfaces are generated with activation at temperatures above 700 °C. This basic property makes biochar a more favorable adsorbent for gas phase effluents, such as H_2S.

Sample:	Experiment No:	T_f (°C):	BET:	Langmuir:	pH:	% Burn off:
BC-1	1	750	711.80 ± 28.27	1005.83 ± 9.2	9.6	54%
BC-1	2	800	1039.88 ± 41.76	1438.91 ± 14.60	10.10	68%
BC-1	3	850	1103.09 ± 44.61	1538.22 ± 15.06	11.14	86%
BC-2	4	750	504 ± 20.28	697.12 ± 4.4	10.32	35%
BC-2	5	800	257.55 ± 1.6	355.61 ± 8.56	11.36	64%
BC-2[I]	6	850	-	-	-	100%
BC-3	7	750	343.17 ± 7.8	458.6 ± 2.25	9.72	48%
BC-3	8	800	342.03 ± 7.39	459.09 ± 3.04	9.68	50%
BC-3	9	850	178.78 ± 2.8	240.79 ± 2.8	10.10	84%
BC-4[I]	10	750	-	-	11.18	34%
BC-4	11	800	357.02 ± 7.6	481.99 ± 3.26	9.32	54%
BC-4	12	850	461.94 ± 10.5	620.45 ± 4.11	10.58	61%

Table 6.3: *Oxidizer: CO_2; Activation Time: 3 hrs; Flow Rate: 200 ml min^{-1}. [I]Surface area could not be calculated for these samples due to lack of sample or activation.*

Linear regression studies were carried out. A positive linear correlation was established between the activation temperature and burn-off degree for all four samples. A R^2>0.79 confirmed that increased activation temperature leads to higher degree of burn-off. Both BC-1 and BC-4 showed a positive linear trend between surface area and activation temperature with R^2>0.86.

Meanwhile, BC-2 and BC-3 show inversely linear trend between surface area and activation temperature with R^2>0.75. This indicated that surface area (as function of activation temperature) was dependent on the physical structure and the chemical makeup of the biochar.

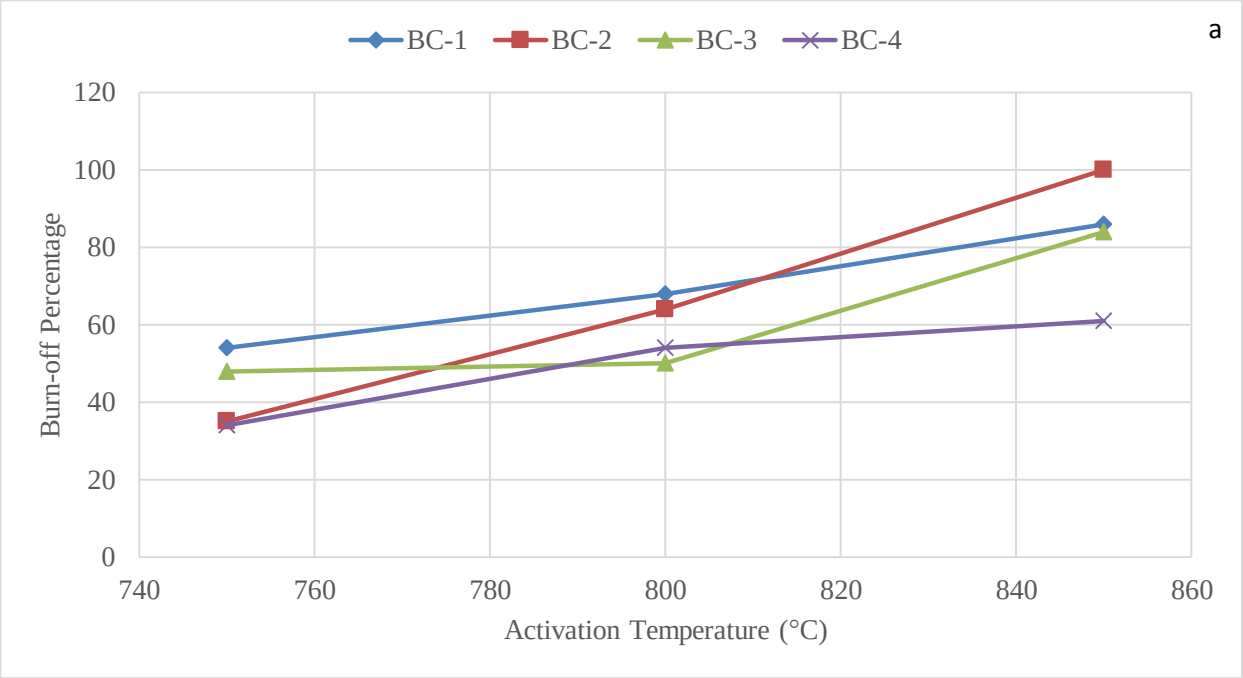

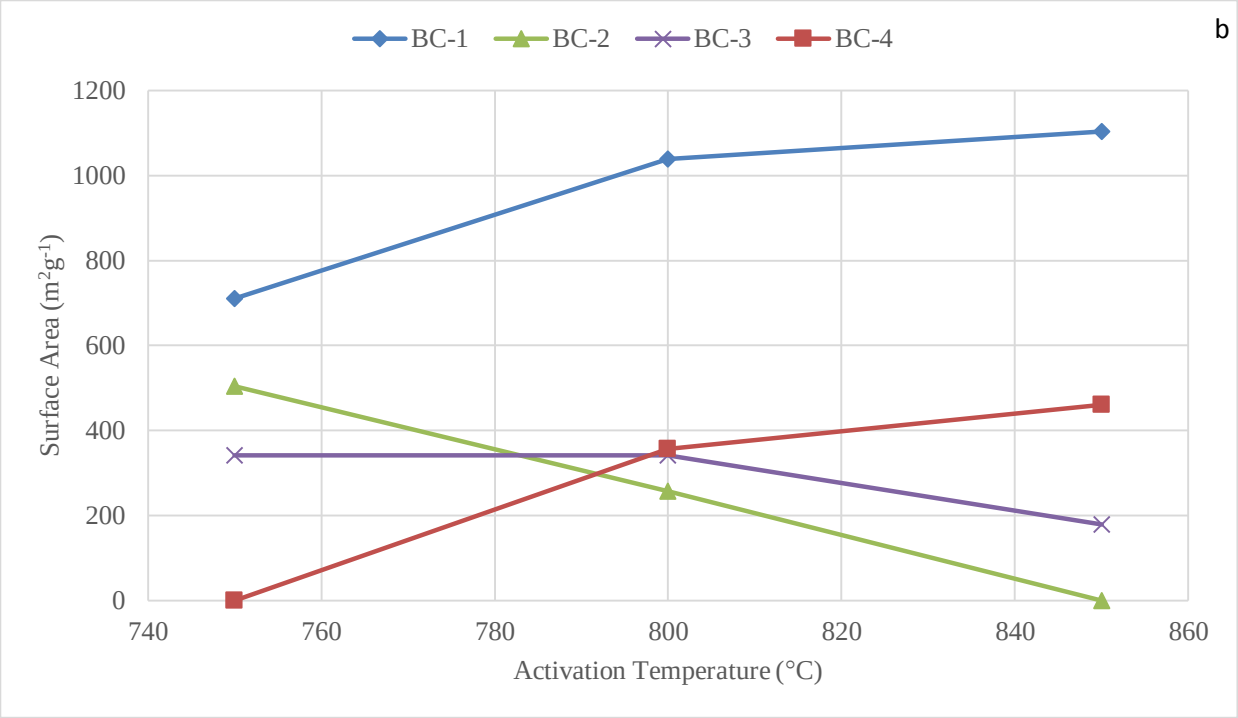

Figure 6.10: *Linear analysis of (a) activation temperature vs burn-off percentage and (b) activation temperature vs surface area.*

6.3.4 Effect of Activation Time on Burn-off and Surface Area

The effects of activation time on surface area and burn-off was studied. Samples BC-1, BC-2, BC-3, and BC-4 were activated at 900 °C for 60, 75, and 90 minutes under 200 $ml^{-}min^{-1}$ flow of CO_2. Additional, BC-1 and BC-2 were chosen to be activated for an extended time period, where they were subjected to 2-5 hours of activation under CO_2 flow rate of 200 $ml\text{-}min^{-1}$. The temperatures at which these samples were activated were chosen based on the results from section 6.3.3. A balance between product yield and surface area was the deciding factor at which temperature the samples were activated. The BC-1 samples were activated at 800 °C and BC-2 sample was activated at 750 °C.

BC-1 sample activated at two hours had a calculated BET surface area of 912 m^2g^{-1} with 54% burn-off compared to 68% burn-off at three hours and a surface area of 1039 $m^2\ g^{-1}$. Further

increase in activation time to five hours showed burn-off of ≥99% with surface area of 321 m^2g^{-1}. An extended period of activation with CO_2 caused a reduction in surface area by nearly 70% with excessive burn-off. The BC-2 sample oxidized for two hours developed a surface area of 431 m^2g^{-1}, and oxidation for three hours developed a surface area of 504 m^2g^{-1}. The calculated surface area for BC-2 was comparably less than that of BC-1. Further increase in activation time for BC-2 resulted in a 100% burn-off.

Experiment No:	Run Time (hr):	BET:	Langmuir:	pH:	Burn off:
1	2	912.25 ± 35.92	1256.88 ± 12.01	10.65	54%
2	3	1039.98 ± 41.76	1438.91 ± 14.60	10.10	68%
3	5	321.38 ± 10.01	446.58 ± 4.27	10.33	99%

Table 6.4: *Sample: BC-1; Oxidizer: CO_2; T_f (°C): 800; Flow Rate: 200 ml min^{-1}.*

Experiment No:	Run Time (hr):	BET:	Langmuir:	pH:	% Burn off:
1	2	431.89 ± 13.7	603.15 ± 8.1	12.39	31%
2	3	504 ± 20.28	697.12 ± 44	10.32	25%
3	5	-	-	-	100%

Table 6.5: *Sample: BC-2; Oxidizer: CO_2; T_f (°C): 750; Flow Rate: 200 ml min^{-1}.*

Results from activation time of 60-90 mins at 900 °C are given in Table 6.6. Sample BC-1 had the highest BET surface area of 922 m^2g^{-1} for 60 minutes of activation time. The sample decreased in surface area to 799 m^2g^{-1} when activated for 75 minutes, while increasing to 866 m^2g^{-1} for activation time of 90 minutes. The largest surface area of BC-2 (543 m^2g^{-1}) > BC-4 (408 m^2g^{-1}) > BC-3 (384 m^2g^{-1}). Closer examination of the data shows that increase in activation time

from 60 to 90 mins showed no significant improvement in surface area while leading to increased burn-off percentage in BC-1, BC-2, and BC-4. The pH value of the activated carbons increased.

Sample:	Experiment No:	Run Time (min):	BET:	Langmuir:	pH	Burn off:
BC-1	1	60	922.07 ± 19.76	1244.02 ± 10.42	11.65	73%
BC-1	2	75	799.89 ± 17	1076.12 ± 9.15	12.41	76%
BC-1	3	90	866.92 ± 18.78	1109.04 ± 8.44	12.40	78%
BC-2	4	60	543.98 ± 10.1	740.46 ± 7.9	11.37	53%
BC-2	5	75	530.82 ± 9.4	728.13 ± 6.8	10.97	55%
BC-2	6	90	507.21 ± 8.34	699.42 ± 7.3	11.84	51%
BC-3	7	60	157.82	215.95	13.02	50%
BC-3	8	75	384.76 ± 7.22	520.56 ± 5.6	10.45	56%
BC-3	9	90	126.59 ± 1.66	171.76 ± 2.49	9.32	64%
BC-4	10	60	388.02 ± 8.4	521.45 ± 4.07	10.47	42%
BC-4	11	75	402.62 ± 8.48	539.57 ± 4.36	10.25	44%
BC-4	12	90	408.84 ± 8.9	550.65 ± 4.08	9.76	45%

Table 6.6: *Oxidizer: CO_2; T_f (°C): 900; Flow Rate: 200 ml min^{-1}.*

6.3.5 Effects of Flow Rate on Yield and Surface Area

Sample BC-2 was activated with flow rates of 100, 200, and 300 ml-min^{-1} at 750°C for three hours under CO_2 were considered. The effect of flow rate on surface area and burn-off percentage on sample BC-2 is summarized in Table 6.7. A maximum surface area of 504 m^2g^{-1} was obtained at a flow rate 200 ml-min^{-1}. The change in surface area was limited to ±30 m^2g^{-1} between each run with relatively low degree of burn-off (<50%). Based on these results, any correlation between surface area development and flow rate was unlikely. Decrease in burn-off percentage was noted as the flow rate increased. This indicated that the oxidizing agent had less time to interact with both the internal and external surfaces of the carbon. The surface pH was highly basic.

Experiment No:	Flow Rate:	BET:	Langmuir:	pH	% Burn off:
1	100	487.90 ± 17.57	680.90 ± 7.88	12.07	45%
2	200	504.00 ± 20.28	697.12 ± 44	10.32	35%
3	300	468.35 ± 19.7	640.91 ± 3.93	13.52	30%

Table 6.7: *Oxidizer: CO_2; T_f (°C): 750; Activation Time: 3 hrs. Change in flow rate very little to no effect on surface area formation.*

6.4 Conclusion

Biochar samples of were characterized and activated using air and CO_2 as oxidizing agents. Effects of process parameters, such as temperature, time, and flow rate on surface area and burn-off percentage were studied. Prior to oxidation, biochar samples had insignificant surface areas (<0.5 m^2g^{-1}). Closer examination samples under SEM showed different structural arrangement of all samples. The structure of the biochar was directly linked to the feedstock and the conditions at

which it was manufactured. SEM imaging showed the presence of alkali salts, including sodium, chloride, and potassium, on the surface of all biochar samples. Iron oxide was also detected on the surface of BC-2. Sample BC-4 contained the largest measured bulk density at 0.57 g-cm^{-3}, while BC-3 had the lowest at 0.23 g-cm^{-3}. The initial pH values of the samples had pH values >6. Sample BC-3_o had highest pH value of 9.44, while BC-1_o had the lowest pH value at 6.64. Post-activation imaging of the samples showed development of macropores in the samples. An increase in the surface pH values was also noted after activation under O_2 and CO_2. Use of O_2 as an oxidizing agent produced BET surface area of <600 m^{2}g^{-1} and excessive burn-off (>60%). Use of O_2 as an oxidizing agent above 600 °C led to 100% burn-off of the biochar, so that it is not recommended as an oxidizer above 600 °C. Under CO_2 activation the samples showed a wide range of surface area development. The surface area attained to a maximum value (1103 m^{2}g^{-1}) at 850 °C when BC-1 was activated for three hours at flow rate of 200 ml min^{-1}. Sample BC-1 always had the highest value of surface area under all test conditions, as expected. Biochar derived from woody materials are known have robust physical structure and develop large surface areas.

Chapter 7: Hydrogen Sulfide Removal

7.1 Introduction

7.1.1 Biochar

H_2S removal is an essential step prior to utilization of biogas. Failure to remove H_2S from the gas stream can lead to corrosion of metal parts in a combustion engine or boiler. Aside from this, H_2S is toxic at low concentrations, produces a bad smell and converts to highly corrosive, unhealthy, and environmentally hazardous SO_2 and H_2SO_4. In biogas H_2S is mixed with CH_4, CO_2, H_2O and other higher hydrocarbons. With removal of H_2S, the gas stream has greater value as fuel. Biogas purification methods can be divided into two categories: physicochemical phenomena and biological processes. There are number of different techniques that have been developed at the lab scale for removal of H_2S but not many have been successfully commercialized. Commercialized techniques include catalytic conversion, hydrosulfurization and filtration through impregnated activated carbon. Use of activated carbon based catalyst has been widely used for removal of H_2S from natural gas, geothermal wells, digester gas, and municipal sewage treatment facilities[138-141].

Typically, activated carbons impregnated with NaOH or KOH are used in H_2S removal. Initially, the gas stream is washed in scrubbers, which increases the humidity in the gas stream. Then it is passed through the activated carbon vessels. The H_2S quickly reacts with the strong base and is immobilized. The humidity in the gas stream assists in this reaction. The removal capacity of such carbons exceeds 0.14 g-cm^3 of carbon. Recent studies have shown that 3 moles of H_2S are adsorbed per 1 mole of NaOH, which highlights its effectiveness. NaOH shifts the dissociation of H_2S to the right increasing the content of HS^- ions which can be further oxidized

either on adsorbed sulfur or activated carbon surface[142]. This process continues until all the NaOH is exhausted.

Unfortunately, impregnated activated carbons carry certain degree of risk. Due to the exothermic reaction during adsorption on a catalyst, the ignition temperature is lowered, potentially resulting in self-ignition of the carbon bed. In addition to this, the oxidation of H_2S results in elemental S which cannot be removed from carbons by washing with water. Additionally, H_2S oxidation stops once all the catalyst is consumed and the pores of the C are filled with sulfur and sodium or potassium salts. Once the reaction has stopped, the C must be disposed. For these reasons, researchers have recently shifted their focus on unimpreganted activated carbons. Considerable removal capacities for H_2S removal at temperature around 200 °C has been reported in literature but not much has been done for removal at ambient temperatures.

Hedden et al.[143] proposed a simple adsorption/oxidation mechanism for H_2S on virgin carbon. Dissociation of H_2S occurs in the film of adsorbed water at the virgin carbon surface, if the pH of the surface allows it, and then HS^- anions are oxidized by oxygen radicals to elemental sulfur[142]. Since this study others have examined the effect of dry and wet conditions on carbon adsorption. It was been observed that dry conditions lead to low capacity being mainly physical adsorption in the small pores of the carbons. It was reported that wet conditions improve the capacity of carbon by much as 80 times. The amount of water adsorbed should not be greater than 5 percent[143, 144], as the increased amount of water vapors can condense into the small pores, thus reducing the number of pore sites available to HS^- dissociation.

Xiao at el.[138] studied the performance of impregnated catalyst on coal based activated carbon for H_2S oxidation, as well as the influence of relative humidity and oxygen on its

performance. The activated carbon used in the study was a commercial grade product which was impregnated with 6% Na_2CO_3. The results show that these impregnated activated carbon (IAC) preformed much better than unimpregnated carbon (UAC). The H_2S sorption capacities of the UAC and IAC were 6.8 and 11.2 mg-g^1, respectively. The S capacities of the two samples increased when oxidizing atmosphere was introduced into the system, to 140 mg-g^{-1} for UAC and 407 mg-g^{-1} for IAC. Addition of humidity also increased the sulfur capacities for both the samples. Elemental S (and some sulfuric acid) was produced when H_2S was oxidized.

Commercially available impregnated activated carbons were tested for oxidation of H_2S at low concentration in digester gas by Bagreev et al. The results showed H_2S removal capacity was dependent on the concentration of H_2S: The lower the concentration, the higher the capacity of adsorbent. Elevated temperatures (38-60 °C) in the reactor and addition of oxygen had no effect on the performance of the materials[141]. Meeyoo and Trimm found completely different results, when they activated carbon for removal of trace H_2S from a gas stream. Increasing the temperature of the system resulted in decreased amount of H_2S removal, as expected, but the drop in the amount H_2S converted catalytically as temperature increased was not expected. The addition of O_2 leads to the formation of elemental S and condensation of H_2O on the surface of the carbon. Water in the gas stream led to improvement in H_2S removal[140].

Effect of pore structure and surface chemistry of activated carbon was investigated by Bandosz. Three commercially available activated carbons were used in the study: (W) wood based carbon activated by H_3PO_4 and (M) petroleum pitch based carbon activated by KOH. The pH of the carbon has a direct effect on the H_2S adsorption capacity. The pH value of sample W was more basic compared to M and W which were neutral in nature. The results indicated that W had a significantly higher sorption capacity than M and W. It was concluded that presence of basic

groups on the surface lead to the immobilization of H_2S. Also, if more oxygen-contain groups are present the carbon surface is more likely to attract and retain water, which is needed for dissociation of H_2S. There was no clear relationship between pore structure and H_2S uptake[145].

The use of CO_2, O_2, and air for oxidation of carbon was studied by Cariason et al. Carbons of high surface area and high purity were produced by carbonization of saran and activating the resultant char. The activation of the char was carried out using CO_2 at 900 °C, O_2 at 300 °C and air at 425 °C. The study showed the oxidation of H_2S on carbon is a first order reaction. The extent of this catalytic activity can be correlated with the carbon activity for the dissociative chemisorption of oxygen. The concentration of oxygen atoms on the carbon is directly related to the oxidizing gas used during activation. It was concluded that use of oxygen or air leads to more efficient at producing active sites than CO_2[146].

The presence of O_2 functional group is also important in breaking down hydrogen sulfide. Tellefson et al. studied the role of O_2 in the kinetic of H_2S adsorption/oxidation. The experiments were performed for low concentration of H_2S (<3%) over a wide range of temperatures (398-473K) and pressure range of 230-2300 kPa. The results showed that the optimum temperature for high H_2S conversion and low SO_2 production is 448K with an O/H_2S ratio 10.05 times the stoichiometric ratio.

Development of activated carbon for selective oxidation of H_2S was investigated by Bashkova at el[147]. The study focused on characterizing the surface and structural features of various activated carbon and correlating these properties with the catalytic activity of the materials. Activated carbon was modified with urea to introduce nitrogen-containing groups into the carbon, and compared to commercial activated carbon. Catalytically active nitrogen species in the carbon

increased breakthrough time and capacity for H_2S but also catalyzed the formation of SO_2 and COS and the early release of these species into the gas stream. Microporous volume and narrow pore width of the lab-synthesized carbon contributed to its ability to capture the elemental sulfur and SO_2, that was formed and to retain these products for an extended period of time. The high amount of basic groups on the carbon surface was associated with the conversion of COS to sulfur.

Steijns et al.[148] studied the adsorption of H_2S on various adsorbents. The deposition of S at the beginning of the removal process increased the catalytic activity of the carbon. Once the S began to fill the micropores, a rapid decrease in activity occured. It was concluded that the catalytic activity per square meter of total surface area was approximately proportional to the amount of adsorbed S. Note that Ghosh and Tollefson found no evidence to support this claim[149, 150].

The occurrence of micropores on the C surface plays an important role in adsorption. The filling of micropores by elemental sulfur is seen as the limiting factor of activated carbon capacity. Steijns and Mars[151] found that greater sulfur adsorption occurred in carbons with pores between 0.5-1 nm. The small sizes of the pores allowed only S ions can be stored into them. These isolated S radicals are further oxidized to SO_2 and then SO_3, so that sulfuric acid became the most important product produced in the reaction.

The surface chemistry of the C is an important indicator of H_2S adsorption-oxidation capacity. It is well known that the degree of acid dissociation depends on the pH of the system, and dissociation is feasible when pH is greater than the pK of the acid under study. Since H_2S is a weak acid, local pH in the pore system had a significant effect on the efficiency of H_2S dissociation and thus its oxidation to various sulfur species. Studies show that pH in the basic

range promoted the dissociation of H_2S[142, 144, 152, 153]. This results in high concentration of HS^- ions, which were then oxidized to S radicals and polymers having chain or ring like shapes. When pH value was low only physical adsorption could occur, so that pH values of 4.5 or greater were needed for effective removal of H_2S.

The occurrence of iron oxides or metal ions from groups 6-8 had an effect on H_2S adsorption[142]. It was not only reflected in the amount adsorbed, but also in the extent of oxidation. Iron oxide is known to promote formation of SO_2 when the removal process occurs at elevated temperatures or room temperature. Use of biochar derived from sewage sludge was tested as H_2S adsorbents. An exceptionally high adsorption capacity was found, higher than that of coconut based biochar. The adsorption capacity was attributed to the presence of iron, copper, and zinc oxides on the surface.

7.1.2 Catalyst

Two main commercial catalytic processes dealing with selective oxidation of H_2S by oxygen into elemental S^0 have been developed. The high temperature Superclaus process, which is based on Fe and Fe/Cr catalyst supported on alumina and silica, worked above the S dew point (>180 °C) with an overall sulfur removal efficiency of 99.5%[5, 154-158]. The lower temperature (100 °C) Doxosulfreen process was based on Cu catalyst supported on modified alumina in batch mode reaches efficiencies of 99.9%[158-160]. These processes were generally used as S recovery processes rather than H_2S removal technologies. Also, although these process are efficient they are only economical for large scale production due to large capital requirements and complex expensive procedures. Furthermore, the addition of oxygen in gas stream containing methane can be highly dangerous.

$$3H_2S + SO_2 \xrightarrow{yields} 2H_2S + SO_2 + H_2O \quad (26)$$

$$2H_2S + SO_2 \xrightarrow{yields} \frac{3}{n}S_n + H_2O \quad (27)$$

The use of adsorbents for H_2S adsorption has been identified as a sound means to purify small-scale biogas production. These types of systems involve fixed-bed upward or downward flow gas-solid contactors. This use of catalysts for H_2S decomposition is of much interest as it is less energy intensive and more economically feasible. Many metal oxides including iron, zinc, calcium, molybdenum, copper and cobalt have been identified as suitable adsorbents for H_2S removal[5, 161]. Nonetheless, only iron, zinc and calcium oxides are extensively used for H_2S due to cost and availability. In this study, we focus our attention on iron oxide, one of the oldest metal oxide implemented since the 19th century[5, 162, 163].

The iron sponge is the best known iron oxide adsorbent. In most iron sponge applications, the iron oxide is impregnated onto wood-chips for selective adsorption of H_2S. The chemical reactions involved are shown in the following equations:

$$Fe_2O_3 + 3H_2S \xrightarrow{yields} Fe_2S_3 + 3H_2O, \quad (28)$$

$$Fe_2S_3 + \frac{3}{2}O_2 \xrightarrow{yields} Fe_2O_3 + 3S. \quad (29)$$

The iron sponge has been shown to work in both batch mode and continuous-regeneration mode. In batch mode, 85% efficiency (0.56 gHgS) of theoretical efficiency has been achieved. Soon after complete saturation, the vessel is taken out of service for regeneration. Due to S^o build-up and

loss of hydration water, iron-sponge activity is reduced by about one-third after each regeneration cycle. On the other hand, a continuous-regeneration process has a higher removal capacity of 1.84 gHgS[5].

Kotera[164] and Fukuda[165] studied catalytic activity of metal sulfides including FeS, and NiS at temperatures of 500-800 °C. FeS and NiS were able to react with H_2S according to the following reactions:

$$FeS + H_2S \xrightarrow{yields} FeS_2 + H_2, \quad (30)$$

$$NiS + H_2S \xrightarrow{yields} NiS_2 + H_2. \quad (31)$$

Al-Shamma[166, 167] studied the decomposition of H_2S on $V_2O_5/\gamma\text{-}Al_2O_3$ at 500-600 °C and proposed a two-stage process in which S^o is produced. The reaction of H_2S on vanadium oxide was proposed as:

$$5H_2S + V_2O_5 \xrightarrow{yields} V_2S_3 + 5H_2O + 2S^O. \quad (32)$$

The V_2S_3 provided additional reaction site for decompose of H_2S via following reactions:

$$V_2S_3 + 5H_2S \xrightarrow{yields} VS_4 + 5H_2, \quad (33)$$

$$2VS_4 \xrightarrow{yields} V_2S_3 + 5S^O, \quad (34)$$

$$H_2S \xrightarrow{yields} H_2 + S^O, \quad (35)$$

Unfortunately these catalysts are expensive or hazardous and require high operation temperatures.

In this study, we look at the potential of untreated biochar and metal catalyst to adsorb H_2S and CO_2 from a biogas stream. To achieve this goal, detailed studies of biochar were performed and the adsorption capacities are measured. These data were used to evaluate the effectiveness of biochar as a filtration media for biogas. In doing so, we increased the value of biogas, and prevented CO_2 from returning to the atmosphere. We also report the use of a metal oxide catalyst for removal of H_2S from the biogas stream. With this process, it was possible to carry out H_2S adsorption for an extended period of time at relatively low temperatures of 23-255 °C.

7.2 Experiment

7.2.1 Materials

Four sets of biochar pellets were used in this study. Set-1 was derived from hardwood ($BC\text{-}1_o$), set-2 was blend of chicken waste plus hardwood ($BC\text{-}2_o$), set-3 was switchgrass ($BC\text{-}3_o$), and set-4 blend of swine waste plus rye ($BC\text{-}4_o$). The biochar samples are donated by United States Department of Agriculture (USDA) and North Carolina University. The samples were oxidized under CO_2 atmosphere at 900 °C for 60 minutes. The oxidized samples were labeled as BC-1, BC-2, BC-3 and BC-4.

Nano-iron oxide catalyst was sonochemically prepared by decomposing $Fe(CO)_5$ in hexadecane. Two sets of nano-iron oxide catalyst samples were prepared and are referred to as HD-3, and HD-2. The BET surface area of HD-3 was 53.17 m^2g^{-1} and HD-2 was 16.48 m^2g^{-1}. Commercially available cupric oxide (CO), nickel oxide (NO), and iron oxide (FO) catalysts were purchased form United Catalysts Inc. These metal oxides were chosen due to their lower bond enthalpy thus requiring less energy for regeneration. This allowed for easier regeneration of the

product, when needed. Spectroscopic studies of the reacted and unreacted catalyst were carried out on a Perkin Elmer Frontier FTIR spectrometer.

A synthetic mix of CH_4 (59%), CO_2 (40%), and H_2S (1%) was provided by Air Liquid. All reactions were carried out under a fume hood due to dangerous nature of biogas. The gaseous products were analyzed by a gas chromatograph (Gow-Mac series 580) with a Hayesep R colume (4' X 1/8") and a flame photometric detector (FPD).

7.2.2 Gas Breakthrough Capacity

For the reaction test, the adsorbent was loaded into a quartz reactor measuring 0.63 cm o.d x 16.5 cm length. Breakthrough capacity of synthetic biogas was tested as it passed through packed column (Figure 2.2). The experiment was carried out until 500 ppm of H_2S was recorded at the outlet. The bed temperature was measured by a K-type thermocouple placed at the center of the packed bed. The vertical reactor was wrapped with electric heating tape equipped with a temperature controller and operated isothermally.

Biochar particulates of size 40 x 60 (using U.S. Standard Mesh sieve) were loaded into the reactor chamber and were held in place with quartz wool. The packed d measured 14 cm in length. Effects of environmental temperature and surface chemistry (pH) of the biochar were studied. Landfill gas is known to be produced at elevated temperatures of 70 – 100 °C. To simulate this condition, the biochar column was heated between 70 – 100 °C as the biogas was passed through the column. All experiments are conducted in the absence of water unless stated otherwise. The experiments were conducted at atmospheric pressure with gas hourly space velocity (GHSV) of 275 hr^{-1}. The weight of the biochar samples ranged from 0.6 – 1.8 g.

The catalyst was held in place in the center for the reactor measuring only 2.28 cm in length with quartz wool. The experiments were conducted at atmospheric pressure with gas hourly space velocity (GHSV) of 1690 hr^{-1}. The weight of the samples range from 0.2 – 2.0 g. The adsorption capacity of the adsorbents were calculated using the following equation:

$$\frac{X_b \; x \; C_{H_2S} \; x \; M_b \; x \; P}{W_c}, \tag{36}$$

where X_b is biogas collected in moles, C_{H_2S} is concentration of H_2S in percentage (1%), M_b is molar mass of biogas (94.13 g mol^{-1}), P is efficiency percentage, and W_c is total weight of the sample.

Composition	ΔH_f (kcal $mole^{-1}$)	ΔG_f (kcal $mole^{-1}$)
FeS	-24.2	-24.3
NiS	-20.3	-20.6
CuS	-11.6	-11.7
ZnS	-49.2	-48.1

Table 7.1: *Standard enthalpy and Gibbs free energy of formation of sulfide minerals form the elements at 25°C*[168].

7.2.3 pH of Biochar Surface

The pH measurements of the biochar were conducted according to ASTM D3838. Ten grams of biochar was added to 100ml of DI water. The mixture was boiled for 15 minutes. The water was filtered and the pH was measured.

7.2.4 N_2 Adsorption

BET surface area and micropore volume distribution were determined using N_2 adsorption using a Micromeritics TriStar 3000 analyzer. Before the experiment the sample was degassed for four hours at 350 °C under constant helium flow. The total BET surface area was calculated using:

$$Total\ BET\ Area = Micropore\ Area + Exteral\ Area \quad (37)$$

7.2.5 Thermal Regeneration

Regeneration experiments were also performed. Thermal regeneration of biochar was carried out by heating the sample to 300°C for five hours under 200 ml min^{-1} flow of N_2 in a Lindebery Blue M tube furnace. The temperature was carefully monitored and the gas flow rate was measured by calibrated rotameter. The regeneration of the catalyst was carried out at 420°C in the tube furnace. The regeneration feed gas contained H_2O and air, where the air was bubbled through a water column at 200 ml min^{-1}. The regeneration process for the metal oxide catalyst was carried out for 12 hours. Upon regeneration, the samples were retested for H_2S removal.

7.3 Results and discussions

7.3.1 Biochar

Activated biochar was tested as an H_2S adsorbent using the breakthrough capacity measurements. The H_2S breakthrough capacity was expressed in terms of mHgS. The importance of surface area, pore volume and surface chemistry should be noted when comparing H_2S capacity of each sample. The hardwood based sample (BC-1) outperformed other samples as H_2S adsorbents. Activated carbons derived from wood based feedstock have shown to preform significantly better as a H_2S adsorbent than activated carbons produced from other feedstocks[144]. Commercially available activated carbon tested in this study showed the lowest affinity for H_2S

adsorption. The H_2S breakthrough capacity was calculated by integration of the area above the H_2S breakthrough curve, taking into account the initial and exit concentration of H_2S, the flow rate, breakthrough time, and mass of the carbon. The breakthrough time used to calculate the H_2S capacity was defined as the lapsed time from the beginning of the experiment to the time outlet concentration of H_2S was 500 ppm.

7.3.1.1 Activated Biochar Characterization

The N_2 adsorption data and surface chemistry (pH) were obtained for all five samples examined in this work. The N_2 adsorption isotherms are given in Figure 7.1. The BET surface area, micropore surface area, external surface area and micropore volume of each sample are shown in Table 7.2. The isotherms of all five samples are typical of Type I (according to the IUPAC classifications), which indicated the existence of narrow micropores in the samples. The quantity of N_2 adsorbed before plateauing ($p/p^o < 0.05$) indicated the size of the microporous area and volume present in the sample. The plateauing at $p/p^o > 0.05$ indicated the filling of micropores and beginning of adsorption on the external surface at a very slow rate. This was expected as most microporous materials are characterized as Type I isotherms.

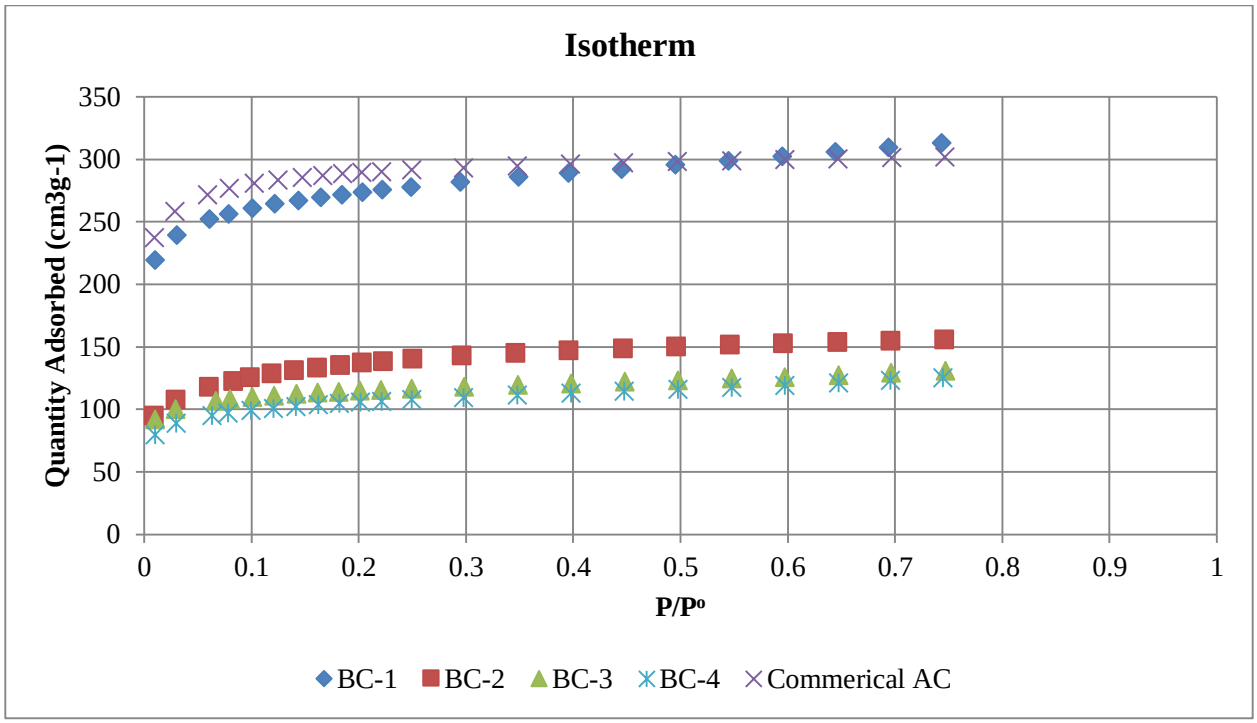

Figure 7.1: *Type I N_2 adsorption isotherm measured at -198 °C for BC-1, BC-2, BC-3, BC-4, and commercial AC.*

On average the activated biochars showed significantly lower surface area and pore volume than commercial AC as seen in Table 7.2. The commercial AC showed the largest surface area at 1100 m^2g^{-1}. The largest surface area in the biochar sample was produced in BC-1 at 1026 m^2g^{-1} and the surface area measured for BC-2 (506 m^2g^{-1}) > BC-3 (433 m^2g^{-1}) > BC-4 (394 m^2g^{-1}). Meanwhile, micropore volume ranged from 0.12 cm^3g^{-1} in BC-4 to 0.40 cm^3g^{-1} in the commercial AC. Of the biochar samples, BC-1 showed the maximum micropore volume at 0.33 cm^3g^{-1}. The relationship between surface area and micropore volume is clearly shown in Figure 7.2a. A linear regression analysis for the BET surface area found $R^2 > 0.98$. The relationship between micropore surface area and micropore volume was strongly linked to each other as seen in Figure 5.3b, with $R^2 > 0.99$. Larger micropore surface area led to higher micropore volume, as expected. The role of biochar pore volume in H_2S adsorption cannot be overlooked. Bashkova at el. showed that

carbons with smaller surface area but with larger pore volume had higher H_2S adsorption capacity[169].

Sample	Total BET Area (m^2g^{-1})	Micropore Area (m^2g^{-1})	External Area (m^2g^{-1})	Micropore Volume† (cm^3g^1)	pH
BC-1	1026	805	221	0.33	11.35
BC-2	506	335	171	0.14	10.99
BC-3	433	348	85	0.14	12.00
BC-4	394	287	107	0.12	10.64
Commercial AC	1100	984	116	0.40	9.43

Table 7.2: *Total BET surface area and micropore volume data was obtained from N_2 adsorption testing along with pH values of the samples. †Micropore volume (rounded up to the hundredth decimal point)*

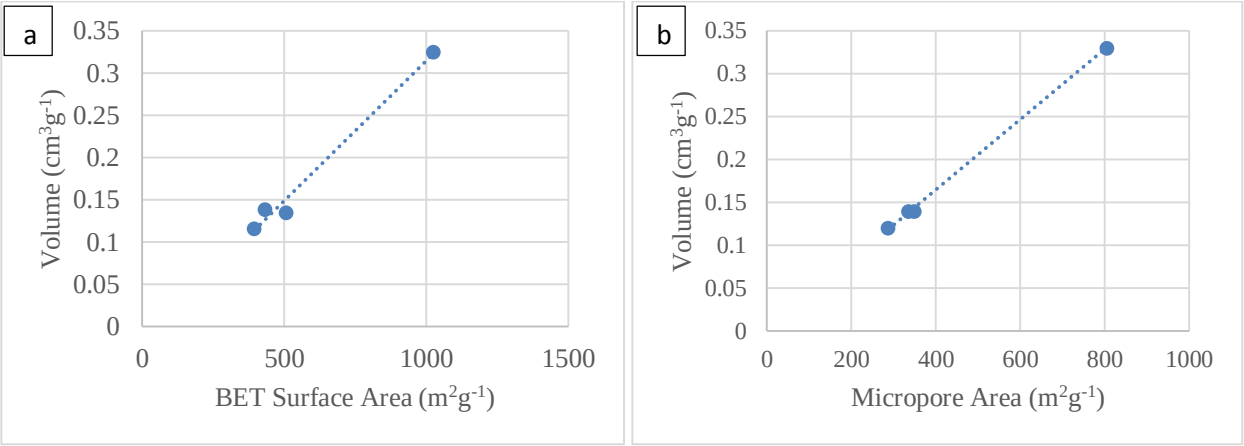

Figure 7.2: *A strong linear relationship between (a) BET surface area vs. volume, and (b) micropore area vs. volume was established from the data in Table 5.2.*

The surface pH of the biochar is given in Table 7.2. All biochar samples show a pH value of >10. Sample BC-3 was the most basic of the samples studied at pH of 12. The commercial AC was surprisingly in the basic range of the pH scale, though it was still relatively lower then biochar samples.

7.3.1.2 Catalytic activity measurements

Differences in performance have been linked to number of different factors including surface area, pore volume and surface pH of the sample. An H_2S adsorption test were performed before and after oxidization of the biochar, in order to study the effects of surface area and pore volume on adsorption capacity. The adsorption test was carried out at 100°C to simulate actual biogas conditions. The BET surface areas of all the biochar samples were <0.5 m^2g^{-1} before oxidation. The lack of surface area was not suitable for H_2S adsorption, as indicated by the results in Table 7.3. The removal capacity of BC-1_0 (6.2 mHgS) > BC-4_0 (5.8 mHgS) > BC-3_0 (5.7 mHgS) > BC-2_0 (4.5 mHgS) at 100 °C.

Sample	**at 100°C (mHgS)**	**Sample**	**at 100°C (mHgS)**
BC-1_0	6.2	BC-1	59.4
BC-2_0	4.5	BC-2	38.1
BC-3_0	5.7	BC-3	47.4
BC-4_0	5.8	BC-4	36.4

Table 7.3: *Comparison of H_2S adsorption capacity between pre-activated (left-hand side) and post-activated (right-hand side) biochar samples.*

The activated biochar samples were tested for H_2S adsorption at 100°C. The H_2S adsorption capacities showed a large improvement (Table 7.3). The biochar samples showed an expansion in adsorption capacity by >88%. Sample BC-1 was the best performing biochar sample with 59.4 mHgS at 100 °C followed by BC-3 (47.4 mHgS), BC-2 (38.1 mHgS), and BC-4 (36.4 mHgS).

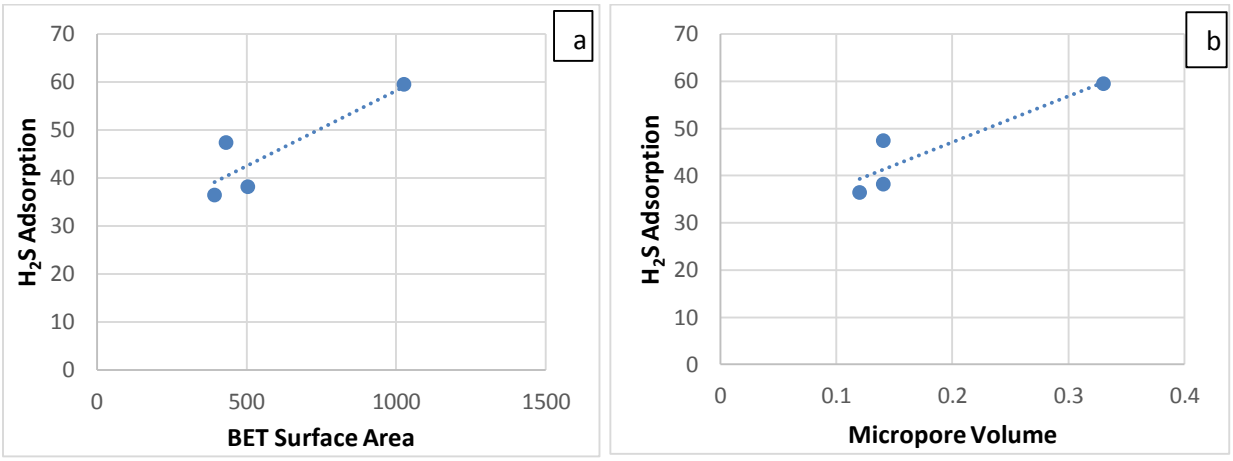

Figure 7.3: *Measure of adsorption capacity at 100 °C as depended on biochar (a) BET surface area and (b) micropore volume.*

The importance of micropore volume was highlighted by the results given in Figure 7.3. Comparing the results from sample BC-2 and sample BC-3 showed that micropore volume was important in terms of H_2S adsorption capacity. The total BET surface area of BC-2 (506 m^2g^{-1}) was greater than BC-3 (433 m^2g^{-1}), but the micropore surface area, which was directly linked to micropore volume (see Figure 5.3b), of BC-3 (348 m^2g^{-1}) was greater than BC-2 (335 m^2g^{-1}), and resulted in a 20% higher adsorption capacity. Linear regression analysis shows a R^2>0.83 when comparing micropore volume to H_2S adsorption (see Figure 7.3b). The same analysis applied to surface area and H_2S adsorption showed R^2>0.76 (see Figure 7.3a). This indicates micropore volume is a better indicator of H_2S adsorption capacity in biochar.

To observe the effects of gas temperature on H_2S adsorption the samples were heated to 23 °C and 100°C. All three component of the gas stream, CH_4, CO_2, and H_2S were carefully monitored at the outlet. Interactions of CO_2 and CH_4 with the biochar surface have been well documented[17, 18, 170]. At 23°C the results showed that CH_4 has limited interaction with the biochar surface as CH_4 was immediate observed at the outlet of the reactor (Figure 7.4a). Meanwhile, CO_2 breakthrough was dependent on the experimental temperature. At 23°C physical adsorption of CO_2 and H_2S was observed to take place in all four samples. The average breakthrough time for CO_2 was 20 mins, while breakthrough time of H_2S varied from sample to sample. The reaction in which CO_2 and H_2S are physically adsorbed onto the surface:

$$H_2S_g \rightarrow H_2S_a, \tag{38}$$

$$CO_{2g} \rightarrow CO_{2a}. \tag{39}$$

In this case, competitive adsorption took place between CO_2 and H_2S for the limited number of sites available for adsorption. For instance, an adsorbed CO_2 molecule on the biochar surface could be displaced by an incoming H_2S molecule with a greater binding energy, and vice versa. The discriminatory nature in which the biochar surface preferred one molecule over the other, was determined by van der Waals intermolecular interactions. Van der Waals forces play an important role in physical adsorption of gases onto carbon surfaces at low temperatures. In general, the binding energy of the adsorbate to the adsorbent allowed the surface to be selective in adsorption. Typical binding energy for physical adsorption was approximately 10-100 meV.

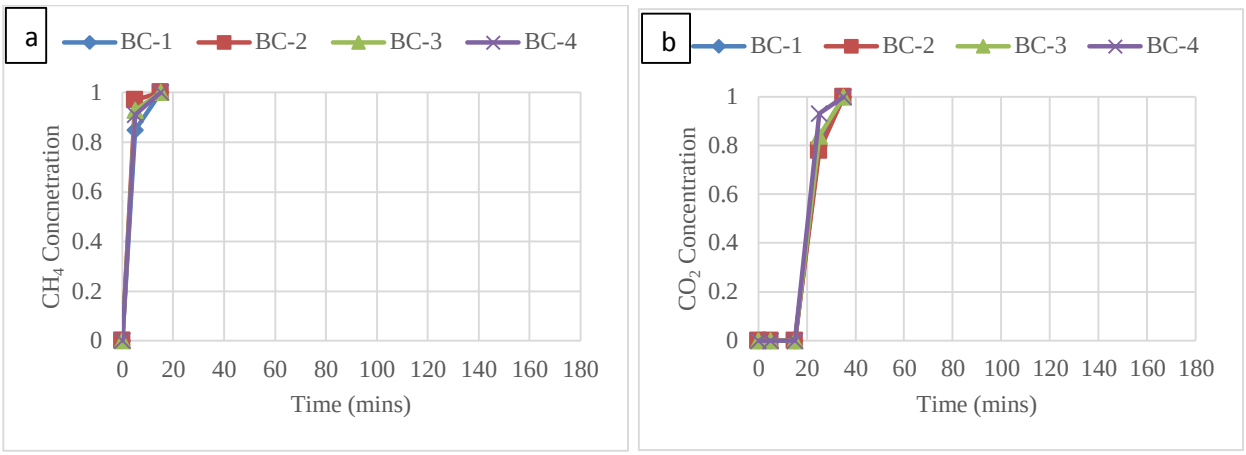

Figure 7.4: *Concentration of (a) CH_4 and (b) CO_2 at the outlet as biogas flows through the sample tube at 25 °C.*

The data clearly showed that samples BC-1, BC-2, and BC-4 were selective in adsorbing H_2S over CO_2. Sample BC-3 was less selective and displayed equal breakthrough time for both CO_2 and H_2S. Sample BC-2 had the longest breakthrough time for H_2S removal while sample BC-3 had the shortest. Although BC-2 had longer breakthrough time, sample BC-1 removed the largest amount of H_2S at 96.9 mHgS, while sample BC-3 had the least at 34.8 mHgS. Sample BC-1 and sample BC-3 were 100% efficient in removing H_2S until time of breakthrough (Figure 7.5). Sample BC-2 and BC-4 had removal efficiency of 99% and 98% respectively. The sharp breakthrough curves indicate near complete usage of the biochar surface in all four samples.

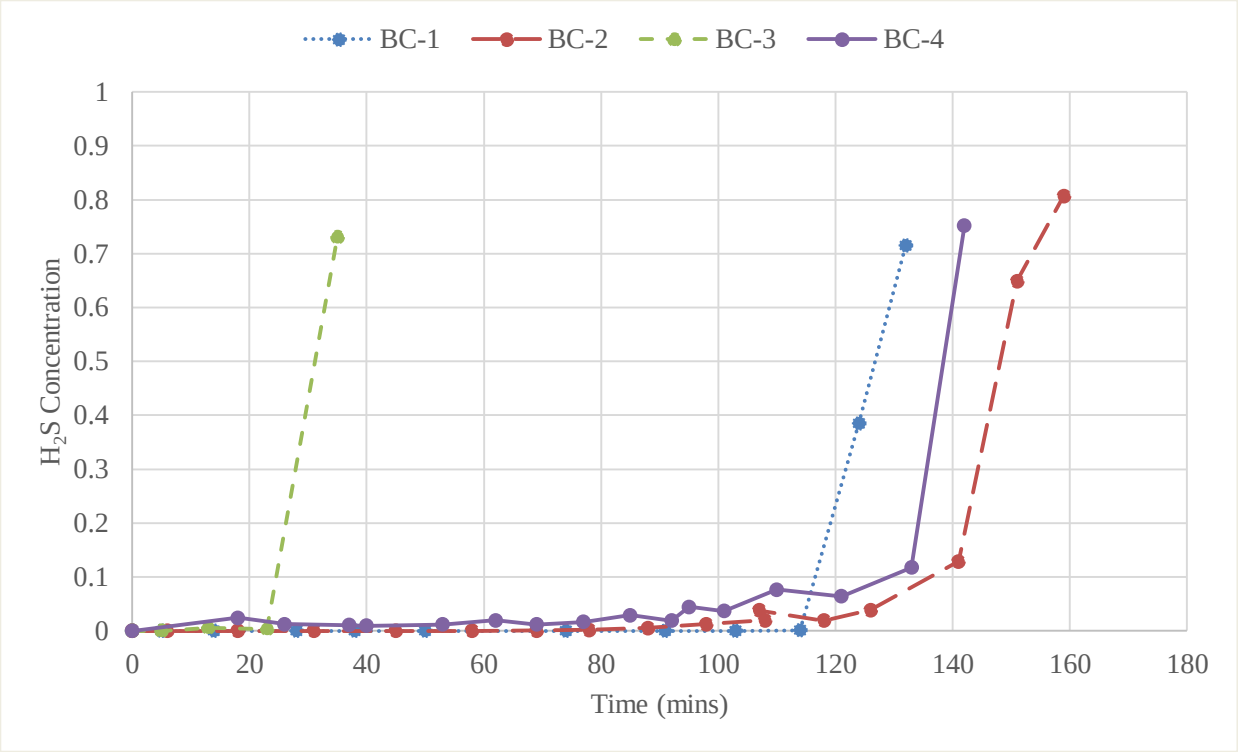

Figure 7.5: *Breakthrough curves of biochar samples taken at 23 °C.*

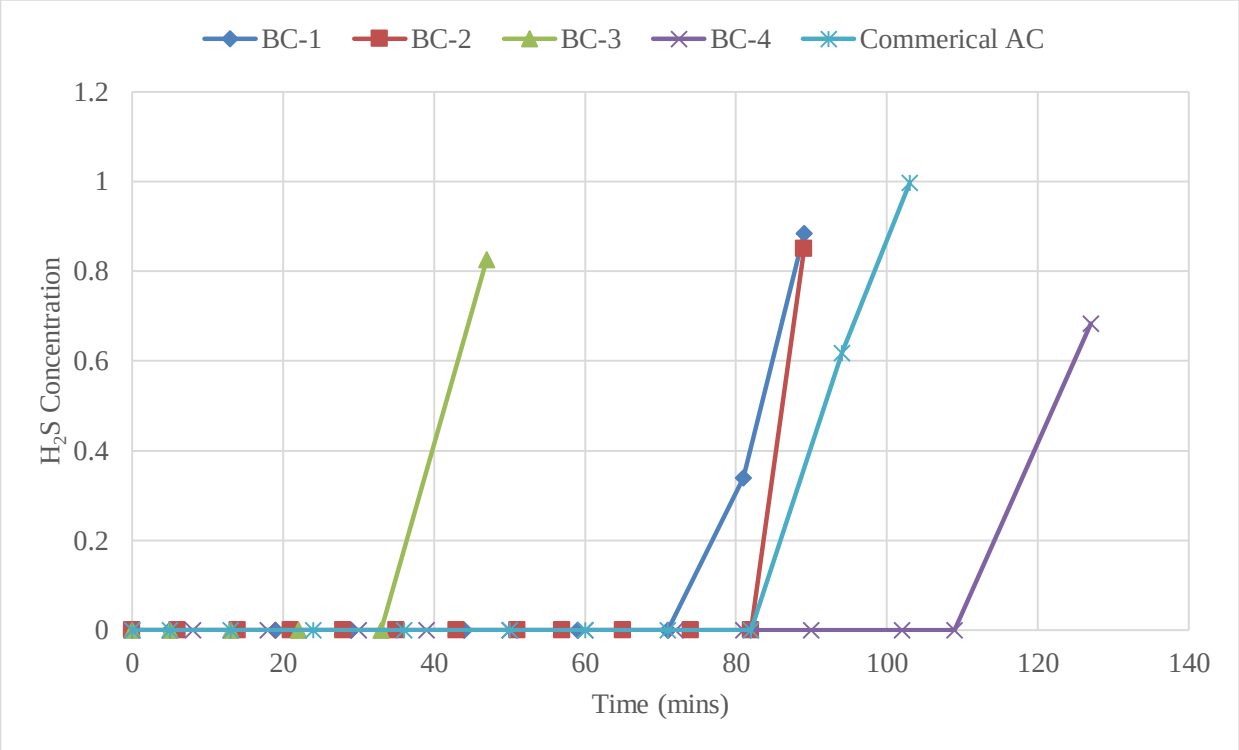

Figure 7.6: *Breakthrough curves of biochar samples when run at 100 °C.*

At 100°C, both CH_4 and CO_2 showed no interaction with the biochar surface of any of the samples. Both gases passed through the packed bed column without interacting with the biochar as expected. At elevated temperatures, the CO_2 molecules are at higher energetic state, and adsorption-desorption occurs simultaneously. These energetic molecules leave the biochar surface without much interaction. These data show that interaction between CO_2 and the biochar surface was strictly physisorption. Sample BC-4 had the longest breakthrough time while BC-3 had the shortest. Sample BC-1 removed the largest amount of H_2S at 59.4 mHsg and the commercial sample had the least removal at 32.6 mHgS. The removal efficiency was 100% in all five samples.

Sample BC-1 had 38% increase in H_2S adsorption capacity and sample BC-2 increased by 34% at 23°C. Sample BC-3 had 27% decrease in adsorption capacity. These results show that BC-1, BC-2, and BC-4 prefer physisorption for removing H_2S, while BC-3 prefers chemisorption mechanism. The data also indicates that the samples were complete saturated before breakthrough. The activated biochar samples were able to outperform the commercial AC at 100°C.

Sample	at 23°C (mHgS)	at 100°C (mHgS)
BC-1	96.9	59.4
BC-2	57.2	38.1
BC-3	34.8	47.4
BC-4	49.7	36.4
Commercial AC	-	32.6

Table 7.4: *Recorded breakthrough capacity of H_2S at 100°C and 23°C for all different samples. BC-1 and BC-2 perform better at low temperatures indicating large amount of physical adsorption taking place.*

7.3.1.3 Importance of surface pH

In most instances surface chemistry of the carbon is rarely considered when deciding which carbon to use for adsorption. Few studies have highlighted the importance of surface chemistry when it comes to adsorption of H_2S. It is known that degree of acid dissociation depends on the pH of the system. Hydrogen sulfide is a well-known weak diprotic acid with first and second dissociations constant (K_a) equal to 1.0×10^{-7} and 1.3×10^{-13} respectively. These values can be different in the small pores of activated carbon where the effect of the enhanced adsorption potential is very strong.

A low pH value of the carbon surface was expected to suppress the dissociation of H_2S. This resulted in low concentration of HS^- ions in the pores which were oxidized to sulfur oxide from which sulfuric acid formed. On the other hand, a pH in the basic range supported the dissociation of H_2S. This resulted in a high concentration of HS^- ions, which were then oxidized to sulfur polymers having chain or ring-link shapes[56]. The local pH value depended on the pore sizes and the location of acidic groups. Pores need to be large enough to accommodate surface functional groups and small enough to have a film of water at relatively low pressure[171]. This played an important role in the oxidation-adsorption reactions which took place on the surface of the biochar.

Sample	pH	@ 100°C (mHgS)
BC-1	11.35	59.4
BC-1	10.19	47.6

Table 7.5: *Change in surface pH has a drastic effect on the H_2S adsorption capacity.*

The effect of surface pH on the H_2S adsorption capacity was studied by modifying the surface chemistry of the biochar sample. These experiments were carried out at 100°C using sample BC-1. The initial surface pH of sample BC-1 was 11.35 (run 1). When H_2S adsorption test was carried the result showed a breakthrough time of 71 minutes before 500 ppm of H_2S was detected at the outlet. This was equivalent to 59.4 mHgS. A modified BC-1 sample (run 2) with surface pH of 10.19 was tested. The surface pH modification was done by washing the sample with deionized water for three hours and drying it in the oven. Change in surface pH caused the breakthrough time to decrease to 57 minutes, equivalent to 47.6 mHgS. Decreased surface pH had a negative impact on adsorption capacity. Lower pH value indicates loss of basic functional groups from the surface. These functional groups are known to be active sites for H_2S decomposition[59]. A lack of these basic functional group led to lower adsorption capacity.

7.3.1.4 Presence of water

The presence of water on the carbon surface and its ability to oxidize H_2S has been studied extensively[56]. The presence of water contributes to the dissociation of H_2S and facilitates its oxidation to sulfur and sulfur dioxide. The proposed mechanism in which H_2S dissociates in water goes as following[138]:

$$H_2S_g \overset{K_H}{\rightarrow} H_2S_a, \tag{40}$$

$$H_2S_a \overset{K_s}{\rightarrow} H_2S_{a-l}, \tag{41}$$

$$H_2S_{a-l} \overset{K_a}{\rightarrow} HS_a^- + H^+, \tag{42}$$

$$HS_a^- + O_a^* \overset{K_{R1}}{\longrightarrow} S_a + OH^-, \tag{43}$$

$$HS_a^- + 3O_a^* \xrightarrow{K_{R2}} SO_{2a} + OH^-, \quad (44)$$

$$SO_{2a} + O_a^* + H_2O_a \xrightarrow{K_{R3}} H_2SO_{4a}, \quad (45)$$

$$H^+ + OH^- \xrightarrow{yields} H_2O, \quad (46)$$

where g is gas, l is liquid and a is adsorbed phase; K_H, K_S, K_a, K_{R1}, K_{R2}, and K_{R3} are equilibrium constants for related reactions that which are occurring; O^*_a is dissociatively adsorbed oxygen. In this study, presence of water on the biochar showed no improvement in H_2S adsorption capacity. The H_2S adsorption capacity was lowered by nearly half in the presence of water in the gas stream. The occurrence of water in the gas stream lead to rapid deactivation of the carbon, as the larger water molecules settled onto the carbon surface thus blocking the pore entrance. In addition, reactions between H_2S and water led to an increased amount of sulfuric acid as observed by the decrease in pH value of the exhausted carbon. Formation of sulfuric acid makes it more difficult to regenerate the biochar for additional use.

Precipitation of water molecules was observed near the outlet of the glass column, indicating the oxidation of H_2S as follows:

$$H_2S + \frac{1}{2}O_2 \xrightarrow{yields} H_2O + S. \quad (47)$$

This reaction is well known and has been observed previously[172, 173]. An increase in weight of the carbon samples was observed after each reaction. This weight gain was not purely physisorption a phenomenon as it is unlikely for physical adsorption to take place at elevated temperatures. It is

suspected that H_2S oxidation contributed the largest portion of the weight gain, along with chemisorption. The surface pH of the samples did not decrease in value but rather increased, indicating the oxidation reaction being favored over chemisorption, where sulfuric acid was regularly formed. Physical observation of elemental sulfur was not possible on the outer surface of the biochar. It is more likely that sulfur particles were present deep within the micropores of the samples as this is where majority of reaction sites were available.

7.3.2 Metal Oxide Catalyst for H_2S removal

A metal oxide catalyst allow decomposition of H_2S at both low (<200°C) and high temperatures (>300 °C). Low temperature decomposition of H_2S would be of great practical value. The H_2S removal at low temperatures mainly occurred due to gas-solid reactions. The process led to sulfide formation and deactivation of the catalyst. A goal of the research was to prevent the premature deactivation of the catalyst and prolong the catalyst lifespan.

Sample	Total Capacity (gHgS)			
	23°C	110°C	210°C	255°C
HD-2	<0.01	0.03	1.67	0.48
HD-3	<0.01	0.27	2.87	3.38
CO	<0.01	0.04	1.76	0.73
NO	0.00	0.00	0.00	0.00
FO	<0.01	0.00	1.04	0.64

Table 7.6: *The total capacity of unused catalyst is calculated based on H_2S concentration at the outlet staying below 500 ppm during the duration of the experiment.*

The desulfurization activity of the metal oxide samples as a function of reaction temperature (23 °C, 110 °C, 210 °C, and 255 °C) are given in Table 7.6. Increasing reaction

temperatures (up to 210 °C) caused the H_2S adsorption capacity increase, after which adsorption capacity began to decrease (except in HD-3 sample). The lab-synthesized catalyst HD-2 and HD-3 had largest H_2S adsorption capacity, for these catalysts. Sample HD-3 showed the highest overall removal capacity of 3.38 gHgS at 255 °C. An operating temperature of 210 °C was optimal for obtaining maximum adsorption capacity in CO (1.76 gHgS), HD-2 (1.67 gHgS), and FO (1.04 gHgS) samples. Surprisingly, sample NO was nonreactive with H_2S at any temperature. The catalytic activity of all samples was limited at low temperatures (≤110 °C). At 23 °C the metal oxide samples were ineffective at removing H_2S. Decomposition of H_2S on metal oxides is an endothermic reaction therefore energy input is required for the reaction to take place. Thus, the H_2S flowed through the packed-bed without reacting. In all five cases, H_2S breakthrough occurred between 15-19 mins from the start of the experiment.

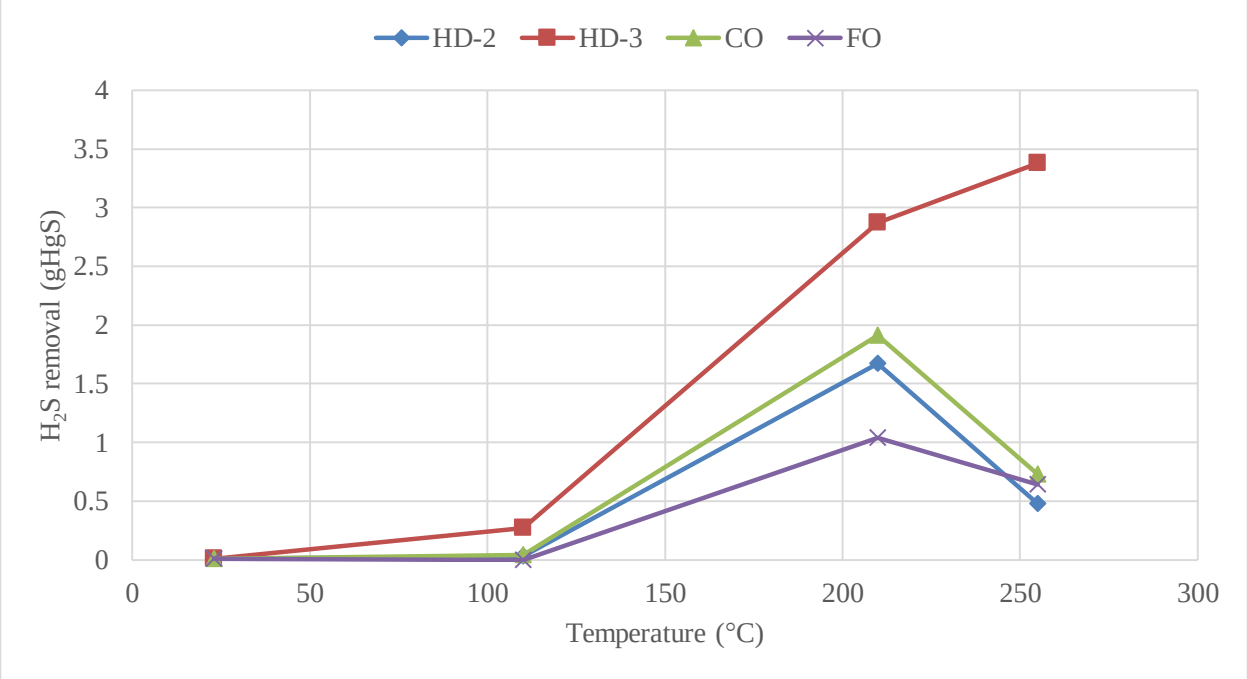

Figure 7.7: *Graphic representation of H_2S removal by HD-2, HD-3, CO, and FO samples and their R^2 values.*

The relationship between temperature and H_2S removal is clearly shown in Figure 7.7. A linear regression analysis of the data showed $R^2 > 0.91$ in the case of HD-3. Coefficient values $0.37 < R^2 < 0.66$ for samples HD-2, CO, and FO were found. Drop off in H_2S adsorption capacity at 255 °C was observed in HD-2, CO, and FO, while an increase in adsorption was found for HD-3. High temperature decomposition was not favored in HD-2, CO and FO samples. At 255°C HD-2, CO, and FO samples rapidly dehydrated causing the individual particles to congeal together. The congealing of the particles reduced valuable surface area needed for H_2S decomposition. The physical changes in the samples after reaction were described in preceding sections.

7.3.2.1 HD-2 and HD-3

Setting the reaction temperature to 110°C did not yield much improvement in H_2S decomposition. A H_2S concentration of 1136 ppm was observed at the outlet within 40 minutes of the experiment when working with HD-2. With sample HD-3, it took 64 minutes before H_2S breakthrough occurred. This was reflected in the larger H_2S adsorption value of 0.27 gHgS for HD-3 compared to 0.03 gHgS for HD-2. At 110 °C, the reactor bed was rapidly saturated and the catalyst was deactivated. As expected, H_2O molecules were observed at the outlet of the reactor as H_2S decomposed on the surface of HD-3 and HD-2. Visual examination of the spent-catalyst showed a change in color for HD-2 (red-brown to black) and HD-3 (brown to black) near the inlet of the reactor column. The outlet and middle region of the reaction column lacked any color change demonstrating unreacted Fe_2O_3 was still present in the column. The change in color indicated the transformation of $Fe_2O_3 \rightarrow Fe_xS_y$. FTIR spectra of the black compound confirmed the existence of Fe_xS_y (see Figure 7.8a). The broad bands at 3400-3100 cm^{-1} were allocated to O-H stretching mode and 1623 cm^{-1} to O-H bending, associated with surface H_2O molecules. Peaks from 1100-950 cm^{-1} were possibly Fe-S skeletal vibration[174]. The 680-390 cm^{-1} bands were

assigned to Fe-O stretching and bending mode. The FTIR spectra of unreacted HD-3 sample is clearly seen in Figure 5.9b.

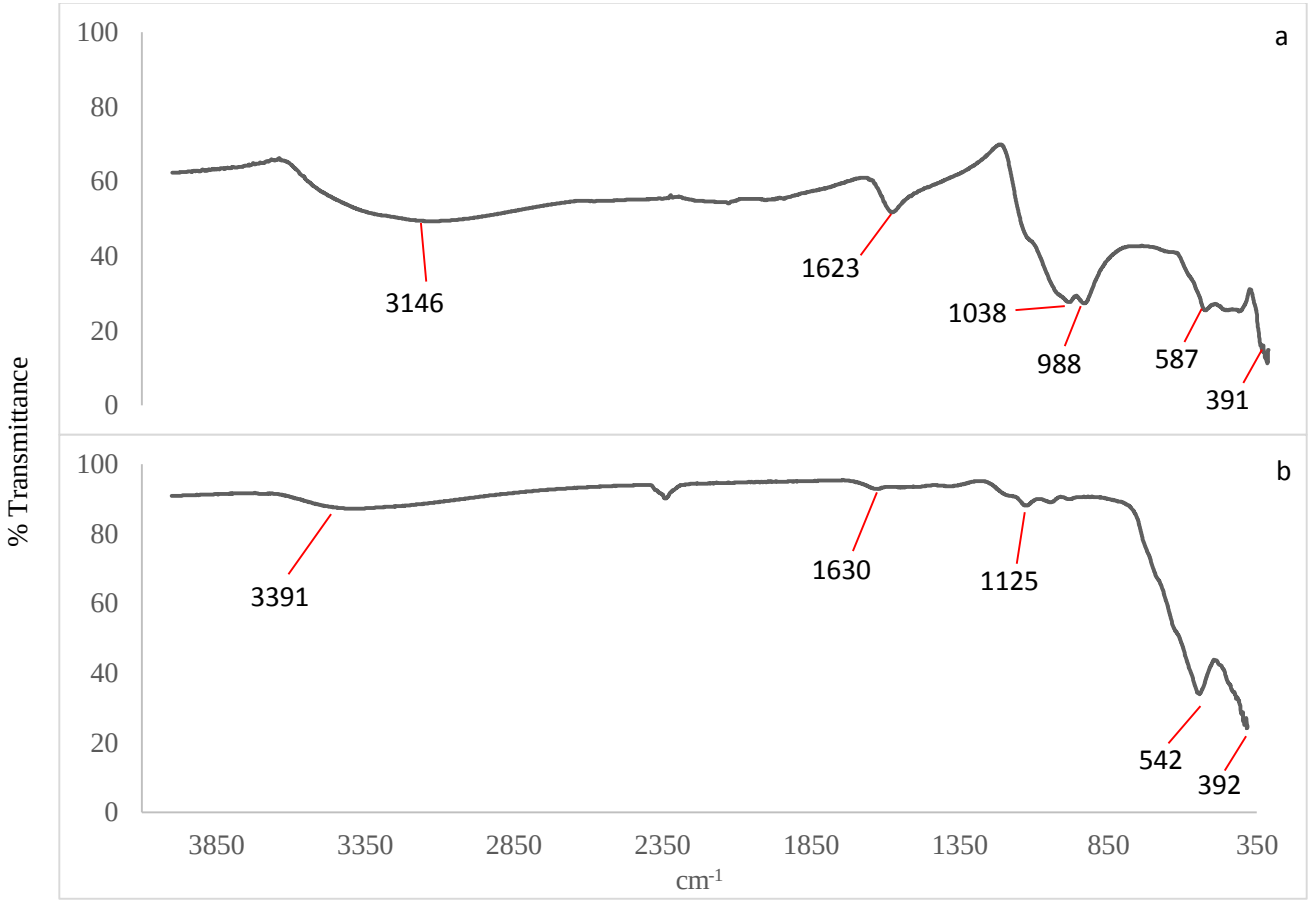

Figure 7.8: *FTIR spectra of sample HD-3 after reacting with H_2S at 110 °C at the (a) beginning of the reactor bed and (b) end of the reactor bed.*

H_2S decomposition at high temperatures yielded better results. At 210°C, H_2S decomposition was 100% efficient for over 21 hours for HD-3 and 33 hours for HD-3, before H_2S breakthrough was observed. During the initial stages of the experiment, an accumulation of H_2O molecules was observed at the outlet of the reactor bed. After an hour, the H_2O molecules gave way to a bright yellow compound on the outlet of the reactor as seen in Figure 5.10. Chemical analysis via FTIR of the yellow compound confirmed the formation of elemental S^0. Presence of

strong IR bands at 864, 656, and 464 cm^{-1} was consistent with that of elemental sulfur (Figure 7.10). The S^0 accumulation was constant for the entire duration of the experiment for both HD-2 and HD-3 samples. The HD-3 sample showed a S^0 amount precipitated at a ratio of 2:1 compared to HD-2.

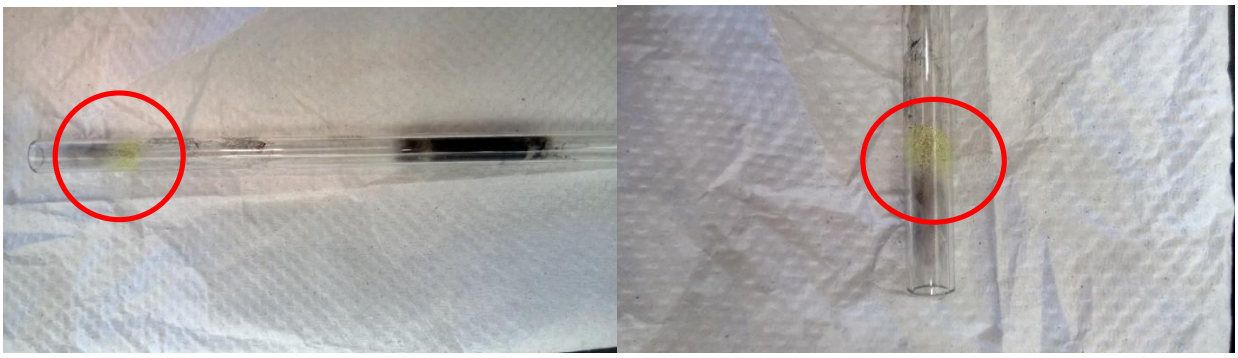

Figure 7.9: *Yellow S deposited (marked by red circle) at the outlet when nano-iron oxide (HD-2 and HD-3) was used as a catalyst.*

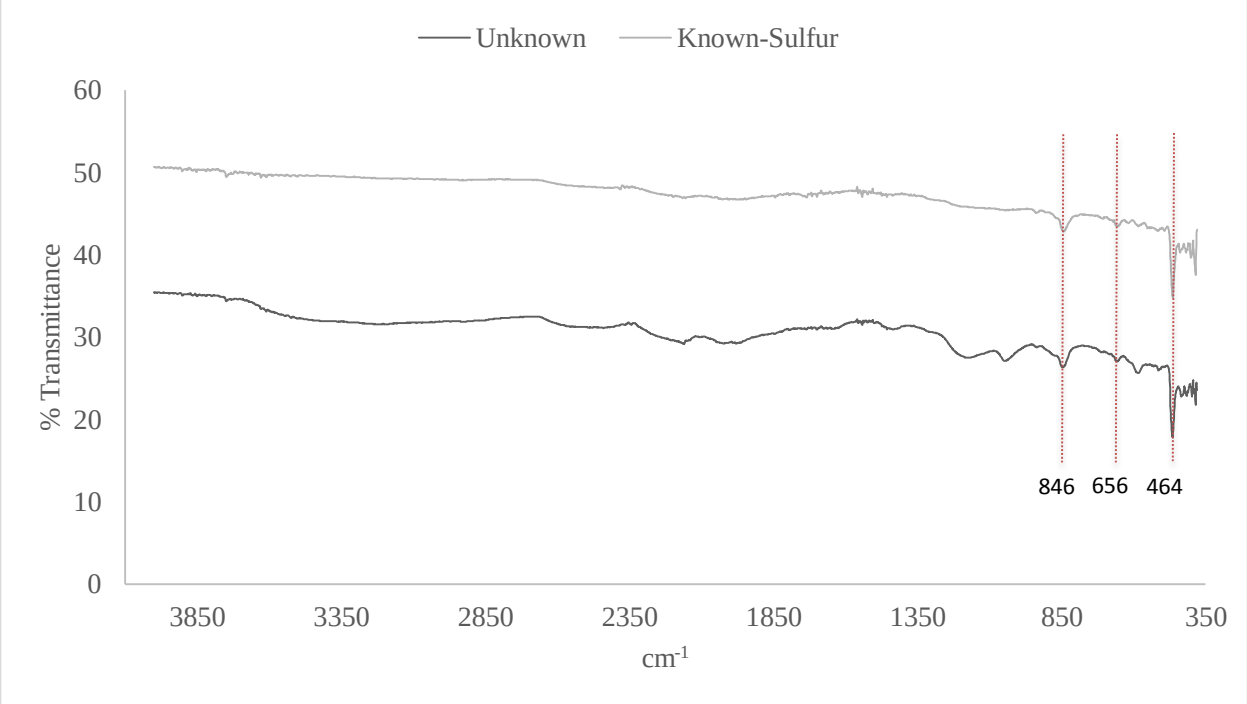

Figure 7.10: *FTIR spectra of unknown yellow compound compared to known yellow elemental S.*

This observation is not consistent with previous findings as precipitation of elemental S in a packed bed reactor using Fe_2O_3 has not been reported. Most processes which utilize iron oxide are assumed to follow Eq. 28, where the reaction takes place between 50-120°C. The iron oxide is converted into iron sulfur and the process stops once all of the iron oxide is converted. In most cases, the spent iron oxide is regenerated via Eq. 29 either by taking the column out of service or continuous-regeneration via addition of oxygen to the gas stream. Addition of oxygen will lead to formation of SO_2 in a redox reaction. Generation of SO_2 is unwanted and requires additional steps to remove it. The production of elemental S over SO_2 is more favorable in this case. The proposed reaction pathway in which sulfur was produced is shown in Figure 7.11.

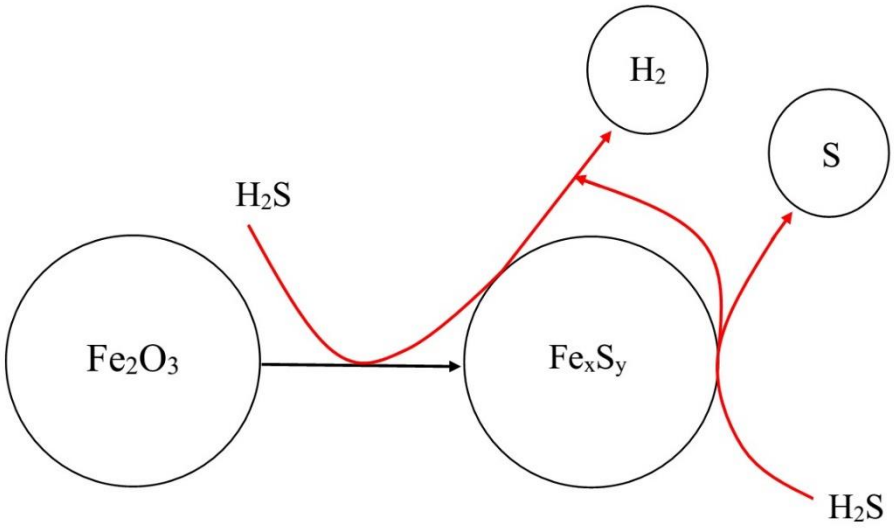

Figure 7.11: *Proposed reaction pathway in which Fe_xS_y becomes catalytically active in decomposing H_2S leading to production of elemental sulfur and hydrogen above 210°C.*

The conversion of Fe_2O_3 to Fe_xS_y, where x (between 1-3) and y (between 1-4) are integers, is a well understood process and has been previously observed[167, 175-178]. Evidence of water molecules at the early stages of the experiment suggest a reaction pathway given by Eq. 28.

Precipitation of S molecules can only be facilitated by breakdown of H_2S via Fe_xS_y, since it is thermodynamically unfavorable for $H_2S \rightarrow H_2 + S$ on Fe_2O_3 at 210°C. The result shows the potential of Fe_xS_y as an active compound in the breakdown H_2S at 210°C. H_2S removal capacity of HD-3 was 42% greater than HD-2 at 210°C. This large increase in capacity can be attributed to the larger surface area of HD-3. Significantly higher amount of sulfur was produced when using HD-3, as more H_2S was able to react with the catalyst due to large number of reaction sites available.

The reaction temperature was then stepped up from 210°C to 255°C. Experiments carried out at 255°C were able to remove H_2S from the gas stream at 96% efficiency when using HD-2, but the removal capacity of HD-2 was decreased to 0.48 gHgS at 255°C. After complete saturation of the catalyst bed, the physical appearance of the catalyst changed from red-brown color to black as the HD-2 was completely converted to Fe_xS_y. The catalyst was no longer in powdered form, as it had coagulated together into a solid mass. Meanwhile, sample HD-3 showed an increase in adsorption capacity to 3.38 gHgS at 100% removal efficiency. As expected, HD-3 changed from unreacted brown color to black in appearance, but stayed in a powdered form. The higher reaction temperature showed no S^0 production in HD-2 and HD-3.

7.3.2.2 Copper Oxide

Sample CO was able to remove 0.04 gHgS at 110 °C. A removal efficiency of 100% was achieved for the initial 60 minutes before 100 ppm of H_2S was observed at the outlet. Water droplets were seen at the outlet of the reactor bed at 110°C but no S particles were observed. Increasing the temperature to 210°C led to a much improved results. The tail gas was H_2S free for before 65 hours before H_2S breakthrough occurred. The H_2S adsorption capacity was calculated

to be 1.91 gHgS, which was comparably larger than the capacity of HD-2 at 210 °C. The reaction pathway through which the CO sample was able to decompose H_2S was:

$$CuO + H_2S \xrightarrow{yields} CuS + H_2O. \quad (48)$$

After two hours, H_2O molecules were no longer seen at the outlet. It is predicted that a secondary reaction in the packed-bed was taking place as follows:

$$CuO + CO_2 \xrightarrow{yields} CuCO_3 \quad (49)$$

$$2CuCO_3 \xrightarrow{@>210\ ^\circ C} Cu_2O + 2CO_2 + \frac{1}{2}O_2 \quad (50)$$

$$Cu_2O + H_2S \xrightarrow{yields} Cu_2S + H_2O \quad (51)$$

Color change was noted for the reacted CO sample. The sample had gone from the initial black color to a mixture of green-blue, where the catalyst solidified into a singular solid piece. The formation of green-blue product points to existence of unreacted $CuCO_3$. IR analysis of the reacted CO sample were inconclusive in confirming production of CuS (see Figure 7.12). No peaks were observed in the IR spectrum of 4000-380 cm^{-1}. When the temperature was increased to 255°C, at the CO performed at 100% efficiency at H_2S removal for over 36 hours. H_2O molecules were observed to form the first two hours. Unlike samples HD-2 and HD-3, no elemental S formed at any temperature when using CuO.

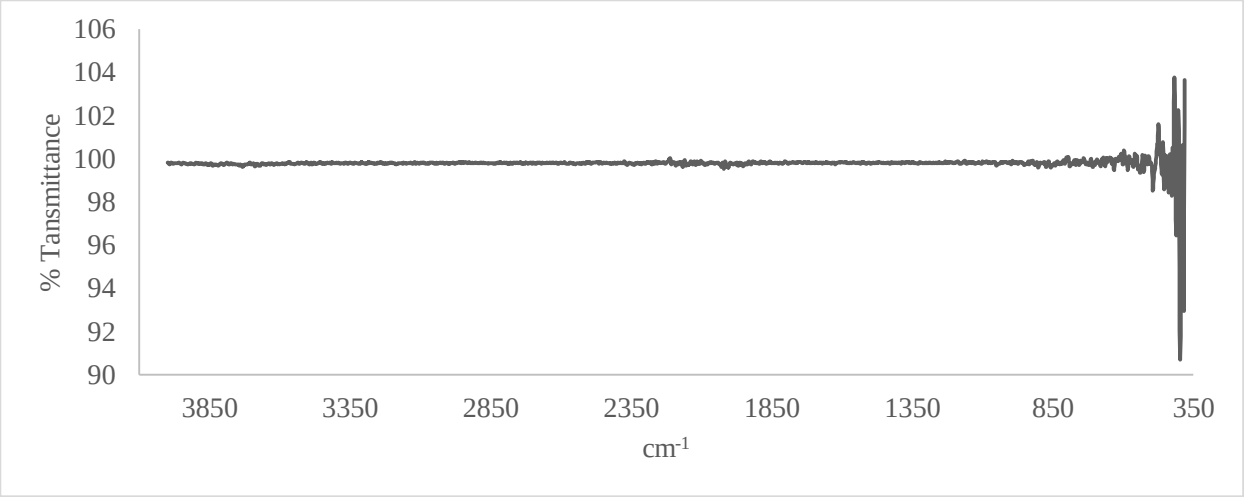

Figure 7.12: *FTIR spectra of CuS sample showed no identifiable IR peaks.*

7.3.3 Thermal regeneration

7.3.3.1 Biochar

Thermal regeneration was carried out for several samples of biochar. Sample BC-4 initially showed H_2S removal rate of 55.1 mg of H_2S per gram of biochar at 100°C. The sample was then regenerated at 300°C for five hours without any gas flow. After the regeneration cycle, the sample was retested for H_2S adsorption. The regenerated sample showed a removal rate of only 36.4 mg of H_2S per gram of biochar at 100°C. This decrease in performance was as expected as the pores of the biochar are filled with elemental S and various other S-compounds. These experiments were repeated with sample BC-1 at 23°C, where initially BC-1 showed adsorption capacity of 96.9 mg of H_2S per gram of biochar. After a regeneration cycle, its adsorption capacity was reduced by 44 percent to 53.5 mHgS of biochar. Meanwhile, sample BC-4 was regenerated to 100% capacity as it was able to remove 36.4 mHgS. Biochar's ability to perform even at half its original capacity can be economically signification.

Sample	1st Cycle (mHgS)	2nd Cycle (mHgS)	Temperature (°C)
BC-1	96.9	53.5	23
BC-4	36.4	36.4	100

Table 7.7: *Comparing H_2S adsorption capacity after regeneration at 300°C.*

7.3.3.2 Metal Oxides

The mixture of H_2O+O_2 as regeneration feed gas at high temperatures (>800°C) has been shown as effective method of regenerating iron sulfides by White[179]. The oxidation of FeS by O_2 is given as:

$$2FeS(s) + \frac{7}{2}O_2(g) \xrightarrow{yields} Fe_2O_3(s) + 2SO_2(g) \quad (52)$$

where SO_2 and total sulfur concentration in the product gas are equal. When the feed gas contains only H_2O, all sulfur is converted to H_2S and the regeneration reaction is as following:

$$3FeS(s) + 4H_2O(g) \xrightarrow{yields} Fe_3O_4(s) + 3H_2S(g) + H_2(g). \quad (53)$$

In the presence of O_2 and H_2O, two additional reactions are believed to be important. Elemental S is formed via Claus reaction:

$$SO_2(g) + 2H_2S(g) \xrightarrow{yields} 2H_2O(g) + \frac{3}{2}S_2(g), \quad (54)$$

$$2Fe_3O_4(s) + \frac{1}{2}O_2(g) \xrightarrow{yields} 3Fe_2O_3(s). \quad (55)$$

Regeneration of the spent catalyst in this study showed no production of H_2S, because of the low reaction temperature 420°C. The Claus reaction requires temperatures above 800°C for breakdown of SO_2 into elemental S. A physical change in color was observed when the metal sulfides were regenerated. The color changes on the catalyst surface are summarized in Table 5.8. After the sample was exposed to the regeneration feed gas for 12 hours, it changed color to orange-brown. Iron oxides of this color are identified as the hemati form of iron oxide (α-Fe_2O_3), which was confirmed by the FTIR spectra of the sample. The spectra also showed the existence of bands at 1100-950 cm^{-1} assigned to Fe-S (see Figure 7.13a-b). This indicates <100% regeneration of the catalyst at 420 °C under H_2O+O_2 mixture.

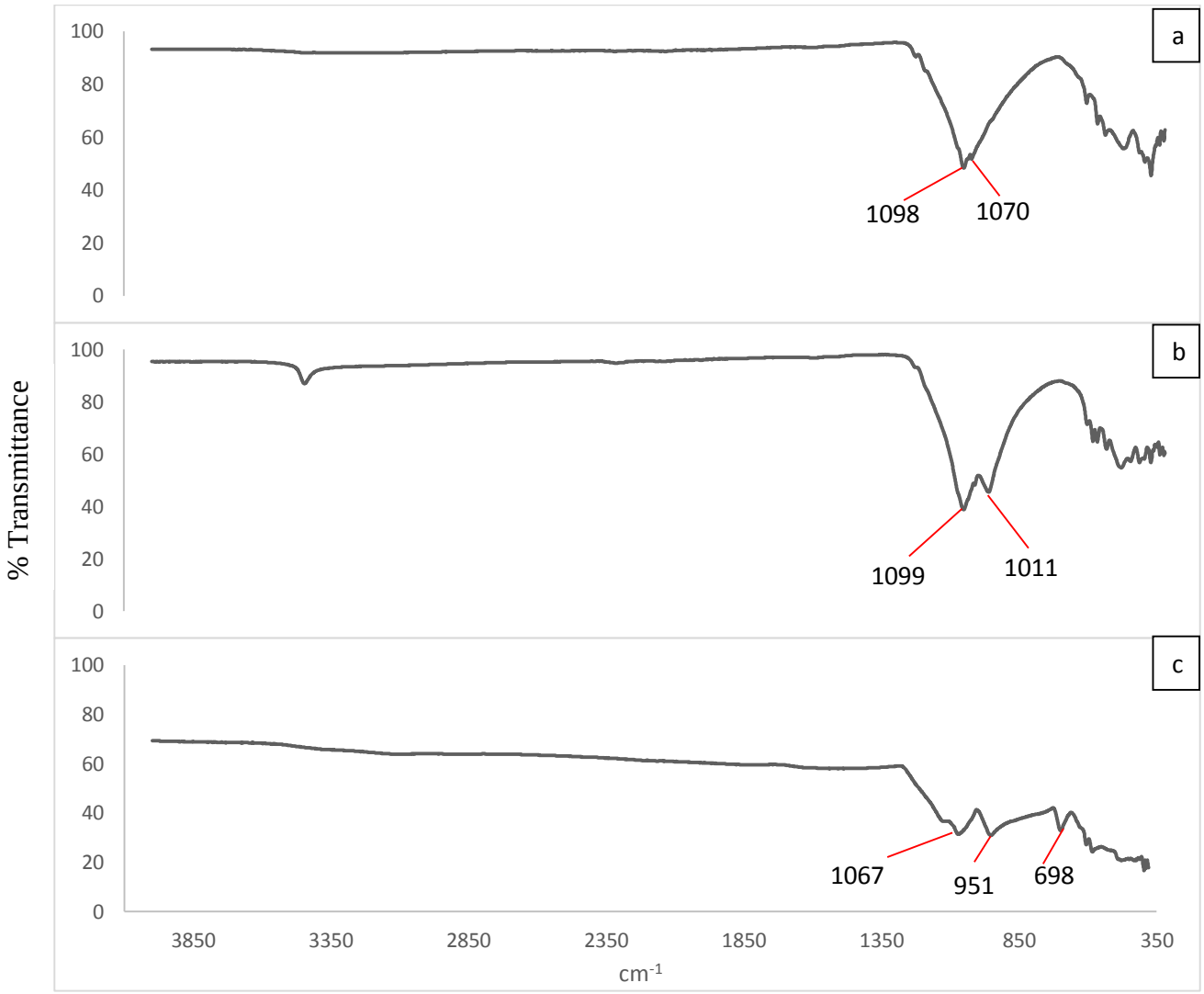

Figure 7.13: *FTIR spectra of (a) HD-2, (b) HD-3, and (c) CO after being regeneration at 420 °C.*

Figure 7.13c shows the IR bands of regenerated CO sample. The CO sample was regenerated via:

$$2CuS + 2O_2 \xrightarrow{yields} 2CuO + S_2O_2 \quad (56)$$

$$CuS + H_2O \xrightarrow{yields} CuO + H_2S \quad (57)$$

$$2Cu_2S + 3O_2 \xrightarrow{yields} 2Cu_2O + 2SO_2 \quad (58)$$

$$Cu_2 + 2Cu_2O \xrightarrow{yields} 6Cu + SO_2 \quad (59)$$

Regeneration of the CO sample utilized both the H_2O and O_2 in the gas stream as explained by Eqs. 56-59. A careful look at Eq. 59 shows the production of Cu instead of CuO, which was observable in the final product. The regenerated CO sample contained a mixture of brown and black powder. This indicates the formation of Cu (which was brown), and CuO (which was black) after regeneration.

Sample	Unreacted Color	Reacted Color	Regenerated Color
HD-2	Red-Brown	Black	Dark brown
HD-3	Brown	Black	Orange-Brown
CO	Black	Green-Blue	Brown-Black mixture
NO	Grey	Grey	Grey
FO	Black	Black	Dark brown

Table 7.8: *Characteristic color change of metal oxides as they are converted into iron sulfide.*

The regenerated samples were tested for H_2S removal (Table 7.9). Sample CO had the highest H_2S adsorption capacity at 0.88 gHgS of all the samples tested. There was a larger decrease in performance in HD-2 and HD-3, which was surprising. This decrease in capacity can be attributed to incomplete regeneration of the samples; they require regeneration at higher temperatures (>420 °C).

Sample	Total Capacity (gHgS) @ 210 °C
HD-2	0.22
HD-3	0.65
CO	0.88
FO	0.31

Table 7.9: *Adsorption capacity of the metal oxides after being regenerated and tested again for H_2S adsorption.*

7.4 Conclusion

The results from this study showed the potential of a combined system containing biochar plus a metal catalyst as an H_2S adsorbent system. Four different biochar samples derived from various feedstocks were tested and analyzed for H_2S removal. The data showed that biochar produced from hardwood (BC-1) has the largest H_2S adsorption capacity at 59.4 mHgS of at 100°C and 96.9 mHgS at 23 °C. The influence of micropore volumes on H_2S adsorption capacity was evident. Samples with larger micropore volumes have largest H_2S adsorption capacity. It is no longer sufficient to say activated biochar with the largest surface area will necessarily be the best performing H_2S adsorbent. Pore volume must be taken into account when deciding on an activated biochar. Changes in surface chemistry also affected the efficiency of H_2S removal. It was demonstrated that a decrease in pH value by 1.16 units decreased the H_2S adsorption by 11.8 mHgS.

Metal oxide catalysts were tested for H_2S decomposition. The lab-synthesized Fe_2O_3 nano-size catalyst HD-3 was the best preforming catalyst with H_2S removal of 3.38 gHgS at 255 °C. A reaction temperature of 210 °C was optimal for sample HD-2, CO, and FO to remove maximal

H_2S from biogas CO (1.76 gHgS) > HD-2 (1.67 gHgs) > FO (1.04 gHgs). Elevated reaction temperature of 255 °C resulted in decreased adsorption capacity in the HD-2, CO, and FO samples. This indicates the existence of a critical temperature above which adsorption performance for some catalysts may start to deteriorate. Formation of S^0 at 210 °C with HD-2 and HD-3 samples was observed. A new reaction pathway was proposed to explain the decomposition of $H_2S \rightarrow S^o + H_2$ with HD-3 and HD-2 samples.

Chapter 8: Conclusion

This study shows the potential utilization of locally obtained biomass as energy source and its potential to mitigate harmful GHGs. The significant conclusions from this study are:

1. On Long Island, New York, 234 million m^3 of CH_4 can be produced annually, which is equivalent to 2.52 TW-h of power or nearly 12% of total electricity consumed locally. Upgrading of available biogas is valued at over $125 million annually.
2. Using sonolysis, iron oxide catalyst with surface area ranging from 195-16 m^2g^{-1} were produced in n-decane and hexadecane solvents. A strong correlation ($R^2 > 0.59$) between sonication time and surface area was established.
3. The maximum BET surface area of 1103 m^2g^{-1} was obtained using a hardwood based biochar sample after treatment at 850 °C for three hours under a CO_2 flow rate of 200 $ml.min^{-1}$. Physical activation with CO_2 developed activated biochars with higher surface area then biochars oxidized by O_2. Activation time and temperature are the two most important factors affecting surface area.
4. The microscopic structures of each biochar was highly dependent on the feedstock used. Large amount of alkali salts and metal oxides were present on the surface of biochars. These salts were largely responsible for the surface chemistry (pH > 6) of the samples.
5. The data showed that biochar produced from hardwood had the largest H_2S adsorption capacity at 59.4 mHgS of at 100 °C and 96.9 mHgS at 23 °C. Samples with larger micropore volume have larger H_2S adsorption capacity. It was demonstrated that decrease in pH value by 1.16 units decreased the H_2S adsorption by 11.8 mHgS.

6. The lab synthesized α-Fe_2O_3 nano-size catalyst HD-3 was the best preforming catalyst with H_2S removal of 3.38 gHgS at 255 °C. The sample was synthesized via ultrasonication in a mixture of hexadecane and $Fe(CO)_5$. The BET Surface area of HD-3 was 53.17 m^2g^{-1}. Reaction temperature of 210 °C was optimal for HD-2 (α-Fe_2O_3), CO (CuO) and FO (FeO) to removal maximum H_2S from biogas (CO>HD-2>FO). Samples CO, HD-2, and FO removed 1.76 gHgs, 1.67 gHgs and 1.04 gHgs, respectively. Elevated reaction temperature of 255 °C resulted in decreased adsorption in CO, HD-2, and FO. A new reaction pathway was proposed to explain the decomposition of $H_2S \rightarrow S^o + H_2$ on HD-3 and HD-2 samples.

Chapter 9: Future Work

The present study focused on removal of H_2S from a biogas stream via adsorption on activated biochar and metal oxides. Aditionally, the study also looked at the potential of biogas production on Long Island, NY. Further work can be carried out to improve upon the results found in this study.

- A closer examination of the C&D waste stream being landfilled on LI needs to be carried out. C&D is known to generate high concentration of H_2S and this can have adverse effects on the environment and on public health. A technological viability investigation needs to be conducted for increasing biogas production from C&D while decreasing H_2S generation.
- Sonochemical synthesis of additional metal catalyst including CuO and ZnO needs to be carried out. This study showed the potential of the CuO catalyst to be an effective catalyst for H_2S decomposition. A decrease in particle size may help improve the adsorption capacity of the CuO catalyst. A closer examination of the H_2S decomposition and how CO_2 interacts with CuO catalyst is needed.
- Additional hardwood biochar samples need to be studied for H_2S adsorption. The four different biochar samples were studied showed a wide range of H_2S adsorption capacity. In order to increase the H_2S adsorption capacity, biochar needs to have larger micropore volume and surface area. Physical activation via steam may help improve surface area and micropore volume development in the biochar. A deeper look at the basic and acidic functional groups present on the biochar surface is also needed. The measurement of adsorption capacity at temperatures above 200 °C need to be taken since the existence of

metal oxides was observed on the biochar samples. The higher temperatures may activate the metal oxides present on the surface leading to increased adsorption capacity.

- An additional examination of the proposed pathway of $H_2S \rightarrow H_2 + S^0$ decomposition on nano-size Fe_2O_3 catalyst needs to be carried out. The study found the production of elemental S was dependent on the temperature. This temperature dependence needs to be investigated. Improvement in adsorption capacity after regeneration of the used catalyst is important.

Appendixes A

Renewable Portfolio Standards and Financial Incentives:

On September 22, 2004, the State of New York adopted a Renewable Portfolio Standard (RPS), which requires that 25% of the state's electricity come from renewable sources by 2013. The standard identifies two tiers of eligible resources, a "Main Tier" and a "Customer-Sited Tier." The main tier is mandatory and is to account for 24% of the standard. Eligible sources include biogas, biomass, liquid biofuel, fuel cells, hydroelectric, solar, ocean or tidal power and wind. The customer-sited tier will make up the remaining 1% of renewable energy sales and is to come from voluntary green market programs. Sources of energy that count toward the customer-sited tier include fuel cells, solar, and wind resources[1]. In order to meet the 25% target, the state will need to add approximately 3,700 MWs of electricity generated from renewable resources. Forecast for the program are for reduction in air emissions of NO_x by 6.8%, SO_2 by 5.9%, and CO_2 by 7.7%, with a greater proportion of emission reductions expected in New York City and Long Island[2].

	Personal Tax	Corporate Tax	Sales Tax	Property Tax	Rebates	Grants	Loans	Industry Support	Bonds	Performance Based Incentives
State	3	1	1	3	11	1	4	2	-	-
Federal	3	4	-	-	-	3	5	1	-	1

Table A.0.1: ***Financial incentives for renewable energy. Source: DSIRE 2010***

[1] http://www.pewclimate.org/what_s_being_done/in_the_states/rps.cfm

[2] Flynn, William M. *PSC votes to adopt aggressive renwable energy policy for New York State – Goa to increase renewable energy purchases from 19 percent to 25 percent by 2013.* State of New York Public Service Commission, 2004.

	Personal Tax	Corporate Tax	Sales Tax	Property Tax	Rebates	Grants	Loans	Bonds	Green Building
State	1	1	-	1	26	2	4	-	1
Federal	2	3	-	-	-	2	4	-	-

Table A.0.2: ***Financial incentives for energy efficiency. Source: DSIRE 2010***

Power sources and Energy Consumption:

In 2007, Long Island Power Authority (LIPA) imported 41% of electricity consumed. Much of the electricity was purchased and transported through long-distance transmission lines and undersea cables from off-Island power sources. Long distance transmission lines are known to be inefficient resulting in higher electrical costs for LI. As of 2005, LI power plants produced 59% of electricity from oil, 35% form natural gas, and 6% from waste-to-energy incinerators, and 3% from other fossil fuel sources.

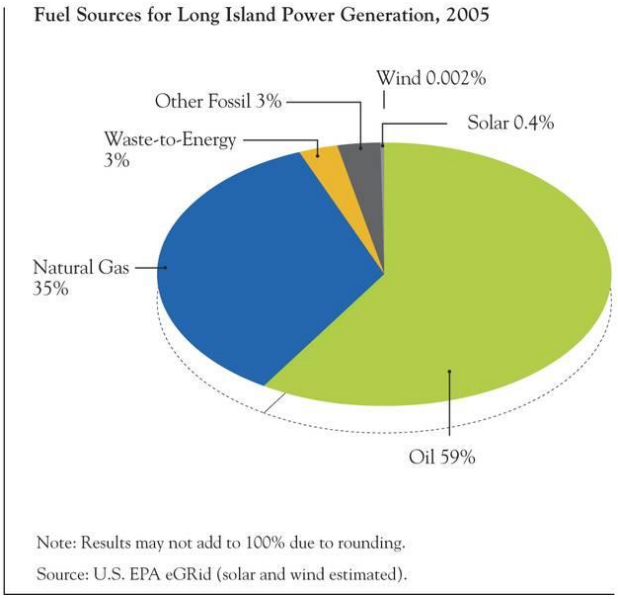

Residential, commercial and industrial electricity consumption in 2007 increased 2.5% over 2006. Residential electricity use has grew 27%, while population grew less than 9%, over the period 1998-2007. Natural gas saw a sharp increase of 14% in consumption in 2007, which resulted in 5.3 million tons of CO_2 emissions. However, a large portion of the increase was due to converting space heating equipment from oil to natural gas which reduced CO_2 emissions by almost a third. In order to meet the RPS set by the State, LI would need to cut its energy consumption growth to less than 0.4% instead of the present 2.5 percent[3].

[3] http://longislandindex.org/index.php?id=206

Appendix B

WWTPs Biogas Potential:

Total sludge = 207,406 ton $year^{-1}$ → 414,812,000 lb $year^{-1}$

Assume Volatiles are 75%

Volatile Solids to Digestion = 414,812,000 x 0.75

= 311,109,000 lb $year^{-1}$

Assume 50% VSS reduction through digestion

VSS Destroyed = 311,109,000 x 0.50

= 155,554,500 lb $year^{-1}$

Assume 16 ft^3 of digester gas produced per pound of volatile solids destroyed

Gas production = 155,554,500 x 16

= 2,488,872,000 ft^3 $year^{-1}$

Facility	Location	Design flow rate (actual flow rate) mgd	Sludge	Digester
Belgrave STP	Great Neck	2		
Birches	Locust Village	0.012		
Cedarhurst STP	Cedarhurst	1		
Glen Cove STP	Glen Cove	6		
Great Neck Village STP	Great Neck	1.5		
Great Neck Water Pollution Control Plant	Great Neck	3.8		

Greater Atlantic Beach STP	West Long Beach	1.5 (0.8)	≤12,000 gallon/day	Two AD;
Greenport STP	Greenport	0.65		
Huntington STP	Huntington	2.5 (2.5)	12 tons/day	Two AD;
Jones Beach STP	Jones Beach	2.5		
Lawrence STP	Lawrence	1.5		
Long Beach STP	City of Long Beach	7.5 (5.5)	2 ft^3	One AD
Bay Park	Bay Park	70		
Cedar Creek	Cedar Creek	72		
Northport STP	Northport	0.34		
Ocean Beach STP	Ocean Beach	0.5		
Oyster Bay STP	Oyster Bay	1.8		
Patchogue STP	Patchogue	0.5		
Plum Island Animal Disease Center	Plum Island	0.08		
Port Washington STP	Port Washington	4		
Riverhead STP	Riverhead	1.3		
Sag Harbor	Sag Harbor	0.25		
Port Jefferson	Port Jefferson	0.85		
SUNY	Stony Brook	2.5		
Bergen Point	Bergen Point	30.5		
Kings Par	Kings Park	1.2		

Shelter Island Heights STP	Shelter Island	0.05		

Table B.0.1: *List of WWTPs on Long Island*

Appendix C

Simulation Setup

The strength of Lattice Boltzmann (LB) lies in its ability to easily compute the advection-diffusion transport in complex porous media. LB's ability to decouple hydrodynamics from mass transfer while preserving the physics of the problem makes it a very powerful tool. In this study, we simulate gas flow through a packed bed of solid adsorbents. We look at how change in pressure, system temperature and packing arrangement affect adsorbents ability to remove impurities in the gas stream.

The D3Q19 model was used in this simulation, where each node has 19 velocity vectors: 1 is in the center, 6 along the axis and 12 for all combination of two axes. The following relationships were used to define pressure (P) and kinematic viscosity (v) of the fluid[4,5]:

$$P = \frac{\rho}{3}, \qquad v = \frac{1}{3}\left(\tau - \frac{1}{2}\right).$$

These equations show that pressure and mass are tied up in LBM; therefore any pressure change translates to change in density. This is the reason why LBM is considered a weakly compressible approximation of the Navier-Stokes equation. Note that $\tau > ½$ is required for physical viscosity. Numerical instability occurs as $\tau \rightarrow ½$.

Treatment of boundary conditions in LBM is very simple. In this work, we impose pressure driving flow conditions at the inlet and outlet. The pressure difference is created by imposing small density drop in the flow direction. Periodic boundary condition is established in the flow direction, where the outgoing fluid at the outlet face is streamed back to the inlet face. This assures

[4] M. C. Sukop and D. T. Thorne, *Lattice Boltzmann modeling : an introduction for geoscientists and engineers*. (Springer, Berlin ; New York, 2006).
[5] M. C. Sukop and D. Or, Water Resour Res **40** (1) (2004)

mass conservation in the system. No-slip boundary conditions are placed everywhere else in the lattice. This requires that the velocity component parallel to the flow must be zero at the solid surface. This means the outgoing fluid is bounced back towards the interior of the fluid in a way that preserves mass.

As stated above, one of key strengths of LB is its ability of decouple hydrodynamics from mass transfer. Therefore, we initially solve the velocity profile of the packed bed and then superimpose the profile on the concentration fields. It is assumed that velocity fields are not affected by adsorption/desorption or surface reaction. Identical particle size, packing arrangement, and grid size used in solving hydrodynamics is used in the diffusion lattice, while setting the relaxation time of diffusion (τ_d) independent from hydrodynamic relaxation time (τ_h). Lattice mass diffusivity is related to actual diffusivity via grid and time step size as $D_A = D_L * \Delta x^2/\Delta t$.

Advection-Diffusion in LBM

Transport of fluids can occur through the combination of advection and diffusion. Advection is the transport associated with flow of a fluid, while diffusion is transport associated with random motions within a fluid. A system of advection-diffusion can be easily simulated using LBM. Figure C.1 illustrates the ability of LBM to easily solve the advection-diffusion equation given as

$$\frac{\partial C}{\partial t} + \nabla \cdot (uC) = D\nabla^2 \mathrm{C}.$$

In regards to Figure 1, only diffusion is considered with the following initial conditions,

$$C(x, t_o) = \begin{cases} C_o & if\ x \leq 0 \\ 0 & if\ x > 0 \end{cases}$$

which leads to a solution that can be written as

$$C(x,t) = C_o\left(1 - erf\left(\frac{x}{\sqrt{4Dt}}\right)\right),$$

where concentration (C) is analogous to fluid density ρ and diffusion (D) is equal to fluid viscosity (v)[180].

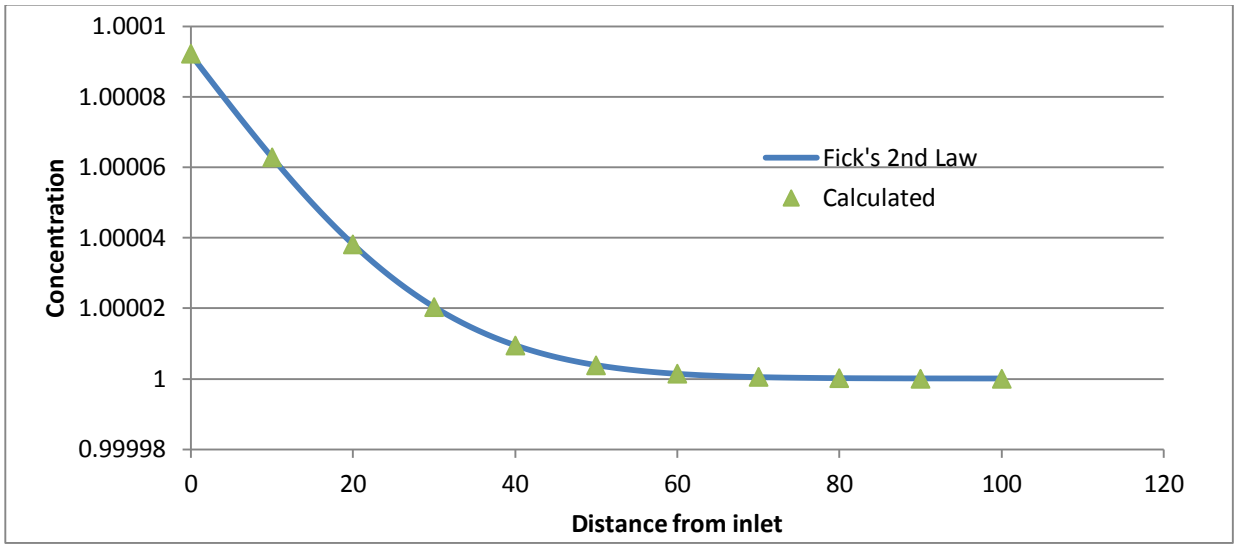

Figure C. 1: *Diffusion of matter in an infinitely long pipe with fixed concentration at inlet x=0 with initial concentration (C_o) of 1.00009. The calculated solution from LBM is in good agreement with the analytical solution.*

Poiseuille Flow

We investigate the performance of LBM D3Q19 lattice for steady Posieuille channel flow. In the pipe, the velocities at the wall are zero (no-slip condition) and the velocity reaches its maximum in the middle. Figure C.2 illustrates the velocity profile in a pipe of width 2L is parabolic and given by

$$v\left(\frac{d^2u}{dy^2}\right) + F = 0,$$

where v is the fluid viscosity and F is constant force along the x-axis. Enforcing the no-slip boundary condition gives a steady-state solution for the velocity as:

$$u(y) = \frac{F}{v}\left(\frac{y^2}{16} - \frac{x^2}{4}\right).$$

Periodic boundary conditions are applied in the x-axis, while the y and z axis are treated solid walls. The flow is initially at rest and is accelerated by a constant pressure parallel to the x-axis. In our experiment the D3Q19 domain contains 50 x 24 x 24 nodes. The viscosity is set to v = 1/6 and the driving force is ΔP=0.0001.

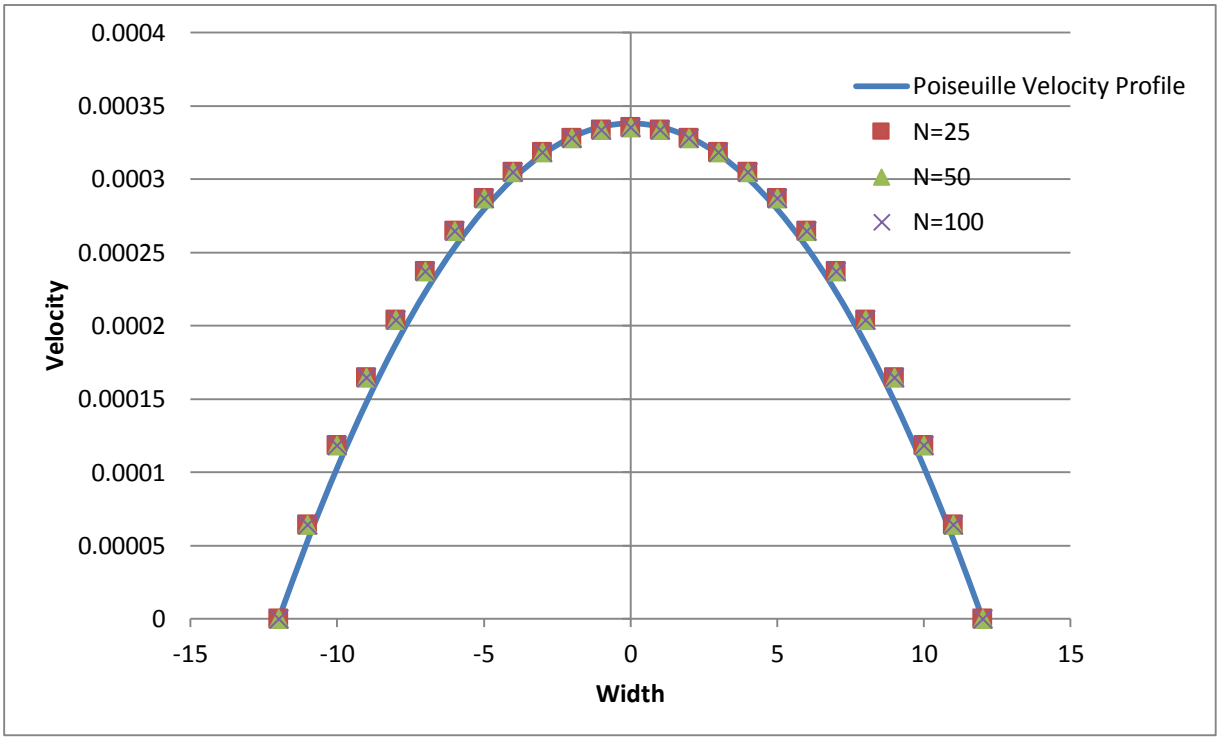

Figure C. 2: *Comparison of the velocity profile for the Poiseuille Flow in a tube at different lattice resolution (N).*

Flow analysis in randomly arranged porous media

Figure C.3 shows the calculated pressure gradient in the randomly arranged porous media. The lattice size was 80 x 40 x 40, with the porous media size of 40 x 40 x 40. The kinematic viscosity v = 1/6, and ΔP = 0.001. This figure shows that pressure drop occurs strictly in the porous

media; the pressure is constant outside the porous media; the average pressure drop across the membrane is independent of the porosity (ε).

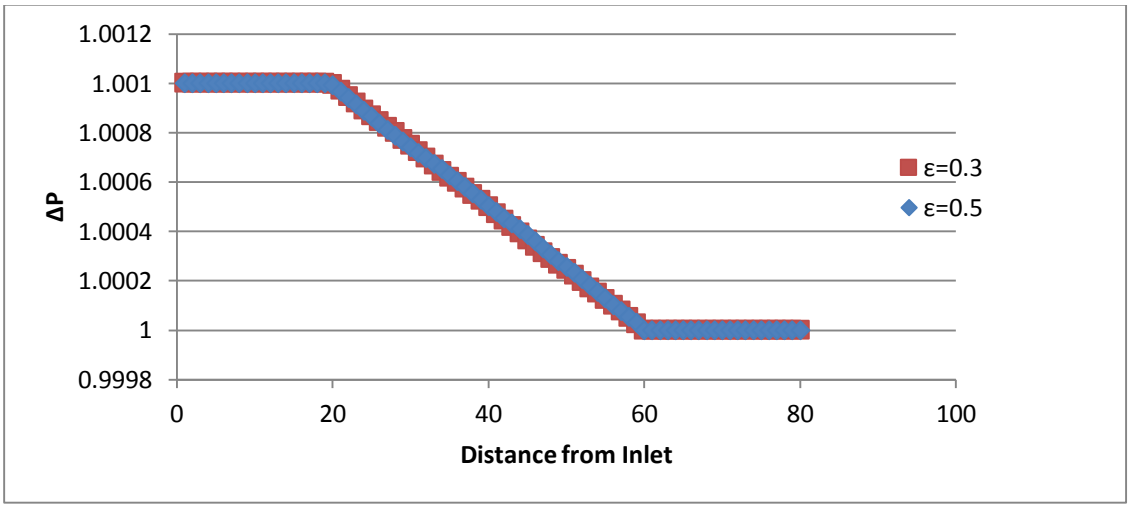

Figure C. 3: *Calculated pressure distribution averaged on the plan perpendicular to the flow direction for two different porosities (ε). V = 1/6, ΔP = 0.001.*

The calculated results for dimensionless permeability (K) as a function of ΔP are shown in Figure C.4. The viscosity is fixed at v=1/6 and the ΔP is varied form 0.01 – 0.0001. This calculation shows that permeability is independent of pressure gradient, which is confirms with Darcy's Law that permeability is an intrinsic property of each porous media.

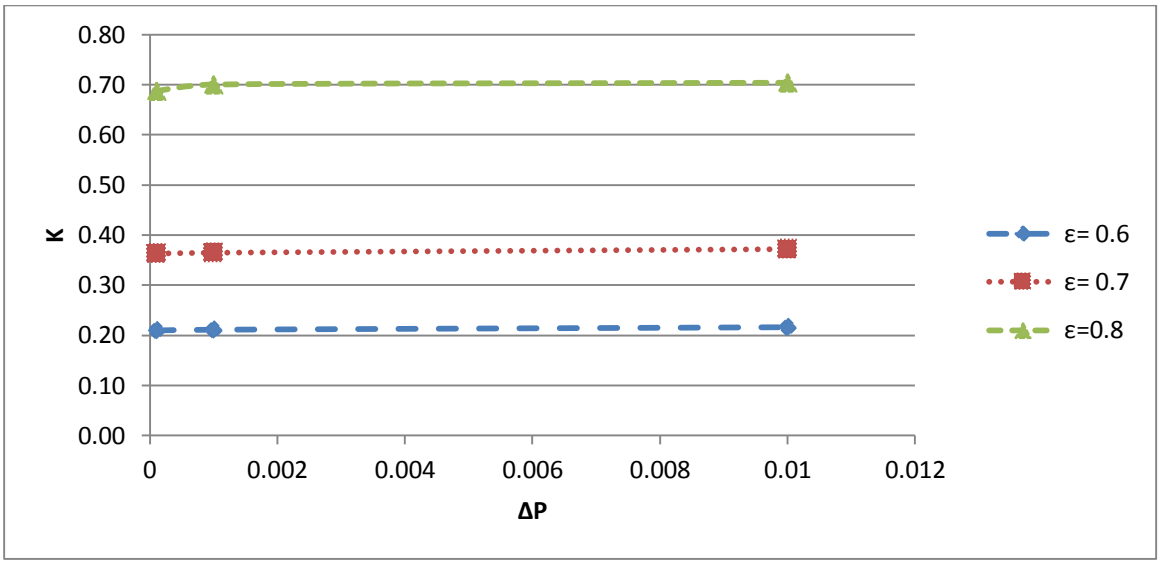

Figure C. 4: *Dependence of dimensionless permeability on the pressure gradient. V = 1/6, ΔP = 0.0001, 0.001, 0.01.*

Effects of fluid viscosity on permeability were studied and the calculated results are shown in Figure C.5. These calculations show a strong relationship between permeability and viscosity. Unfortunately, Darcy's law does not agree with these findings. As stated before, permeability is an intrinsic property of the porous media and must be independent of the viscosity of the fluid. This problem can be overcome by increasing the lattice resolution (N) in the simulation.

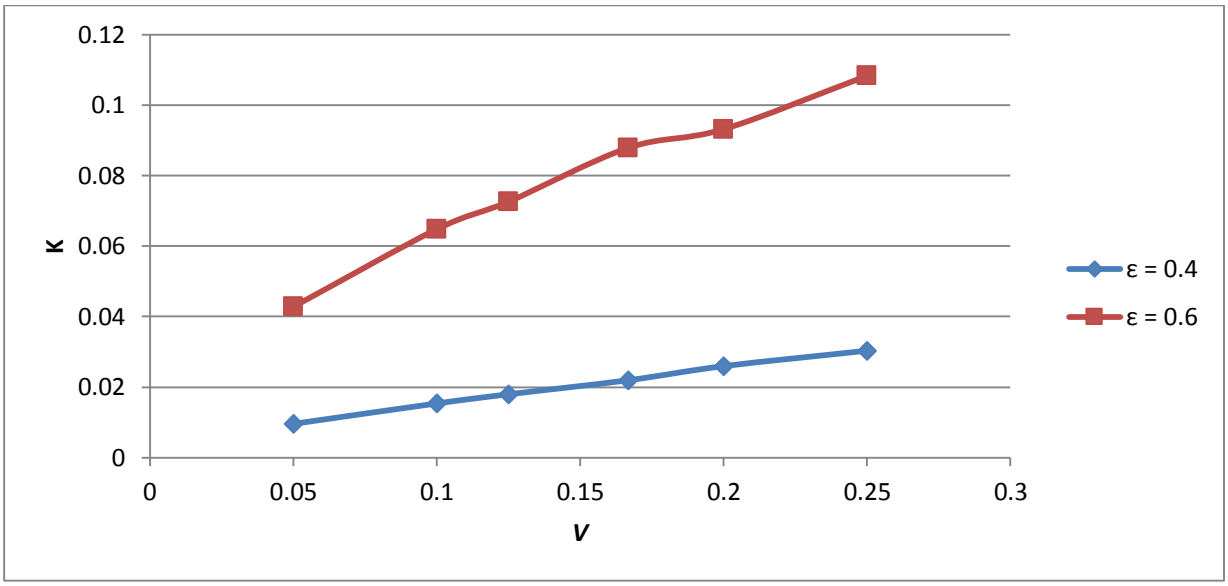

Figure C. 5: *Change in dimensionless permeability due to fluid viscosity for different porosities. 50x24x24 lattice size, ΔP=-0.01.*

Increasing the lattice resolution shows permeability is less dependent on viscosity, which follows Darcy's Law. From Figure C.6, one can see that at low viscosity the lattice resolution has no apparent effect on the permeability, while at higher viscosity the permeability values diverge from high to low resolution.

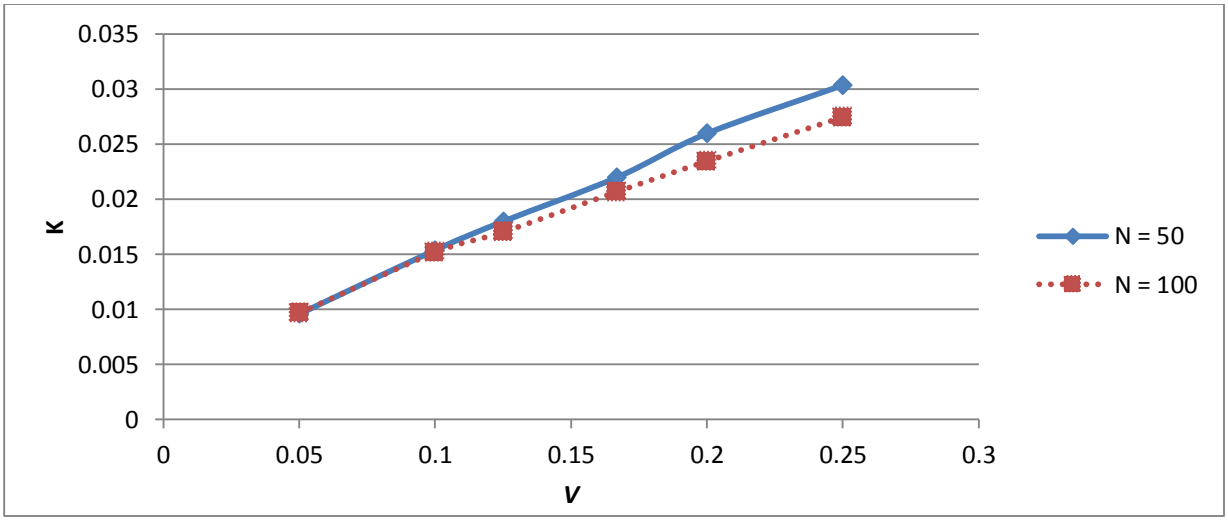

Figure C. 6: *Effects on permeability as a result of changing viscosity and resolution(N). 50x24x24 lattice size, ΔP=0.001, ε=0.4.*

Effects of Hydrodynamics

The 3D simulation was carried out on 101 x 32 x 32 grid at three different porosities 0.9, 0.8, and 0.7. The concentration profiles shown in Figure 7 correspond to Y = L/2 containing ε=.1. It is assumed that in the initial stage the adsorbent had no impurities. The concentration at inlet is held at 1.01, whereas the outlet concentration is held constant at 1.00. Few distinct observations may be made from these simulations. First, increasing porosity (ε→1) leads to higher average velocity in the system. The general velocity profile is uniform throughout the lattice in the flow direction as seen from the z-y plane; however, local velocity fluctuations were noted in media with higher porosity. The velocity profile in the x-z plane (Figure 7b) reconfirms the local fluctuation at higher porosities. Localized increase in velocity near the wall is noted as the porosity decreases. Second, higher porosity leads to more complete usage of adsorbent. For instance, when ε=0.9 nearly 96% of the total adsorbent surface area was used in comparison to only 71% when ε=0.7. The majority of the unused adsorbents were located near the outlet, as is the case in experimental settings. Third, solute concentration was evenly distributed from the center of the lattice to the walls even in the presence of a parabolic velocity profile. The solute concentration profile is not significantly influenced by the packing arrangement.

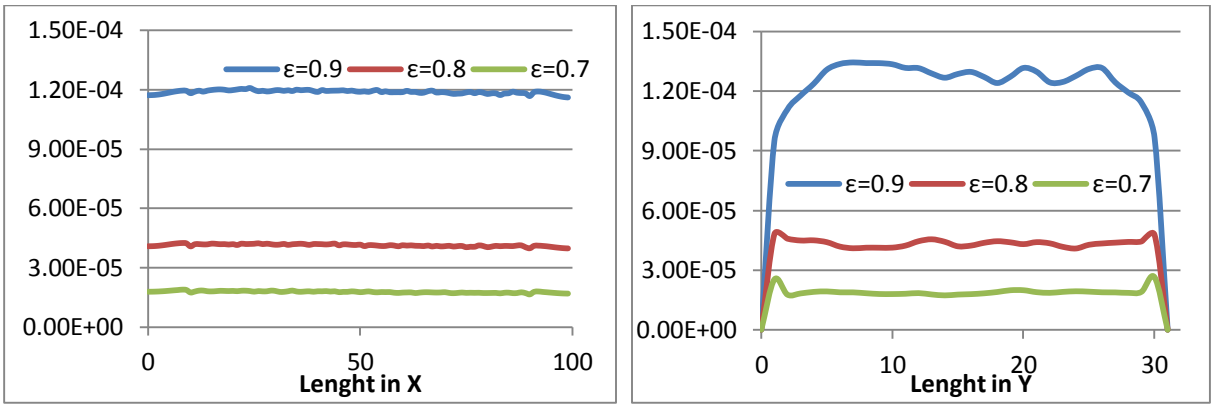

Figure C. 7: *(A) Uniform velocity flow through porous media in the flow direction (x-axis). High porosity leads to high velocity to quicker flow of gas through the system. (B) Larger magnitude of velocity was noted at the walls as porosity decreased.*

Activation Energy kJ/mol	Porosity	Percentage adsorbent Used	Average Mass increase
50	0.9	82%	0.0620
	0.8	56%	0.0471
	0.7	39%	0.0472
75	0.9	98%	0.0421
	0.8	83%	0.0535
	0.7	64%	0.0552
100	0.9	100%	0.0022
	0.8	99%	0.0046
	0.7	99%	0.0094

Table C. 0: *Changing in activation energy tends to have a profound effect on amount of adsorbent used and how much contaminate is removed from the gas stream.*

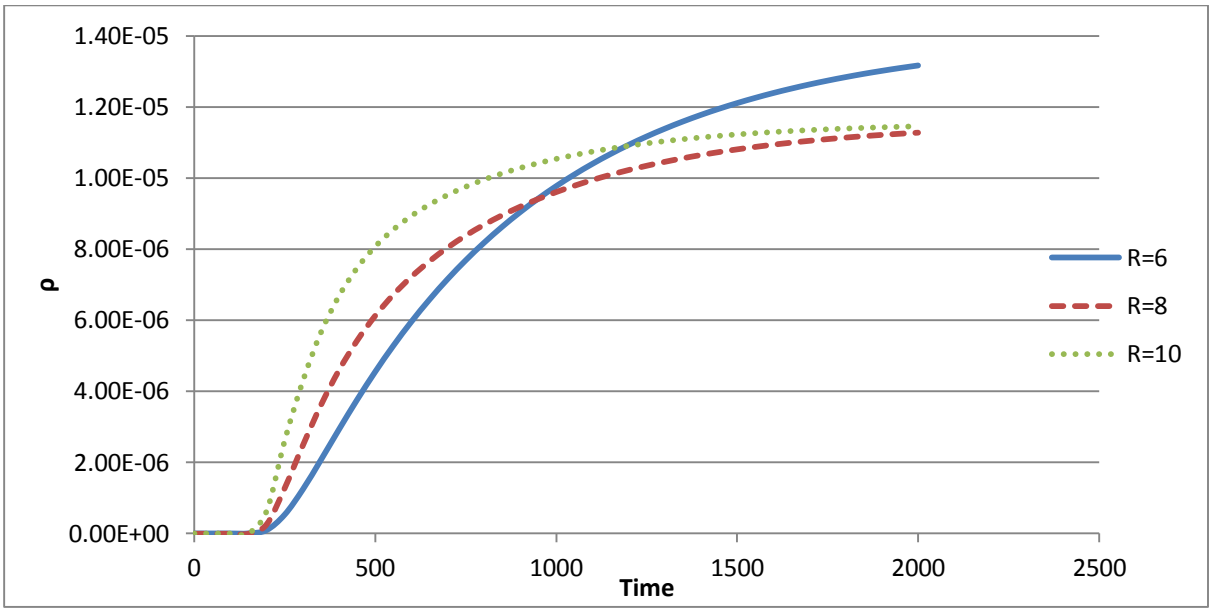

Figure C. 8: *Increase in Reynolds number leads to improved breakthrough time as observed from the outlet.*

Flow through Periodically Arranged Solid Spheres

Simulation of Gas flow through a packed column of solid spheres was conducted in a 101 x 33 x 33 lattice. The column was packed with different packing arrangements. The main objective of this study is to investigate velocity and concentration profiles of a packed bed with solid (non-porous) spheres. It was assumed that adsorption only occurred on the outer surfaces of the spheres.

The column is packed with equal size spheres (radius (r) = 7 lu) on a simple cubic (SC) arrangement. The column was packed from X=10 to X=90 leaving empty sections at the beginning and end of the lattice. It was assumed that initially (t=0) the column is free of any impurities (C_o=0). At t>0 the solute concentration at the inlet was switched to 0.001, while the outlet was held at 0. The diffusion coefficient (D) was set to 0.2 lu, which corresponds to 2.1E-5 cm^2/s in physical units.

a. 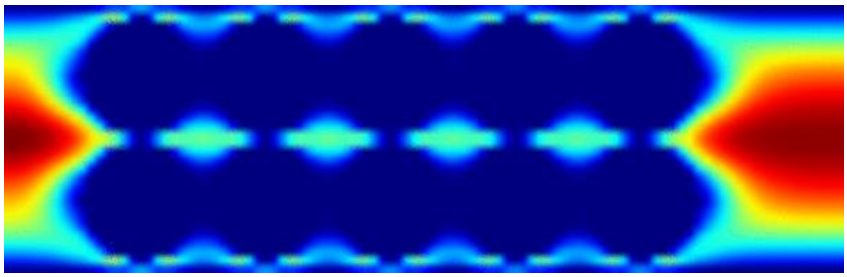 b. 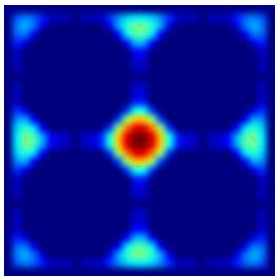

Figure C. 9: *(a) Velocity profile in the x-z plane located at y= ny/2 in a simple cubic arrangement. (b) velocity profile in y-z plane located at x=32.*

Figure C.9 (a) is a plot of the steady-state velocity profile obtained from the 3D simulations of gas flow through a packed column. The dark blue regions of the figure represent the solid spheres. The bright red spot in Figure C.9 (b) corresponds to a larger magnitude of velocity at the center compared to the outside regions. This can be attributed to the packing arrangement of the spheres. It is well known that the porosity of a simple cubic structure is approximately 0.48. The majority of this porosity exists in the center of the structure, leading to a higher magnitude of velocity in the center of the lattice.

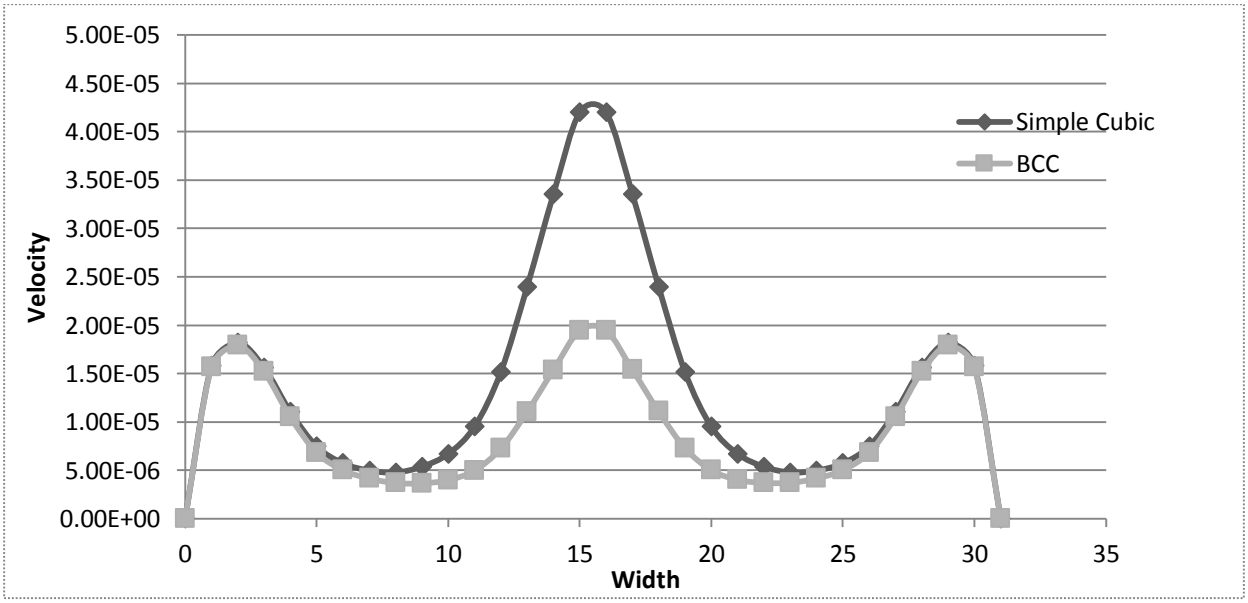

Figure C. 10: *Velocity profile comparison between simple cubic and BCC packing arrangement.*

Flow through a BCC packing arrangement led more to a uniform velocity throughout the system. Unlike SC velocity profile, BCC velocity profile had no significant uneven distribution of velocity profiles across the column. The BCC structure was more closely packed resulting in lower porosity (0.32) and even distribution of void space. Combination of these two factors leads to a lower and more uniform velocity in the system, as show in Figure C.10.

Figure 11 shows amount of adsorption that takes place moving away from the inlet of the system. Regardless of the packing arrangement the overall amount of solvent adsorbed decreases with increasing distance from inlet. This is strongly correlated to the pressure gradient present in the system.

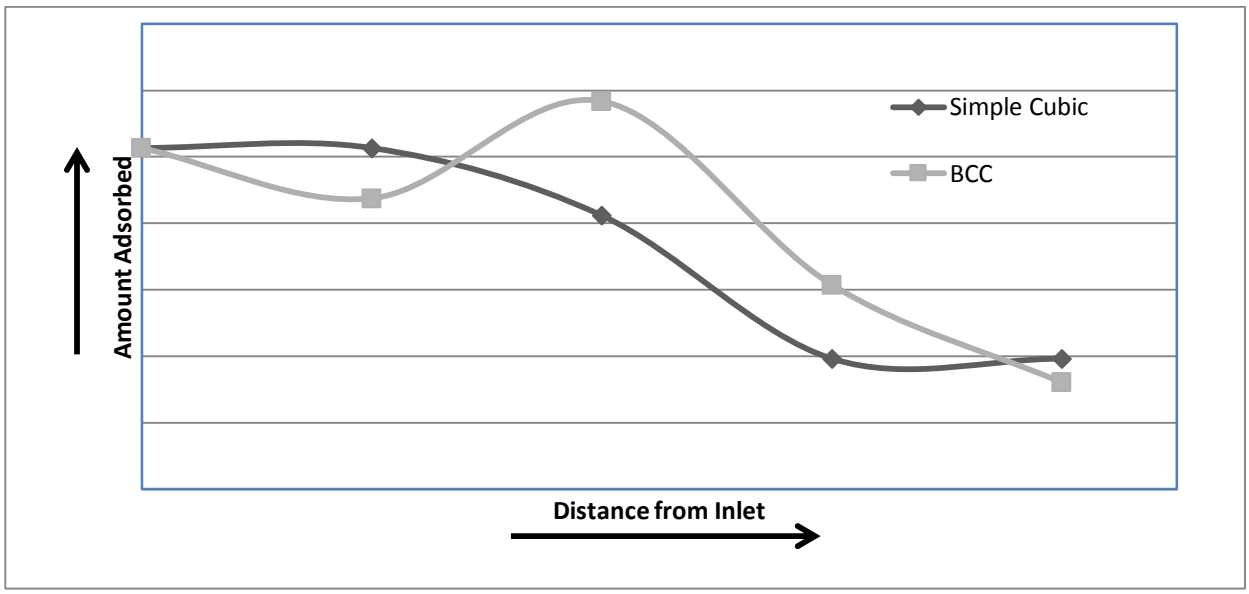

Figure C. 11: *Amount of adsorption occurring as a function of distance from the inlet for a simple cubic and BCC packing arrangement.*

1. Report No. DOE/EIA-0484(2013), 2013.
2. R. W. Howarth, A. Ingraffea and T. Engelder, Nature **477** (7364), 271-275 (2011).
3. T. Myers, Ground Water **50** (6), 872-882 (2012).
4. D. Rahm, Energ Policy **39** (5), 2974-2981 (2011).
5. N. Abatzoglou and S. Boivin, Biofuel Bioprod Bior **3** (1), 42-71 (2009).
6. P. V. Rao, S. S. Baral, R. Dey and S. Mutnuri, Renew Sust Energ Rev **14** (7), 2086-2094 (2010).
7. R. H. Zhang, H. M. El-Mashad, K. Hartman, F. Y. Wang, G. Q. Liu, C. Choate and P. Gamble, Bioresource Technology **98** (4), 929-935 (2007).
8. P. Weiland, Appl Microbiol Biot **85** (4), 849-860 (2010).
9. P. J. Crutzen, Nature **350** (1991).
10. J. B. Holm-Nielsen, T. Al Seadi and P. Oleskowicz-Popiel, Bioresource Technology **100** (22), 5478-5484 (2009).
11. J. Lelieveld, Nature **443** (7110), 405-406 (2006).
12. J. Lehmann and S. Josesph, (Earthscan, Sterling, 2009).
13. K. Kristiina, M. Tuomas, B. Irina and R. Kristiina, Agriculture Ecosystems & Environment (140), 309-313 (2011).
14. J. E. Amonette and S. Joseph, in *Biochar for Environmental Management*, edited by J. Lehmann and S. Joseph (Earthscan, Sterling, 2009), pp. 33-43.
15. C. M. Preston and M. W. I. Schmidt, Biogeosciences **3** (4), 397-420 (2006).
16. D. Matovic, Energy **36** (4), 2011-2016 (2011).
17. D. Woolf, J. E. Amonette, F. A. Street-Perrott, J. Lehmann and S. Joseph, Nat Commun **1** (2010).
18. Y. Okimori, M. Ogawa and F. Takahashi, in *Mitigation and Adaptation Strategies for Global Change* (Kluwer Academic Publishers, Netherland, 2003), Vol. 8, pp. 261-280.
19. J. Davis and D. Sentinella, (Anthroposane, www.energy-without-carbon.org, 2013), Vol. 2013.
20. P. Weiland, Applied Microbiology and Biotechnology **85**, 849-860 (2010).
21. W. Gujer and A. J. B. Zehnder, Water Sci Technol **15** (8-9), 127-167 (1983).
22. J. Rapport, R. Zhang, B. M. Jenkins and R. B. Williams, Report No. WMB-2008-011, 2008.
23. J. M. Hammer and J. M. J. Hammer, *Waste and Wastewater Technology*. (Prentice Hall, New Jersey, 2001).
24. (U.S EPA - Sources and emissions of methane throughout the United States, 2008).
25. A. A. Tsave, P. M. Soupios and E. S. Karapidakis, in *International Conference "Protection & Restoration of the Environment VIII* (Chania), Vol. 322.
26. K. Spokas, J. Bogner, J. P. Chanton, M. Morcet, C. Aran, C. Graff, Y. Moreau-Le Golvan and I. Hebe, Waste Management **26** (5), 516-525 (2006).
27. J. Bogner, K. Spokas, E. Burton, R. Sweeney and V. Corona, Chemosphere **31** (9), 4119-4130 (1995).
28. (U.S EPA - Municipal Solid Waste (MSW) in the United States: Facts and Figures, 2010).
29. I. Alternative Resources, 2006.
30. M. B. Rands, D. E. Cooper, C. P. Woo, G. C. Fletcher and K. A. Rolfe, J Water Pollut Con F **53** (2), 185-189 (1981).
31. D. R. Ranade, A. S. Dighe, S. S. Bhirangi, V. S. Panhalkar and T. Y. Yeole, Bioresource Technology **68** (3), 287-291 (1999).
32. I. Diaz, A. C. Lopes, S. I. Perez and M. Fdz-Polanco, Bioresource Technology **101** (20), 7724-7730 (2010).
33. E. Ryckebosch, M. Drouillon and H. Veruaeren, Biomass Bioenerg **35** (5), 1633-1645 (2011).
34. M. Persson, O. Jonsson and A. Wellinger, (IEA Bioenergy Task 37: Energy from Biogas and Landfill Gas, 2006).
35. A. Wellinger and A. Lindberg, (IEA Bioenergy Task 24: Energy From Biological Conversion of Organic Waste, 2005).
36. S. Cavenati, C. A. Grande and A. E. Rodrigues, Ind Eng Chem Res **47** (16), 6333-6335 (2008).
37. S. S. Kapdi, V. K. Vijay, S. K. Rajesh and R. Prasad, Renew Energ **30** (8), 1195-1202 (2005).

38. S. Basu, A. L. Khan, A. Cano-Odena, C. Q. Liu and I. F. J. Vankelecom, Chem Soc Rev **39** (2), 750-768 (2010).
39. H. J. Wubs and A. A. C. M. Beenackers, Aiche J **40** (3), 433-444 (1994).
40. M. S. Horikawa, F. Rossi, M. L. Gimenes, C. M. M. Costa and M. G. C. da Silva, Braz J Chem Eng **21** (3), 415-422 (2004).
41. R. R. Broekhuis, D. J. Koch and S. Lynn, Ind Eng Chem Res **31** (12), 2635-2642 (1992).
42. R. A. Davis and O. C. Sandall, Aiche J **39** (7), 1135-1145 (1993).
43. G. T. Rochelle, Science **325** (5948), 1652-1654 (2009).
44. J. R. Gibbins and R. I. Crane, P I Mech Eng a-J Pow **218** (A4), 231-239 (2004).
45. F. Rodriguez-Reinoso, A. C. Pastor, H. Marsh and A. Huidobro, Carbon **38** (3), 397-406 (2000).
46. J. Lehmann, J. Skjemstad, S. Sohi, J. Carter, M. Barson, P. Falloon, K. Coleman, P. Woodbury and E. Krull, Nat Geosci **1** (12), 832-835 (2008).
47. M. Ondrej, B. Peter, C. andrew and S. saran, Fuel (2011).
48. A. V. Bridgwater, Chem Eng J **91** (2-3), 87-102 (2003).
49. A. V. Bridgwater, D. Meier and D. Radlein, Org Geochem **30** (12), 1479-1493 (1999).
50. B. Esben, A. Per, E. Helge and H.-N. Henrik, Soil Biology & Biochemistry **46**, 73-79 (2012).
51. A. Zhang, Rongjun Bian, Genxing Pan, Liqiang Cui, Qaiser Hussain, Lianqing Li, Jinwei Zheng, Jufeng Zheng, Xuhui Zhang, Xiojun Han and X. Yu, Field Crops Research (127), 153-160 (2012).
52. F. Rouquerol, I. Rouquerol and K. Sing, *Adsorption of Powders and Porous Solids*. (Academic Press, London, 1999).
53. J. Lehmann and S. Joseph, *Biochar for environmental management : science and technology*. (Earthscan, London ; Sterling, VA, 2009).
54. R. Qadeer, J. Hanif, M. Saleem and M. Afzal, J Chem Soc Pakistan **16** (4), 229-235 (1994).
55. A. C. Lua, T. Yang and J. Guo, J Anal Appl Pyrol **72** (2), 279-287 (2004).
56. H. Marsh and F. Rodríguez-Reinoso, *Activated carbon*, 1st ed. (Elsevier, Amsterdam ; Boston, 2006).
57. H. Boehm, in *Adsorption by Carbons* edited by E. J. Bottani and J. M. D. Tascon (Elsevier, Oxford, 2008), pp. 301-323.
58. S. Koutcheiko, C. M. Monreal, H. Kodama, T. McCracken and L. Kotlyar, Bioresource Technology **98** (13), 2459-2464 (2007).
59. A. Bagreev, T. J. Bandosz and D. C. Locke, Carbon **39** (13), 1971-1979 (2001).
60. P. Webb and C. Orr, *Analytical Methods in Fine Particle Technology*. (Micromeritics Instrument Corporation, 1997).
61. K. S. W. Sing, in *Adsorption by Carbons*, edited by E. J. Bottani and J. M. D. Tascon (Elsevier, Oxford, 2008), pp. 1-12.
62. J. R. Richards, *Control of Gaseous Emissions - Student Manual* 3rd ed. (ICES Ltd. , 2000).
63. S. S. Brody and J. E. Chaney, J Gas Chromatogr **4** (2), 42-& (1966).
64. R. K. Stevens, A. E. Okeeffe and G. C. Ortman, Environmental Science & Technology **3** (7), 652-& (1969).
65. C. Nelder and B. Hicks, *Profit from the Peak: The End of Oil and the Greatest Investment Event of the Century*. (John Wiley & Sons, Inc., Hoboken, 2008).
66. I. KEMA and L. Summite Blue Consulting, *New York Renewable Portfolio Standard Program Evaluation Report - 2009 Review*. (NYSERDA, Albany 2009).
67. L. I. Index, (http://www.longislandindex.org/2009.324.0.html, 2009), pp. The Long Island Index is a project that gathers and publishes data on the Long Island region.
68. V. Chandra, *Fundamentals of Natural Gas: An International Perspective*. (PennWell Books, Tulsa, 2006).
69. E. Favre, R. Bounaceur and D. Roizard, J Membrane Sci **328** (1-2), 11-14 (2009).
70. E. Hubbard, (Long Island Landfill Annual Report - Brookhaven 09, Town of Brookhaven, 2009).
71. N. Y. S. D. E. Conservation, (Landfill Gas Recovery Data - 2009 Annual Report Data, 2009).

72. D. J. Tonjes, (Municipal Solid Waste Assessment Nassau and Suffolk Counties Long Island New York 2006, 2007).
73. U. S. EPA, (www.epa.gov/lmop, 2010), pp. Landfill Methane Outreach Program
74. A. A. Tsave and E. S. Karapidakis, J Optoelectron Adv M **10** (5), 1277-1281 (2008).
75. U. S. EPA, (http://www.epa.gov/outreach/sources.html, 2008), pp. Sources and emissions of methane throughout the United States.
76. W. E. Eleazer, I. Odle, William S, Y.-S. Wang and M. A. Barlaz, Environmental Science & Technology **31** (3), 911-917 (1997).
77. Y.-C. Jang and T. G. Townsend, Environmental Engineering Science **20** (3), 183-196 (2003).
78. M. A. Barlaz, Waste Management **26**, 321-333 (2006).
79. G. Y. S. Chan, L. M. Chu and M. H. Wong, Environmental Pollution **118**, 393-399 (2002).
80. U. Filipkowska, Polish Journal of Environmental Studies **17** (2), 199-207 (2008).
81. D. T. Sponza and O. N. Agdag, Process Biochemistry **39**, 2157-2165 (2003).
82. D. R. Reinhart and A. B. Al-Yousfi, Waste Management & Research **14**, 337-346 (1996).
83. N. Y. S. D. E. Conservation, (Beyond Waste: A Sustainable Materials Management Strategy for New York, 2009).
84. C. Gallert, A. Henning and J. Winter, Water Res **37** (6), 1433-1441 (2003).
85. D. Bolzonella, P. Pavan, S. Mace and F. Cecchi, Water Sci Technol **53** (8), 23-32 (2006).
86. C. Saint-Joly, S. Desbois and J. P. Lotti, Water Sci Technol **41** (3), 291-297 (2000).
87. P. Weiland, Applied Biochemistry and Biotechnology **109**, 263-274 (2003).
88. U. S. EPA, Report No. U.S. EPA # 430-R-10-006, 2011.
89. S. Martin, E. Maranon and H. Sastre, Bioresource Technology **62** (1-2), 47-54 (1997).
90. M. Haight, Water Sci Technol **52** (1-2), 553-559 (2005).
91. T. Vilsack and C. Z. F. Clark, Report No. AC-07-A-51, 2007.
92. N.Y.S.E.R.D.A, (New York State Residential Energy Prices in Nominal Dollars, 1995-2009, 2009).
93. H. Hartmann and B. K. Ahring, Water Sci Technol **53** (8), 7-22 (2006).
94. I. Alternative Resources, *Focused Verification and Validation of Advanced Solid Waste Management Conversion Technologies: Phase 2 Study*. (NYC Economic Development Corporation & NYC Department of Sanitation, New York City, 2006).
95. D. Cyranoski, Nature **444**, 262-263 (2006).
96. C. E. Nichols, in *Biocycle* (2004), Vol. 45, pp. 47-53.
97. W. Wu, Q. G. He and C. Z. Jiang, Nanoscale Res Lett **3** (11), 397-415 (2008).
98. A. K. Gupta and M. Gupta, Biomaterials **26** (18), 3995-4021 (2005).
99. J. Rockenberger, E. C. Scher and A. P. Alivisatos, J Am Chem Soc **121** (49), 11595-11596 (1999).
100. S. H. Sun and H. Zeng, J Am Chem Soc **124** (28), 8204-8205 (2002).
101. T. Hyeon, S. S. Lee, J. Park, Y. Chung and H. Bin Na, J Am Chem Soc **123** (51), 12798-12801 (2001).
102. T. Ahn, J. H. Kim, H. M. Yang, J. W. Lee and J. D. Kim, J Phys Chem C **116** (10), 6069-6076 (2012).
103. Y. S. Kang, S. Risbud, J. F. Rabolt and P. Stroeve, Chem Mater **8** (9), 2209-& (1996).
104. S. Santra, R. Tapec, N. Theodoropoulou, J. Dobson, A. Hebard and W. H. Tan, Langmuir **17** (10), 2900-2906 (2001).
105. S. Takami, T. Sato, T. Mousavand, S. Ohara, M. Umetsu and T. Adschiri, Mater Lett **61** (26), 4769-4772 (2007).
106. K. S. Suslick, S. B. Choe, A. A. Cichowlas and M. W. Grinstaff, Nature **353** (6343), 414-416 (1991).
107. K. S. Suslick, D. A. Hammerton and R. E. Cline, J Am Chem Soc **108** (18), 5641-5642 (1986).
108. S. Laurent, J. L. Bridot, L. V. Elst and R. N. Muller, Future Med Chem **2** (3), 427-449 (2010).
109. R. V. Kumar, Y. Diamant and A. Gedanken, Chem Mater **12** (8), 2301-2305 (2000).

110. K. Okitsu, M. Ashokkumar and F. Grieser, J Phys Chem B **109** (44), 20673-20675 (2005).
111. N. A. Dhas, A. Zaban and A. Gedanken, Chem Mater **11** (3), 806-813 (1999).
112. R. Vijayakumar, Y. Koltypin, I. Felner and A. Gedanken, Mat Sci Eng a-Struct **286** (1), 101-105 (2000).
113. K. S. Suslick, T. W. Hyeon and M. M. Fang, Chem Mater **8** (8), 2172-2179 (1996).
114. Y. Koltypin, X. Cao, R. Prozorov, J. Balogh, D. Kaptas and A. Gedanken, J Mater Chem **7** (12), 2453-2456 (1997).
115. K. V. P. M. Shafi, A. Ulman, X. Z. Yan, N. L. Yang, C. Estournes, H. White and M. Rafailovich, Langmuir **17** (16), 5093-5097 (2001).
116. D. Mahajan, E. T. Papish and K. Pandya, Ultrason Sonochem **11** (6), 385-392 (2004).
117. M. Gotic and S. Music, Journal of Molecular Structure **834-836**, 445-453 (2006).
118. L. Verdonck, S. Hoste, F. F. Roelandt and G. P. Vanderkelen, Journal of Molecular Structure **79** (1-4), 273-279 (1982).
119. P. Cambier, Clay Miner **21** (2), 201-210 (1986).
120. H. Namduri and S. Nasrazadani, Corros Sci **50** (9), 2493-2497 (2008).
121. F. Rodriguezreinoso and M. Molinasabio, Carbon **30** (7), 1111-1118 (1992).
122. J. A. Macia-Agullo, B. C. Moore, D. Cazorla-Amoros and A. Linares-Solano, Carbon **42** (7), 1367-1370 (2004).
123. K. Okada, N. Yamamoto, Y. Kameshima and A. Yasumori, J Colloid Interf Sci **262** (1), 179-193 (2003).
124. C. Moreno-Castilla, F. Carrasco-Marin, M. V. Lopez-Ramon and M. A. Alvarez-Merino, Carbon **39** (9), 1415-1420 (2001).
125. M. A. Lillo-Rodenas, D. Cazorla-Amoros and A. Linares-Solano, Carbon **41** (2), 267-275 (2003).
126. A. Ahmadpour and D. D. Do, Carbon **34** (4), 471-479 (1996).
127. F. Caturla, M. Molinasabio and F. Rodriguezreinoso, Carbon **29** (7), 999-1007 (1991).
128. A. Ros, M. A. Lillo-Rodenas, E. Fuente, M. A. Montes-Moran, M. J. Martin and A. Linares-Solano, Chemosphere **65** (1), 132-140 (2006).
129. Z. H. Hu and M. P. Srinivasan, Micropor Mesopor Mat **43** (3), 267-275 (2001).
130. P. Ariyadejwanich, W. Tanthapanichakoon, K. Nakagawa, S. R. Mukai and H. Tamon, Carbon **41** (1), 157-164 (2003).
131. M. MolinaSabio, M. T. Gonzalez, F. RodriguezReinoso and A. SepulvedaEscribano, Carbon **34** (4), 505-509 (1996).
132. C. F. Chang, C. Y. Chang and W. T. Tsai, J Colloid Interf Sci **232** (1), 45-49 (2000).
133. R. Azargohar and A. K. Dalai, Micropor Mesopor Mat **110** (2-3), 413-421 (2008).
134. M. Asadullah, M. A. Rahman, M. A. Motin and M. B. Sultan, Adsorpt Sci Technol **24** (9), 761-770 (2006).
135. M. Valix, W. H. Cheung and G. McKay, Chemosphere **56** (5), 493-501 (2004).
136. S. H. Guo, J. H. Peng, W. Li, K. B. Yang, L. B. Zhang, S. M. Zhang and H. Y. Xia, Appl Surf Sci **255** (20), 8443-8449 (2009).
137. A. Bagreev, S. Bashkova, D. C. Locke and T. J. Bandosz, Environ Sci Technol **35** (7), 1537-1543 (2001).
138. Y. H. Xiao, S. D. Wang, D. Y. Wu and Q. Yuan, Sep Purif Technol **59** (3), 326-332 (2008).
139. A. M. Yang, E. L. Tollefson and A. K. Dalai, Can J Chem Eng **76** (1), 76-86 (1998).
140. V. Meeyoo, D. L. Trimm and N. W. Cant, J Chem Technol Biot **68** (4), 411-416 (1997).
141. A. Bagreev, S. Katikaneni, S. Parab and T. J. Bandosz, Catal Today **99** (3-4), 329-337 (2005).
142. T. J. Bandosz, in *Adsorption by Carbons*, edited by E. J. Bottani and J. M. D. Tascon (Elsevier, Oxford, 2008), pp. 533-556.
143. A. Bagreev and T. J. Bandosz, Carbon **39** (15), 2303-2311 (2001).
144. F. Adib, A. Bagreev and T. J. Bandosz, Environ Sci Technol **34** (4), 686-692 (2000).
145. T. J. Bandosz, Carbon **37** (3), 483-491 (1999).
146. O. C. Cariaso and P. L. Walker, Carbon **13** (3), 233-239 (1975).

147. S. Bashkova, F. S. Baker, X. X. Wu, T. R. Armstrong and V. Schwartz, Carbon **45** (6), 1354-1363 (2007).
148. M. Steijns, F. Derks, A. Verloop and P. Mars, J Catal **42** (1), 87-95 (1976).
149. T. K. Ghosh and E. L. Tollefson, Can J Chem Eng **64** (6), 969-976 (1986).
150. T. K. Ghosh and E. L. Tollefson, Can J Chem Eng **64** (6), 960-968 (1986).
151. M. Steijns and P. Mars, Ind Eng Chem Prod Rd **16** (1), 35-41 (1977).
152. A. Bagreev, F. Adib and T. J. Bandosz, Carbon **39** (12), 1897-1905 (2001).
153. L. M. Le Leuch, A. Subrenat and P. Le Cloirec, Langmuir **19** (26), 10869-10877 (2003).
154. J. A. Lagas, J. Borsboom and P. H. Berben, Oil Gas J **86** (41), 68-71 (1988).
155. P. F. M. T. Vannisselrooy and J. A. Lagas, Catal Today **16** (2), 263-271 (1993).
156. J. S. Chung, S. C. Paik, H. S. Kim, D. S. Lee and I. S. Nam, Catal Today **35** (1-2), 37-43 (1997).
157. M. Y. Shin, D. W. Park and J. S. Chung, Appl Catal B-Environ **30** (3-4), 409-419 (2001).
158. N. Keller, C. Pham-Huu and M. J. Ledoux, Appl Catal a-Gen **217** (1-2), 205-217 (2001).
159. N. Keller, C. Pham-Huu, C. Crouzet, M. J. Ledoux, S. Savin-Poncet, J. B. Nougayrede and J. Bousquet, Catal Today **53** (4), 535-542 (1999).
160. K. D. Jung, O. S. Joo, S. H. Cho and S. H. Han, Appl Catal a-Gen **240** (1-2), 235-241 (2003).
161. K. T. Li, C. S. Yen and N. S. Shyu, Appl Catal a-Gen **156** (1), 117-130 (1997).
162. J. P. Anerousis and S. K. Whitman, Oil Gas J **83** (7), 71-76 (1985).
163. A. Samuels, Oil Gas J **88** (6), 44-46 (1990).
164. Y. Kotera, N. Todo and K. Fukuda, USA (1976).
165. K. Fukuda, M. Dokiya, T. Kameyama and Y. Kotera, Ind Eng Chem Fund **17** (4), 243-248 (1978).
166. L. M. Alshamma and S. A. Naman, Int J Hydrogen Energ **14** (3), 173-179 (1989).
167. T. V. Reshetenko, S. R. Khairulin, Z. R. Ismagilov and V. V. Kuznetsov, Int J Hydrogen Energ **27** (4), 387-394 (2002).
168. Bachinsk.Dj, Econ Geol **64** (1), 56-& (1969).
169. T. J. Bandosz, J Colloid Interf Sci **246** (1), 1-20 (2002).
170. A. F. Zhang, L. Q. Cui, G. X. Pan, L. Q. Li, Q. Hussain, X. H. Zhang, J. W. Zheng and D. Crowley, Agriculture Ecosystems & Environment **139** (4), 469-475 (2010).
171. F. Adib, A. Bagreev and T. J. Bandosz, J Colloid Interf Sci **214** (2), 407-415 (1999).
172. M. Frenklach, J. H. Lee, J. N. White and W. C. Gardiner, Combust Flame **41** (1), 1-16 (1981).
173. W. S. Yao and F. J. Millero, Mar Chem **52** (1), 1-16 (1996).
174. V. Rouchon, H. Badet, O. Belhadj, O. Bonnerot, B. Lavedrine, J. G. Michard and S. Miska, J Raman Spectrosc **43** (9), 1265-1274 (2012).
175. Y. S. Lee, H. T. Kim and K. O. Yoo, Ind Eng Chem Res **34** (4), 1181-1188 (1995).
176. M. Yumura and E. Furimsky, Ind Eng Chem Proc Dd **24** (4), 1165-1168 (1985).
177. Y. Nagase, T. Jin, H. Hattori, T. Yamaguchi and K. Tanabe, B Chem Soc Jpn **58** (3), 916-918 (1985).
178. P. R. Westmoreland, J. B. Gibson and D. P. Harrison, Environ Sci Technol **11** (5), 488-491 (1977).
179. J. D. White, F. R. Groves and D. P. Harrison, Catal Today **40** (1), 47-57 (1998).
180. M. C. Sukop and D. T. Thorne, *Lattice Boltzmann modeling : an introduction for geoscientists and engineers*. (Springer, Berlin ; New York, 2006).